Université libre de Bruxelles
Faculté des Sciences
Laboratoire de Glaciologie

Thèse de Doctorat

Impact of improved basal and surface boundary conditions on the mass balance of the Sør Rondane Mountains glacial system, Dronning Maud Land, Antarctica.

Impact des conditions aux limites (basales et de surface) sur le bilan de masse du système glaciaire des Sør Rondane Mountains en Antarctique.

Auteur :
Denis Callens

Sous la direction du
Prof. Frank Pattyn

Thèse présentée en vue de l'obtention du titre de Docteur en Science

Le 6 novembre 2014

Abstract

Mass changes of polar ice sheets have an important societal impact, because they affect global sea level. Estimating the current mass budget of ice sheets is equivalent to determining the balance between the surface mass gain through precipitation and the outflow across the grounding line. In Antarctica, the latter is mainly governed by oceanic processes and outlet glacier dynamics.

In this thesis, we assess the mass balance of a part of eastern Dronning Maud Land via an input/output method. Input is given by recent surface accumulation estimations of the whole drainage basin. The outflow at the grounding line is determined from the radar data of a recent airborne survey and satellite-based velocities using a flow model of combined plug flow and simple shear. We estimate the regional mass balance in this area to be between 1.88±8.50 and 3.78±3.32 Gt a^{-1} depending on the surface mass balance (SMB) dataset used. This study also reveals that the plug flow assumption is acceptable at the grounding line of ice streams.

The mass balance of drainage basins is governed by the dynamics of their outlet glaciers and more specifically the flow conditions at the grounding line. Thanks to an airborne radar survey we define the bed properties close to the grounding line of the West Ragnhild Glacier (WRG) in the Sør Rondane Mountains. Geometry and reflectivity analyses reveal that the bed of the last 65 km upstream of the grounding line is sediment covered and saturated with water. This setting promotes the dominance of basal motion leading to a change in the flow regime: in the interior flow is governed by internal deformation while its relative importance decreases to become driven by basal sliding.

Subsequently we present the results of the reconstruction of the SMB across an ice rise through radar data and inverse modelling. The analysis demonstrates that atmospheric circulation was stable during the last millennium. Ice rises induce an orographic uplift of the atmospheric flow and therefore influence the pattern of the SMB across them, resulting in an asymmetric SMB distribution. Since the geometry of the internal reflection horizons observed in radar data depends on the SMB pattern, the asymmetry observed in radar layers reveals the trajectories of air masses at the time of deposit. We present an original and robust method to quantify this SMB distribution. Combining shallow and deep radar layers, SMB across Derwael Ice Rise is reconstructed. Two methods are employed as a function of the depth of the layers: i.e., the shallow layer approximation for the surface radar layers and an optimization technique based on an ice flow model for the deeper ones. Both methods produce similar results. We identify a difference in SMB magnitude of 2.5 between the flanks and the ice rise divide, as well as a shift of ≈4 km between the SMB maximum and the crest. Across the ice rise, SMB exhibits a very large variability, ranging from 0.3 to 0.9 m w.e. a^{-1}. This anomaly is robust in time.

Finally we draw a comprehensive description of the Sør Rondane Mountains sector. The glacial system is close to the equilibrium and seems stable but evidences suggest that it is a fragile equilibrium. The proximity of the open ocean certainly favours the interaction between warm water and the ice shelf cavity conducting to potential important melting. The thinning associated with this melting can detach the ice shelf from pinning points. This will reduce the buttressing from the ice shelf, outlet glaciers will accelerate and mass transfer toward the ocean will increase. Therefore, the future of Antarctic Ice Sheet directly depends on the changes affecting its boundaries and assessing the sensitivity of the ice sheets is essential to quantify and anticipate the future variation of mass balance.

Résumé

Du fait de son impact sur le niveau marin, la variation de masse des calottes polaires est un enjeu sociétal majeur. Pour estimer le bilan de masse actuel des calottes, il faut faire le bilan entre les gains et pertes de masse. Les premiers dépendent essentiellement des précipitations alors que les secondes sont régies par les flux de glace à la ligne d'ancrage. Ce flux est en grande partie déterminé par l'interaction entre la calotte et l'océan, ainsi que par la dynamique des glaciers émissaires.

Dans cette thèse, nous évaluons les gains de masse grâce à 3 estimations récentes du taux d'accumulation neigeuse pour chaque bassin de drainage autours des montagnes Sør Rondane. Le débit à la ligne d'ancrage, lui, est défini grâce à des mesures radar, pour la géométrie, et des vitesses obtenues via des mesures satellitaires. Notre estimation du bilan de masse régional se situe entre 1.88 ± 8.50 et 3.78 ± 3.32 Gt a^{-1}. Ce travail a aussi montré que l'hypothèse d'écoulement piston est acceptable dans les environs de la ligne d'ancrage des glaciers émissaires.

Le bilan de masse des bassins de drainage en Antarctique est régi par la dynamique des glaciers émissaires et plus particulièrement par les conditions d'écoulement à la ligne d'ancrage. Grâce à une série de mesures radar aéroportées, les propriétés du lit sous le glacier Ragnhild occidental ont été investiguées. La géométrie et la réflectivité suggèrent que le lit, proche de la ligne d'ancrage, est couvert de sédiments et saturé en eau. Cette configuration favorise un glissement basal important. Par conséquent, la dynamique de la glace, régie par la déformation interne en amont, change de régime pour devenir essentiellement dominée par le glissement basal.

Ensuite, nous présentons les résultats d'une reconstruction du bilan de masse de surface réalisée grâce à des données radar et une modélisation inverse. Nous apportons des preuves que la circulation atmosphérique de la région est restée stable au cours du dernier millénaire. En effet, les ice rises induisent une ascension orographique des masses d'air et donc influencent la répartition du bilan de masse de ceux-ci. Comme la géométrie des horizons de réflexion dépend en grande partie de ce bilan, l'asymétrie observée le long de ces horizons renseigne sur la trajectoire des masses d'air à l'époque du dépôt. En combinant horizons de surface et profonds, nous avons reconstruit le bilan de masse de surface du Derwael Ice Rise. Deux méthodes sont utilisées en fonction de la profondeur de l'horizon. Pour les horizons de surface, nous utilisons l' "approximation de l'horizon de surface" alors que pour les profonds, nous utilisons une méthode d'optimisation basée sur la modélisation de l'écoulement. Les deux méthodes renvoient des résultats similaires. Le bilan de masse de surface varie d'un facteur de 2.5 entre les flancs et le centre de l'ice rise. Les valeurs d'accumulation s'étendant de 0.3 à 0.9 m w.e. a^{-1}.

Nous terminons avec une description globale du secteur des Sør Rondane Mountains. Le système est proche de l'équilibre et semble stable mais plusieurs indices suggèrent que cet état pourrait rapidement changer suite à un forage externe. Sa proximité avec l'océan favorise les interactions entre la cavité sous l'ice shelf et les eaux chaudes de l'océan. La fusion et l'amincissement de l'ice shelf sont des conséquences de cette interaction entrainant une diminution du nombre de points de contact entre l'ice shelf et le socle rocheux. De ce fait, l'ice shelf ne joue plus son rôle régulateur et la calotte perd de la masse. Connaitre les conditions aux limites de la calotte est donc essentiel pour anticiper les changements de demain affectant la calotte antarctique.

Contents

List of Figures

List of Tables

Abbreviations

ACC	**A**ntarctic **C**ircumpolar **C**urrent
AIS	**A**ntarctic **I**ce **S**heet
APIS	**A**ntarctic **P**eninsula **I**ce **S**heet
AWI	**A**lfred **W**egener **I**nstitute
BM	**B**elgica **M**ountains
BRP	**B**ed **R**eflection **P**ower
CDW	**C**ircumpolar **D**eep **W**ater
CTD	**C**onductivity **T**emperature **D**epth
DIR	**D**erwael **I**ce **R**ise
DML	**D**ronning **M**aud **L**and
EAIS	**E**ast **A**ntarctic **I**ce **S**heet
ERG	**E**ast **R**agnhild **G**lacier
FFT	**F**ast **F**ourier **T**ransform
FKIR	**F**ran**K**enny **I**ce **R**ise
GIA	**G**lacial **I**sostatic **A**adjustment
GICs	**G**laciers and **I**ce **C**ap**s**
GIS	**G**reenland **I**ce **S**heet
GRACE	**G**ravity and **R**ecovery **A**nd **C**limate **E**xperiment
HB	H.E. **H**ansen**B**reen
IMBIE	**I**ce-sheet **M**ass **B**alance **I**nter-comparison **E**xercise
IOM	**I**nput/**O**utput **M**ethod
IPCC	**I**ntergovernmental and **P**anel **C**limate **C**hange
IRH	**I**nternal **R**eflection **H**orizon
mCDW	**m**odified **C**ircumpolar **D**eep **W**ater
pmp	**p**ressure **m**elting **p**oint
psu	**p**ractical **s**alinity **u**nit
RACMO	**R**egional **A**tmospheric **C**limate **MO**del
RBIS	**R**oi **B**audouin **I**ce **S**helf
RES	**R**adio **E**cho **S**ounding
RI	**R**oughness **I**ndex
SIA	**S**hallow **I**ce **A**pproximation
SLE	**S**ea **L**evel **E**quivalent
SMB	**S**urface **M**ass **B**alance
SRM	**S**ør **R**ondane **M**ountains
TB	**T**usse**Breen**
WAIS	**W**est **A**ntarctic **I**ce **S**heet
WRG	**W**est **R**agnhild **G**lacier

List of Publications

Published in peer reviewed journals

Callens, D., Matsuoka, K., Steinhage, D., Smith, B., Witrant, E., and Pattyn, F. (2014). Transition of flow regime along a marine-terminating outlet glacier in east antarctica. *The Cryosphere*, 8:867–875.

Callens, D., Thonnard, N., Lenaerts, J. T.M., van Wessem, J. M., van de Berg, W.J., Matsuoka, K., Pattyn, F. (2014). Mass balance of the Sør Rondane Glacial System. *accepted to Annals of Glaciology.*

Fretwell, P., Pritchard, H. D., Vaughan, D. G., Bamber, J. L., Barrand, N. E., Bell, R., Bianchi, C., Bingham, R. G., Blankenship, D. D., Casassa, G., Catania, G., **Callens, D.**, Conway, H., Cook, A. J., Corr, H. F. J., Damaske, D., Damm, V., Ferraccioli, F., Forsberg, R., Fujita, S., Gim, Y., Gogineni, P., Griggs, J. A., Hindmarsh, R. C. A., Holmlund, P., Holt, J. W., Jacobel, R. W., Jenkins, A., Jokat, W., Jordan, T., King, E. C., Kohler, J., Krabill, W., Riger-Kusk, M., Langley, K. A., Leitchenkov, G., Leuschen, C., Luyendyk, B. P., Matsuoka, K., Mouginot, J., Nitsche, F. O., Nogi, Y., Nost, O. A., Popov, S. V., Rignot, E., Rippin, D. M., Rivera, A., Roberts, J., Ross, N., Siegert, M. J., Smith, A. M., Steinhage, D., Studinger, M., Sun, B., Tinto, B. K., Welch, B. C., Wilson, D., Young, D. A., Xiangbin, C., and Zirizzotti, A. (2013). Bedmap2: improved ice bed, surface and thickness datasets for antarctica. *The Cryosphere*, 7:375–393.

Lenaerts, J. T. M., Brown, J., van den Broeke, M. R., Matsuoka, K., Drews, R., **Callens, D.**, Philippe, M., Gorodetskaya, I. V., van Meijgaard, E., Reijmer, C. H., Pattyn, F., and Van Lipzig, N. P. M. (2014). High variability of climate and surface mass balance induced by antarctic ice rises. *J. Glaciol.*, 60(224):1101–1110.

Matsuoka, K., Pattyn, F., **Callens, D.**, Conway, H. (2014). Radar characterization of the basal interface across the grounding zone of an ice-rise promontory in East Antarctica. *Annals of Glaciology*, 53(60):29–34.

Matsuoka, K., **Callens, D.**, Steinhage, D., Pattyn, F. (2014). Surface elevation and ice thickness measurements of an airborne radar survey made in the Sør Rondane Mountains, Antarctica. *Pangaea*, Digital media.

Pattyn, F., Matsuoka, K., Conway, H., **Callens, D.**, Depoorter, M., Docquier, D., Hubbard, B., Samyn, D., and Tison, J. L. (2012). Radar and ice-core evidence for active ice-ocean interaction under the Roi Baudouin ice shelf, East Antarctica. *J. Geophys. Res.*, 117(F04008).

Submitted in peer reviewed journals

Drews, R., Matusoka, K., Martìn, C., **Callens, D.**, Bergeot, N., and Pattyn, F. (2014). Sustained thinning over millennia of an ice rise in dronning maud land, antarctica. *Submitted to J. Geophys. Res.*

In preparation

Callens, D., Witrant, E., Drews, R., Philippe, M. and Pattyn, F. (2014). Surface mass balance anomaly across an ice rise derived from internal reflection horizons through inverse modelling.

Leonard, K., Pattyn, F., **Callens, D.**, Matusoka, K., Derwael, JJ., Tison, JL. (2014). Warm deep water under an East Antarctic Ice Shelf: implications for grounding line melt.

I undertook the majority of the analyses and interpretations of the articles to which I am the leading author. Other authors contributed with data (Steinhage, Smith, Lenaerts, van Wessem, ven den Berg and Philippe) or methodology (Matsuoka, Witrant, Thonnard, Drews). I brought data of ice thickness along the Ragnhild Coast to Fretwell et al. (2013). In Lenaerts et al. (2014), I took part in the radar section of the paper to estimate the surface mass balance across the Derwael Ice Rise. In Matsuoka et al. (2012b), Pattyn et al. (2012) and Drews et al. (2014), I did the processing and took part in the interpretation of the radar data. Finally, I was in charge of the figure and took part in the discussion of Leonard et al. (Prep).

Chapter 1

Introduction

1.1 Climate change

"Warming of the climate system is unequivocal, and since the 1950s, many of the observed changes are unprecedented over decades to millennia. The atmosphere and ocean have warmed, the amounts of snow and ice have diminished, sea level has risen, and the concentrations of greenhouse gases have increased"

IPCC WGI AR5, 2013: Summary for Policymakers

Due to massive release of greenhouse gases since the industrial revolution, humanity irrevocably changes its environment. Atmospheric warming triggers a variety of changes in all the climate system. As every component of the environment are interconnected, changes in wind speed and direction, ocean circulation, snow cover or iceberg calving are expected. Some of them are obvious while others are less straightforward. Nevertheless each of them are important since feedback can enhance or buffer the ongoing climate change.

Climate change will affect every aspect of human activities and especially the most vulnerable. Among these changes, the sea level rise threatens a lot of people. Even if low elevation coastal zone[1] represents only 2% of the world's land area, 10% of the population live there, i.e. 600 million people in 2000 (Wong et al., 2014). These regions are not only affected by the mean sea level rise but will also have to face stronger and more frequent extreme sea level when astronomical tides and storm surges combine to produce extreme sea level anomaly.

This thesis aims to analyse one important aspect of these multiple changes observed all over the world : the potential Antarctic contribution to the sea level rise. The sea level rise is probably the biggest hazard for humanity and Antarctic ice sheet has a great potential to enhance it.

[1]Coastal regions up to 10 m of elevation.

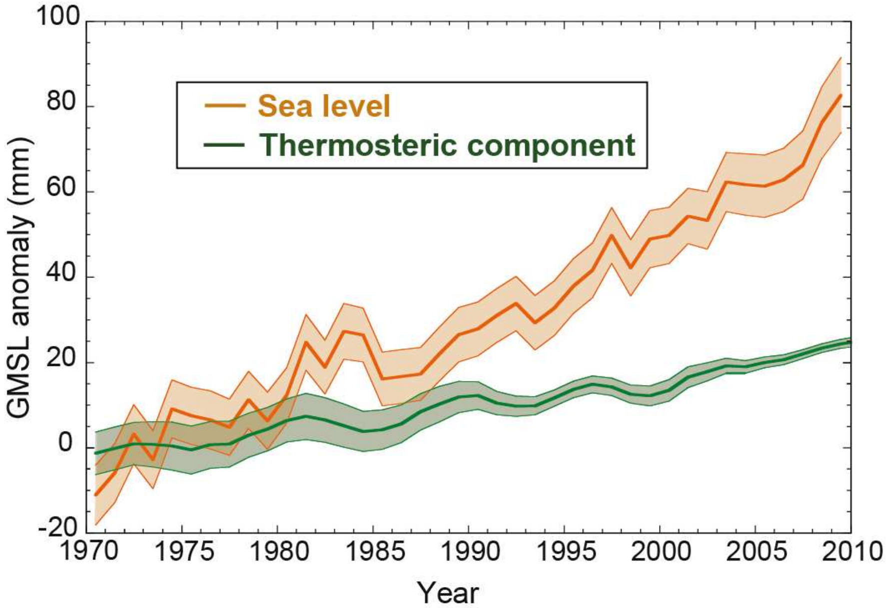

FIGURE 1.1: Global mean sea level anomaly (1970-2010) from tide gauges along with the thermosteric component up to 700 m estimated from in situ temperature profiles. This is a reproduction from IPCC report AR5 (Rhein et al., 2013)

1.2 Sea level Rise

1.2.1 Overview

"The rate of sea level rise since the mid-19th century has been larger than the mean rate during the previous two millennia. Over the period 1901 to 2010, global mean sea level rose by 0.19 [0.17 to 0.21] m"

IPCC WGI AR5, 2013: Summary for Policymakers

Forced by the warming of the climate, sea level rose through the XXth century at a mean rate of 1.7 $\pm$ 0.2 mm a^{-1} (Rhein et al., 2013). This is obtained by spatially extrapolating sparse tide gauges with today's observed distribution (Church and White, 2011). Since 1993, continuous satellite records are available and measure a rising rate of 3.4 $\pm$ 0.4 mm a^{-1} (Nerem et al., 2010). This sea level trend is driven by two processes : the temperature via mass expansion (thermosteric component) and the mass flux from other reservoirs to the ocean (mass component). The former is equal to 1.1 $\pm$ 0.3 mm a^{-1} for the whole water column. As it is more affected by the atmospheric warming, the expansion of the top 700 m will represent the major part of this component ($\approx$ 0.8 mm a^{-1}for the same period). However its relative importance shrinks. Indeed, the thermosteric component continues to grow but slower than the mass components (Figure 1.1).

Recently GRACE satellites provide the first measurements of the mass component. They measure the gravity field from which infinitesimal change of mass can be observed. Unfortunately, GRACE estimates suffer from two pitfalls : (i) uncertainty in glacial isostatic adjustment (GIA) (leading to great uncertainty in the magnitude), (ii) GRACE data collection is very limited in time[2] and the present-day trends cannot be extrapolated in the future to make projections. There is another way to quantify the mass increasing of the ocean : estimating the mass loss of the other water reservoirs. With this method, we extend the time range of the estimates and enable projections.

[2]The satellites start collecting data in 2002

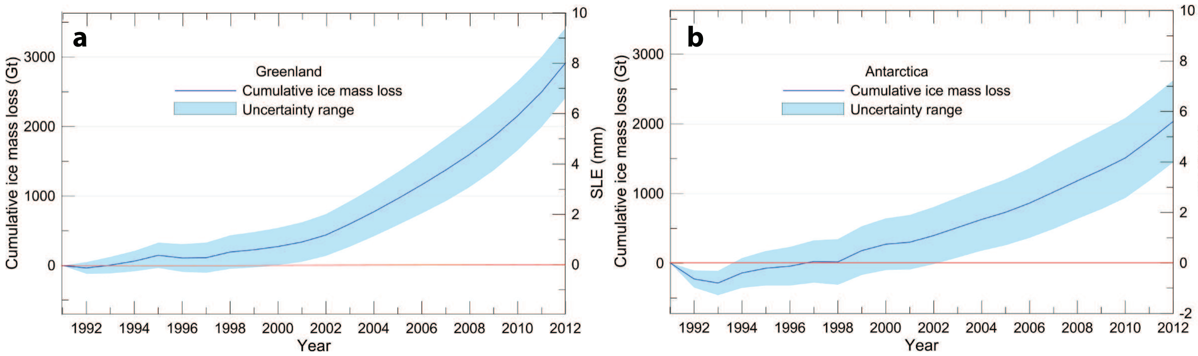

FIGURE 1.2: Cumulative ice mass loss (and sea level equivalent, SLE) from (a) Greenland derived as annual averages from 18 recent studies and from (b) Antarctica derived as annual averages from 10 recent studies. The uncertainty range corresponds to maximum and minimum values for each years. This is a reproduction from IPCC report AR5 (Vaughan et al., 2013)

Among the flux affecting the mass component, cryospheric contribution is by far the most important. Water comes from the shrinking of glaciers and the Greenland and Antarctic Ice Sheets. Glaciers and ice caps (GICs) experienced the most spectacular mass loss, especially in terms of area covered. As it is possible for the mass component of the ocean, GRACE measurements are also affected by the mass change in the cryosphere. GICs contribution to sea level rise from GRACE measurement is -259 $\pm$ 28 Gt a^{-1}, i.e. 0.7 $\pm$ 0.08 mm a^{-1}, between 2003 and 2009 (Gardner et al., 2013). The joint contribution from Greenland (GIS) and Antarctic Ice Sheets (AIS) is of the same order of magnitude as the glacier contribution. Vaughan et al. (2013) average the results from 18 (GIS) and 10 (AIS) mass change studies (Figure 1.2). Following this method, GIS and AIS are losing 121 $\pm$ 27 Gt a^{-1} (i.e. 0.33 $\pm$ 0.07 mm a^{-1}) and 97 $\pm$ 37 Gt a^{-1} (i.e. 0.27 $\pm$ 0.10 mm a^{-1}), respectively, during the last two decades (1993–2010). Vaughan et al. (2013) also observe a recent acceleration of mass loss from these ice bodies between 2005 and 2010 with a low to mid confidence level. This statement is questioned by Shepherd et al. (2012) as they observed that mass balance is affected by an inter-annual cycle of 2 to 4 years. Thus longer time series are a prerequisite for any assessment of acceleration because the observed increase may not be a long term trend.

One can consider that a basic average of the studies can conceal the disparity in quality of these studies. The IMBIE consortium (Shepherd et al., 2012) attempted to reconcile the different mass balance estimate. They standardized the time span and the study coverage as well as the methodology. They came out with a reconciled estimate of the mean mass change between 1992 and 2011: -142 $\pm$ 49 Gt a^{-1} and -71 $\pm$ 53 Gt a^{-1} for GIS and AIS[3], respectively. The total contribution of the two ice sheets is -213 Gt a^{-1} (i.e. 0.58 mm a^{-1}).

1.2.2 Antarctic mass balance

The mass budget of an ice sheet is the balance between the mass input and output. Input is the solid precipitation (snow) which compacts to form ice. Due to gravity, the ice mass will slowly move toward the coast. The outfluxes determined by both melt water runoff and mass export through the ocean. Whereas in Greenland, these processes are equally shared (van den Broeke et al., 2009), in Antarctica, near-absence of surface runoff is observed. Therefore the surface mass balance (SMB) is virtually everywhere positive and all the mass output is governed through the floating part of the ice sheet : the ice shelves where it calves or melts into the ocean.

[3] Do not forget the list of abbreviations on page xiv

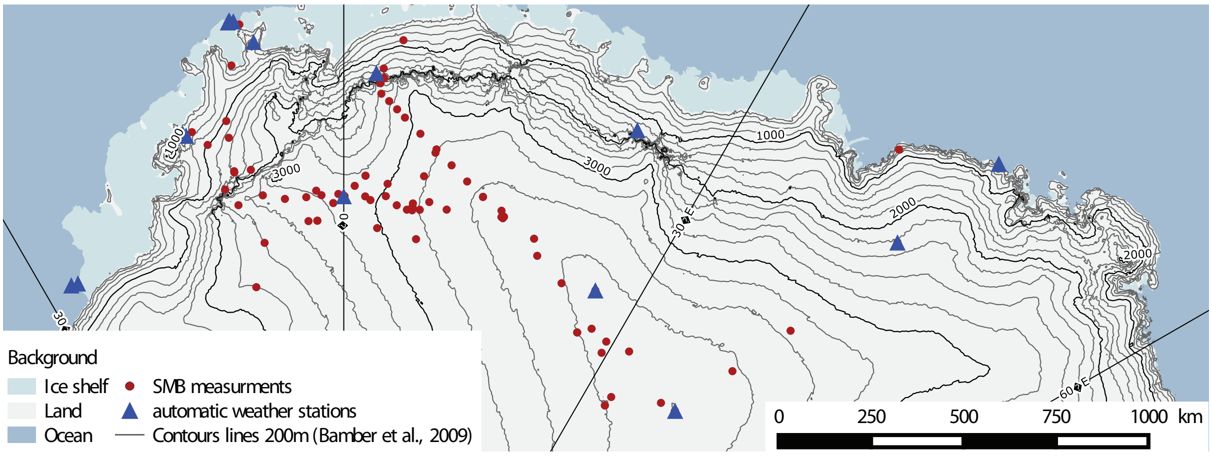

FIGURE 1.3: Compilation of the firn core made in Dronning Maud Land during the last two decades (red circle). Blue triangles represent the automatic weather stations working in 2014. Large part of the east is still not sampled. This figure is adapted from Fjøsne (2014).

1.2.2.1 Surface Mass Balance

Until now, measurements of SMB are very sparse, often discontinuous and sometimes inaccurate. For instance, stake measurements are hampered by inter-annual variability. The stakes can be bend by the wind and buried by the snow. Therefore it is extremely uncommon to have long time series in the same place. Automatic weather stations are even scarcer. However, they are of interest because they can relate the atmospheric properties to the SMB : temperature, wind and precipitation. It helps to understand the impact of these properties on the SMB. Unfortunately, they are subject to power cuts. Furthermore, time series are also barely long enough to establish the climatic SMB and the potential trend in it. The only reliable way to retrieve this SMB and its trends are ice core studies. However, these are labour intensive. Therefore it is almost impossible to have a sufficiently fine distribution to assess the regional SMB (Figure 1.3). Furthermore observed SMB trends in ice cores may be very local. Indeed, spatial variability of the SMB at kilometre scale is one order of magnitude higher than its temporal variability at the centennial scale (Frezzotti et al., 2013). For instance, SMB trend in DML varies a lot depending on the ice core studies : most of the studies showed no trends on the plateau (Anschütz et al., 2009, Isaksson et al., 1999) others identified a positive trends in the SMB within the last fifty years of the XXth century (Fujita et al., 2011). Surprisingly SMB reconstruction from ice core are even scarcer close to the coast (Figure 1.3). Combination with radio-echo sounding can extrapolate these ice core data but they remains spatially limited.

SMB distribution is normally determined using two methods. Firstly, spatial extrapolation of ground point measurement with satellite measurement (e.g. Arthern et al., 2006). The sparse measurements are used to calibrate the satellite distribution. Secondly, atmospheric modelling allows to determine the SMB distribution based on the constitutive processes which govern the atmosphere. Reanalysis can be performed in van de Berg et al. (2006) or not in Lenaerts et al. (2012) and Van Wessem et al. (2014). Reanalysis allows to correct the results of the model following regional mean of ground measurement. When no reanalysis is performed, measurement are used to validate the results. The atmospheric modelling has the advantage to introduce the understanding of the processes in the reasoning. Unfortunately, modelling relies on approximation and has to be parametrized and validated and data which are qualified for this are very rare. Only 745 reliable in-situ SMB measurements were used to validate Lenaerts et al. (2012) results in Antarctica. Furthermore they are not evenly distributed, a large part of the East Antarctic Plateau is not sampled (Figure 1.3).

Lenaerts et al. (2012) estimated with RACMO (Regional Atmoshperic Climate MOdel) an ice-sheet integrated SMB of 2418 $\pm$ 181 Gt a^{-1}. It is also important to note that most of the accumulation is located close to the coast. For instance, 18% of the total SMB accumulates over the ice shelves which represents only 11% of the total area (Lenaerts et al., 2012). It is likely that the SMB of the interior is stable because of the remoteness to water sources and the extremely cold temperature observed there. Indeed, Frezzotti et al. (2013) compiled SMB reconstruction from ice cores all around Antarctica and did not observed any trend in DML over the last 800 years. Therefore a significant trend in the global surface mass balance of Antarctica seems to be unlikely and precipitation is not the driver of the observed trends in mass balance of the ice sheet, aforementioned. As the input is not responsible for the mass balance deficit trend observed, the output sinks can be questioned.

1.2.2.2 Ice shelves as the tap of the Antarctic Ice Sheet

At least 74% of the total ice discharged from the Antarctica Ice Sheet passes through ice shelves (Bindschadler et al., 2011a). Usually ice streams concentrate the ice into narrow channels which discharge into the ocean through ice shelves. Ice shelves are freely floating except in some points where friction occurs. They are generally confined into embayments in which the sides exert friction on the fast flowing part. The second type of friction comes from the bottom. As ice flows over sea floor topographic highs (pinning points), ice is locally grounded and hence friction also occurs. These loci of friction are important : they buttress and restrain the seaward-flowing outlet glaciers. Scambos et al. (2004) brilliantly demonstrated this process by GPS measurements, before and after the collapse of Larsen B Ice Shelf. Modelling studies have also shown the importance of the pinning points (e.g. Favier et al., 2012). Therefore their impact directly affects the behaviour of the whole ice sheet.

For a while, it was commonly assumed that EAIS was stable and its changes are negligible in regards of the changes observed in WAIS. Recently, Mengel and Levermann (2014) showed that the Wilkes Basin in East Antarctica is equally prone to marine ice sheet instability than WAIS. Small changes at the coastal margins of the basin will lead to significant thinning of all the basin and a sea level rise of 3–4 m. This basin is drained by the Ninnis and Cook ice streams. West of them, a larger glacier is subject of growing concern : Totten Glacier. From 2002 to 2009 it has lost mass at a growing rate (Chen et al., 2009). This may be driven by the conditions in the ice shelf cavity. Simultaneously to the thinning of the glacier, a decrease of the cold polynya water flux is observed. This cold water enters the ice shelf cavity and prevents melting. The decreasing of cold water input favours the basal melting (Khazendar et al., 2013). Until now, no change is observed in Dronning Maud Land, our region of interest, but it remains largely unknown due to the scarcity of reliable measurements.

Therefore, ice shelves are a significant control on ice sheet mass balance. Two features have a predominant influence on their stability :

Ice rise and ice rumples Most ice shelves run aground against ice rises or ice rumples. These are local highs in the ocean bed topography which divert or buttress to flow of the surrounding ice shelf (Figure 1.4). Ice rises are large features characterized by their own flow regime : ice flows radially from a divide toward the margins and the surrounding ice shelf. They can be seen as miniature ice caps (Martin and Sanderson, 1980). On the other hand, ice rumples are smaller features which merely support the ice shelf. The latter pinning points are more sensitive to changes.

Ice rises and rumples exert a back force on the motion of the ice shelves which restrains the flow of ice streams. This buttressing play a critical role in modulating the mass balance of the Antarctic

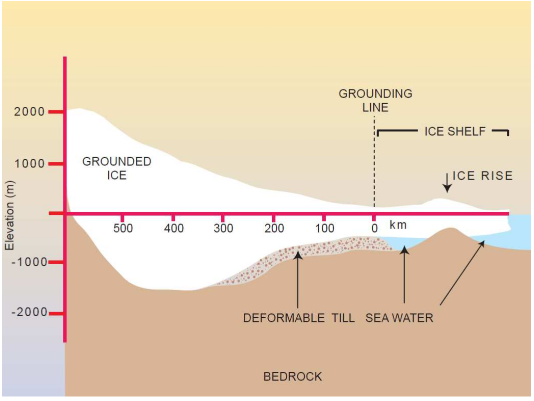

FIGURE 1.4: Schematic side view of the system ice stream - ice shelf - ice rise. Ice flows from left to right. This figure is a reproduction of Figure 2 in Oppenheimer (1998)

ice sheet. The acceleration of glaciers flowing into Larsen B ice shelf due to the collapse in 2002 (Scambos et al., 2004) led to significant thinning of them. Their observed imbalance in 2008 was equal to 4.34 ± 1.64 Gt a^{-1}. On one of these , Crane Glacier, the thinning pulse, initially greatest near the calving front, has broadened and migrated upstream (Berthier et al., 2012). The pinning points are important to stabilise the ice shelves and to avoid their collapse.

Ungrounding of a pinning point can induce severe change to the upstream ice stream. Two processes can lead to the decreasing of number of friction points : a variation of the sea surface elevation and a thinning of the ice shelf. Indeed as ice shelf is in hydrostatic equilibrium, a decrease of 10% of the ice shelf thickness will produce an uplift of the ice shelf bottom of 9% of the depth.

Ice shelf cavity The interaction between the ocean and the ice shelf occurs in the ice shelf cavity. This interaction is very active and results in massive melting and sometimes refreezing. At a continental scale, oceanic erosion represents about half of the total mass loss of the ice shelves (Depoorter et al., 2013). Therefore climate change affecting the ocean can directly affect the mass balance of the ice sheet. Currently, in the Pacific and Indian ocean, a southward shift of the Antarctic circumpolar current is observed without significant changes in its properties (Rhein et al., 2013). This current carries relatively warm water and approaches the ice shelves margins. It increases the total amount of heat available to melt the ice. In a few places (e.g. Pine Island Ice Shelf, Jenkins et al., 2010), we observed incursion of warm water into the ice cavity which enhance the melt rate while, in other place (e.g. Fimbulisen, Hattermann et al., 2012), interactions between the open ocean and the ice shelf cavity are limited to small seasonal eddy flows.

Sub ice shelf melting has a superlinear response to increase in ocean temperature (Holland et al., 2008). When ocean water reaches the ice at the grounding line, it melts the ice. Two scenarii are possible. If the water is relatively cold (-1.8 °C), it will melt the ice at the grounding line. This melt water will move up driven by its buoyancy. During its movement, the water body will entrain salt form the surrounding water and will equilibrate at some point. It will freeze there since it is supercooled for the conditions of temperature and pressure reached there. This situation is depicted by Figure 1.5a. The newly formed ice is called marine ice and has peculiar property such as a salinity one order of magnitude higher than meteoric ice (Tison and Khazendar, 2001). The second case happens when water is relatively warm. The melting starts also at the grounding line but water has enough heat content to maintain a latent heat flux all along its way up. This results in a plume of fresh water in front of the ice shelf. This is typically the case of Pine Island Glacier (Stanton et al., 2013).

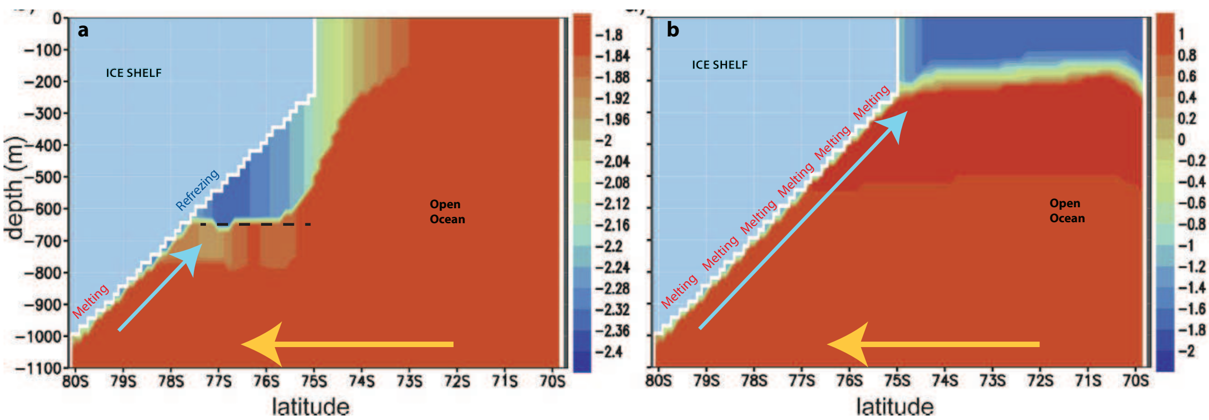

FIGURE 1.5: Circulation of water in the ice shelf cavity for two different situation : (a) influx of cold water (-1.8 °C), (b) incoming of warmer water (1 °C). Yellow arrows denote the influx of ocean water into ice shelf cavity while blue arrows are the trajectories of melted water, This figure is adapted from figure 4c and 4d in Holland et al. (2008)

If the relation between ocean temperature and basal melting is clear, there is no direct relation between them that can be applied to all the ice shelves. Indeed, a single melt rate sensitivity to warming does not exist because its dependence to the shape of the roof of the ice shelf cavity (Holland et al., 2008). As mentioned before, fresh water forms at the interface between the two media. This is called the mixed layer (Figure 1.6). Melting quickly consumes all the heat available in this layer and diffusivity from the interior of the ice shelf cavity cannot sustain this melting. However, the surrounding water is denser than this body thus it start to flow upward along the ice shelf bottom. This movement produces a shearing between stagnant interior water and the moving water in the mixed layer which induces a turbulent mixing at the interface. This process entrains warm and saline water in the mixed layer and can sustain melting along the path of the water (Little et al., 2009). Depending on the slope, water moves slower or faster and it affects the shearing, hence the rate of entrainment. Therefore, the melting is generally sustained along the steep slope. In their model configuration, Little et al. (2009) show that increasing the slope of the ice shelf cavity by 40% is as efficient as increasing by 1 °C the temperature in the interior of the ice shelf cavity.

Considering a shallow shelf 2D model, the profile of the bottom of the ice shelf will be parabolic in the case of a freely floating ice tongue and linear if lateral drag is added in the model, i.e. an ice shelf confined in a bay (Van der Veen, 2013). In the first case, the potential of melting is high near the grounding line and is nearly absent further downstream. In the second case, this potential is constant all along the flowline. However, these are two ideal cases in two dimensions. The profile of an ice shelf depends on multiple parameters such as melting, divergence, lateral drag and buttressing. Therefore each ice shelf has a different temperature to melt relationship because of the diversity of geometric profile.

1.2.2.3 Mass balance estimation

As previously mentioned, Vaughan et al. (2013) average data from ten studies to assess the mass balance of Antarctica. These estimations are based on several methods: satellite gravimetry which measures the change in gravity field, satellite altimetry which measures the surface evolution of the ice sheet and the input/output method (IOM) which evaluates input and output of each drainage basins and integrate them. None of them are free from errors and all have to rely on either models or approximations (Shepherd et al., 2012). Satellite gravimetry and altimetry measure the absolute mass change but rely on glacial isostatic adjustment (GIA) model. As most of the drainage basins

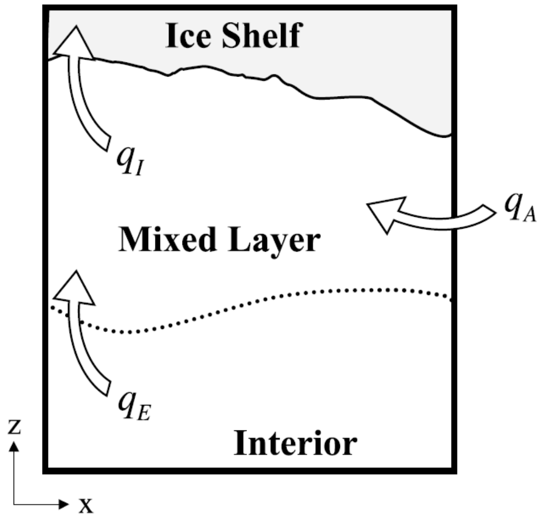

FIGURE 1.6: Zoom on the mixed layer. The arrows represents the fluxes of heat. q_A is the advective flux carried from upstream in the mixed layer, q_I is the heat flux toward the ice and q_E is the entrained heat flux driven by the shearing between the mixed layer and the interior of the ice shelf cavity. Note that the orientation is reversed compare to Figure 1.5. This figure is reproduced from Little et al. (2009)

in East Antarctic Ice Sheet (EAIS) are close to the equilibrium, these methods struggle to come up with good estimations, as a small error in the GIA model causes big relative errors in the results (Hanna et al., 2013). The altimetry also depends on the firn densification process which is still hard to model.

The input/output method (IOM) calculates the balance between the area-integrated surface mass balance (SMB) that feeds a given drainage basin and the loss of ice through ice discharge at the basin outlet (contact with the ocean). Nevertheless, a recent IOM study (Zwally and Giovinetto, 2011) emphasizes that the IOM is equally prone to a large uncertainty. Indeed, the method is highly sensitive to the choice of the surface mass balance (SMB) as input parameter. At present, several SMB datasets are available, either based on regional atmospheric modelling (Lenaerts et al., 2012, van de Berg et al., 2006) or on data assimilation methods (Arthern et al., 2006). Lenaerts et al. (2012) compare several datasets and identify a discrepancy up to 15%, which is >300 Gt $a^{-1}$for the whole Antarctic ice sheet.

The IOM has another pitfall. It is common to set the flux gate seaward of the grounding line, assuming that the glacier reaches hydrostatic equilibrium at the grounding line and ice thickness does not change significantly between the grounding line and the point where the ice shelf actually reaches a hydraulic equilibrium. Moreover, they can be separated by several kilometres (Bindschadler et al., 2011b). This is a major drawback, since intense subglacial melting occurs at the seaward side of the grounding line, well up to several tens of meters per year (Dutrieux et al., 2013, Payne et al., 2007), which is an order of magnitude higher than the local SMB. It is therefore recommended to calculate the outflow slightly upstream of the grounding line. Unfortunately, this leads to a bias in ice thickness (if direct observations are lacking) and, secondly, it is now necessary to consider ice dynamics since the independence of flow speed with depth (plug flow) is not fully valid any more. Vaughan et al. (2013) consider that incomplete ice thickness mapping still causes uncertainties in ice discharge of 2 to 15% in Antarctica.

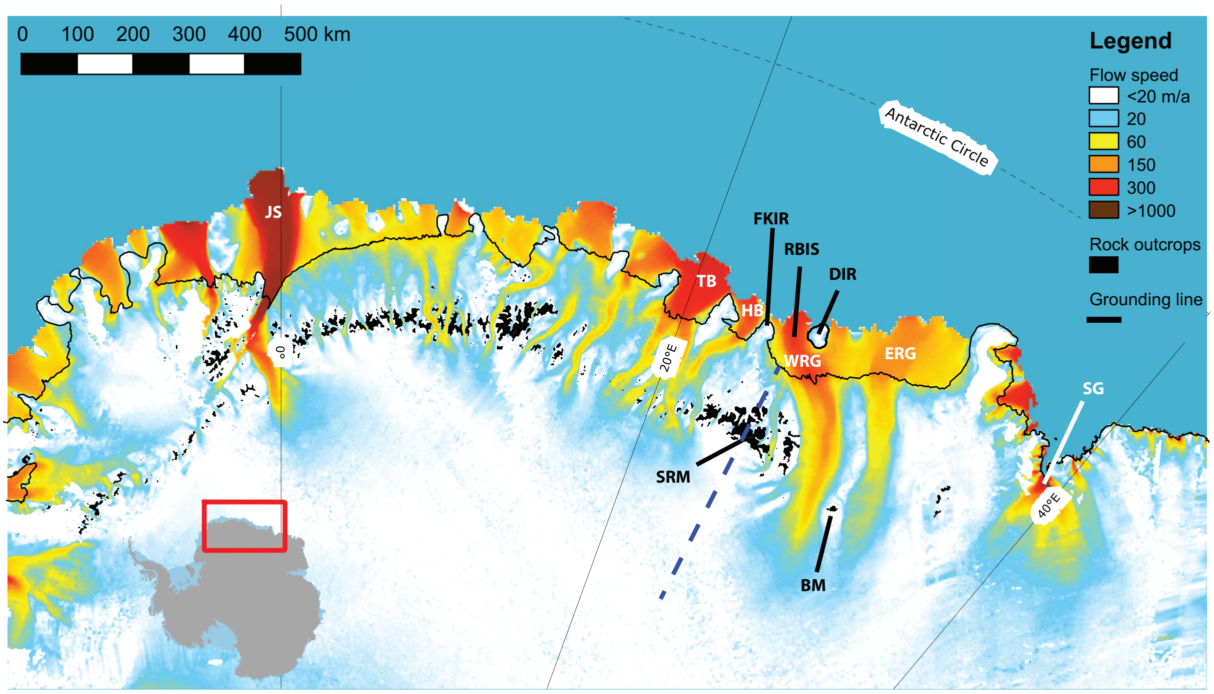

FIGURE 1.7: Map of the Dronning Maud Land. The background is the surface speed of the ice (Rignot et al., 2011a). The rock outcrops are shown in black (SCAR, 2012). The grounding line (black line) is from Bindschadler et al. (2011b) except for the grounding line of Derwael Ice Rise (DIR) which was manually picked. The annotations in white are the glaciers mentioned in this theses : Jutulstraumen (JS), Tussebreen (TB), H.E. Hansenbreen (HB), West Ragnhild Glacier (WRG), East Ragnhild Glacier (ERG) and Shirase Glacier (SG). The other geographical features are the Sør Rondane Mountains (SRM), the Belgica Mountains (BM), the Roi Baudouin Ice Shelf (RBIS) and the FranKenny Ice Rise (FKIR). The blue dashed line denotes the profile of Figure 1.8. The red box on the small map of Antarctica (bottom left) is the extent of the bigger map. This map and a large part of the next ones are made with Quantarctica database (www.quantarctica.org).

1.3 Data Collection

1.3.1 Geographical Settings

Dronning Maud Land (DML) is located in East Antarctica along the coast of Atlantic and Indian Ocean between 20° W and 45° E. This region is characterized by an elevated plateau and a relatively low coastal region separated by mountainous arc about 150 km inland (Figure 1.7). These mountains dam the ice flow (Figure 1.8) which is concentrated into few narrow trunks, the outlet glaciers. In DML, these glaciers flow into ice shelves embedded in small embayments which generate lateral friction. This friction buttresses the flow of the glaciers. In this part of Antarctica, there are 3 major outlets : Jutulstraumen, West Ragnhild Glacier (WRG) and Shirase. They discharge $14.2\,\mathrm{Gt\,a^{-1}}$(Høydal, 1996), $10.4 \pm 0.6\,\mathrm{Gt\,a^{-1}}$ (Chapter 2) and $13.8 \pm 1.6\,\mathrm{Gt\,a^{-1}}$; (Pattyn and Derauw, 2002), respectively. In this thesis, we will focus on the WRG and the surrounding area, i.e. the Sør Rondane Mountains (SRM), the glaciers flowing around it and the associated ice shelves.

The size of the ice sheet is quite constant in time. Mackintosh et al. (2014) show evidence that nunataks of the SRM was free of ice at least until 200,000 years ago. This shows that the ice sheet did not massively thicken during the last glaciation. In the contrary, the grounding line during the

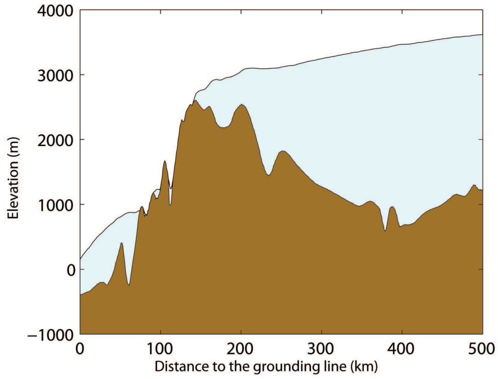

FIGURE 1.8: Profile of the geometry of the ice sheet along the dashed blue line in Figure 1.7. Brown is the bedrock and light blue is the ice sheet (Fretwell et al., 2013). The grounding line is on the left and the ice divide is on the right.

last glacial maximum was located significantly further north: along the continental shelf (Anderson et al., 2002).

Roi Baudouin Ice Shelf (RBIS) is the floating part of the WRG. It flows between two ice rises : Derwael Ice Rise (DIR) and an unnamed ice rise located 24°E (Figure 1.7 and 1.9), hereafter called FranKenny Ice Rise (FKIR). They exert lateral friction on RBIS. A closer analysis of the region shows that a smaller ice rise (PP1 on Figure 1.9, 24.5°E) may play a dominant role.

1.3.2 Inventory of the measurements

Since 2008, intensive data collection was performed in the region of the Roi Baudouin Ice Shelf (Figure 1.9). The opening of the Princess Elisabeth Station is obviously a trigger of the interest for the region. Nevertheless RBIS is a good case study of the ice shelves in Dronning Maud Land: a major glacier flows into it, it is buttressed by two big ice rises and its front is close to the continental shelf allowing interaction between ocean and its cavity. These reasons led us to collect data on and around RBIS to better understand if it is stable or not. Data collection was spread over several campaigns.

The first campaign took place in 2008. This mission had two aspects : a geophysical survey (GPS and low-frequency radar[4]) was made on the FranKenny Ice Rise, and several ice cores were drilled in and around a rift located north of this ice rise (White dot around 24°E on Figure 1.9). In 2010, FKIR was revisited as well as the Derwael Ice Rise (≈ 26.5°E). Again, GPS and low-frequency radar survey were carried out. Another series of cores were made in the surrounding of the rift.

In the framework of of a EUFAR project, the Alfred Wegener Institute (AWI) performed in January 2011 an airborne radio-echo sounding survey of 4 outlet glaciers (blue line on Figure 1.9). The aim was to map the bedrock topography beneath them.

In December 2011, within the framework of the BELISSIMA project, Katie Leonard made 11 Conductivity-Temperature-Depth (CTD) soundings in front of RBIS (yellow dots on Figure 1.9) to evaluate the physical properties of the water bodies which interact with the ice shelf cavity.

[4]For a description of radar use in glaciology, see Appendix A

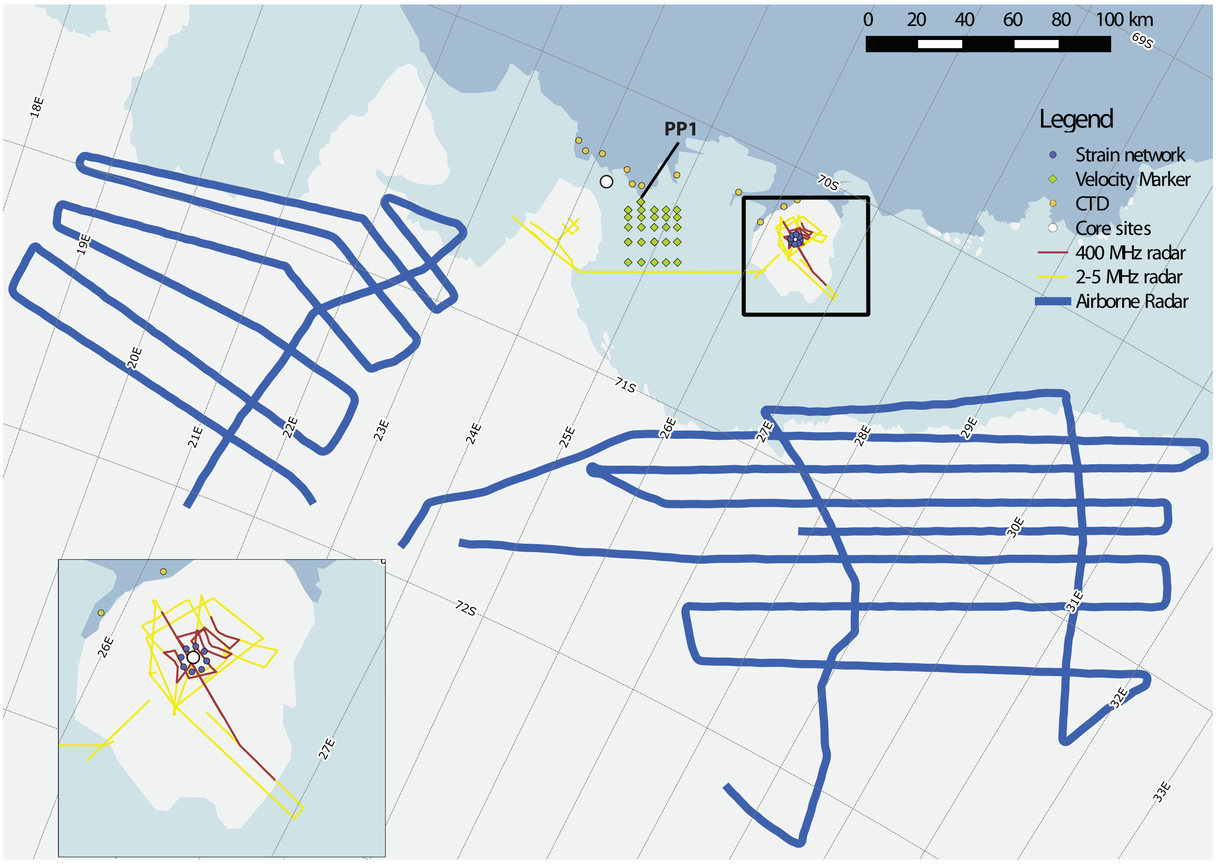

FIGURE 1.9: Inventory of the data collected around RBIS during the last few years.

Finally, in the framework of the ICECON project, an important field campaign was organised in 2012. We made a comprehensive survey of the DIR. The target was the Raymond bump[5] previously observed and the processes leading to its formation. At the ice divide, a 120-m deep ice core was drilled. Installation of a continuous geodetic GPS at the same place was a main achievement of the ICECON project as well as five devices to measure compaction rate at different depth. We did a geophysical survey of the surrounding of the Raymond bump with 400 MHz and 2 MHz radar. The former one is to evaluate the surface mass balance and the latter was used to map deep layers and bed topography. A few kilometres away of the divide, we installed 8 velocity markers (blue dots) to estimate the strain rate at the core site. These have to be reoccupied to measure the relative change from one year to another.

In the meanwhile, the InBev-Baillet Latour project, Be:Wise, took place on the RBIS few kilometres upstream of a small ice rise hereafter named PP1. A grid of 26 velocity markers was set up (green diamonds) and we made radar measurements (400 MHz and 5 MHz) and GPS survey between them (not shown on the map to avoid overloading). The aim was to understand the influence of PP1 on the ice shelf flow.

All of these data are mentioned for completeness. I will not explicitly use data from all these surveys and projects, but they help to understand the big picture drawn in Chapter 5. My main contributions are based on the geophysical surveys that I combined with ice flow modelling to retrieve the boundary conditions of the ice sheet.

[5]A Raymond bump is an anticline observed in the ice beneath the divide due to the difference in rheology between there and the margins.

1.4 Aim of the thesis

As we saw, sea level rise contributions are still largely unknown. Efforts have to be done on quantifying the relative importance of the contributors. This thesis was designed to partly answer this question through a comprehensive study of the mass balance and ice dynamics of Dronning Maud Land, its ice streams, ice shelves and ice rises.

In the latest study of Antarctic mass balance, the mass balance of the Sør Rondane Mountains glacial system is assumed to be at equilibrium (Shepherd et al., 2012). This assumption is made because of the lack of thickness data close to the grounding line and is based on the conviction that no change occurs in this part of Antarctica. In this thesis, we re-evaluate this hypothesis thanks to a new airborne radar survey which reveals the geometry of the grounding line. Via an input/output method, we assess the mass balance of the 4 major outlet glaciers flowing around the SRM.

The budget of a glacier is partly governed by its dynamics. If a collapse of the frontal ice shelf occurs, the glacier will significantly accelerate affecting the mass balance negatively until it reaches a new equilibrium state. These equilibrium positions depends on the geometry. Therefore, we investigate the geometry of the West Ragnhild Glacier, the biggest outlet glacier in the region, to evaluate its sensitivity to change at its boundaries. The nature of the bed and its flow regime are also investigated to draw a complete description of the dynamics of the WRG.

Finally, another aspect of the input/output method is the use of a dataset of the surface mass balance. Unfortunately, these datasets have coarse resolution: tens of kilometres. We will show that the SMB can vary by a factor of three within one grid cell of these datasets. This conclusion is drawn on the basis of a geophysical survey made across the Derwael Ice Rise which emphasizes the impact of the surface topography on the SMB.

This thesis is organized in four chapters. The three first are scientific contributions to peer-reviewed journals as they were published. The last one is a comprehensive summary of the recent advance in understanding the behaviour of this region.

Chapter 2

Mass balance of the Sør Rondane Glacial System, East Antarctica

Submitted by D. Callens, N. Thonnard, J. T.M. Lenaerts, J. M. van Wessem, W.J. van de Berg, K. Matsuoka, F. Pattyn, in Annals of Glaciology, 2014.

Mass changes of polar ice sheets have an important societal impact, because they affect global sea level. Estimating the current mass budget of ice sheets is equivalent to determining the balance between the surface mass gain through precipitation and the outflow across the grounding line. Especially for the Antarctic ice sheet, the latter is governed by oceanic processes and outlet glacier dynamics. In this study, we computed the mass budget of major outlet glaciers in the Eastern Dronning Maud Land sector of the Antarctic Ice Sheet using the input-output method. Input is given by recent surface accumulation estimations (SMB) of the whole drainage basin. The outflow at the grounding line is determined from the radar data of a recent airborne survey and satellite-based velocities using a flow model of combined plug flow and simple shear. This approach is an improvement over previous studies, as the ice thickness is measured and not estimated from hydrostatic equilibrium. In line with the general thickening of the ice sheet over this sector, we estimate the regional mass balance in this area to be 3.15±8.23 Gt a^{-1} according to the most recent SMB model results.

2.1 Introduction

Precise knowledge of the mass balance of ice sheets is essential for estimating their contribution to current and future sea level rise. The numerous assumptions necessary to assess the global mass balance of Antarctica lead to significant discrepancies between the bulk of estimations (Rignot et al., 2011c, Zwally and Giovinetto, 2011). The IMBIE consortium (Shepherd et al., 2012) reconciled results from a range of different methods (Input/Output Method (IOM), satellite altimetry and gravimetry) to determine that the average mass loss of the entire Antarctic ice sheet over the period 1992–2010 was 71±53 Gt a^{-1}. During this period, the East Antarctic Ice Sheet (EAIS) mass change might be positive (+14±43 Gt a^{-1}), whilst the West Antarctic Ice Sheet (WAIS) and Antarctic Peninsula Ice Sheet (APIS) lost mass (−65±26 and −20±14 Gt a^{-1}). While the magnitude of change of WAIS and APIS are therefore relatively well constrained, even the sign of the sea level rise contribution from EAIS remains uncertain.

A significant issue of mass change estimation is that none of the methods presently used are free from significant errors, and all rely on either models or approximations (Shepherd et al., 2012). The IOM calculates the balance between the total surface mass balance (SMB) that feeds a given drainage basin and the loss of ice through ice discharge at the basin outlet (e.g., Rignot et al., 2008). Satellite gravimetry and altimetry (e.g., Gunter et al., 2009) measure the absolute mass change but rely on glacial isostatic adjustment (GIA) models and altimetry also suffers of uncertainty due the densification process. As most of the drainage basins in EAIS are close to the equilibrium (Shepherd et al., 2012), these methods struggle to fulfil good estimations, because a small error in the GIA model will introduce large relative errors in the results (Hanna et al., 2013).

Nevertheless, a recent IOM study (Zwally and Giovinetto, 2011) emphasizes that the IOM is equally prone to a large uncertainty. Indeed, the method is highly sensitive to the choice of the surface mass balance (SMB) as an input parameter. At present, several SMB datasets are available, either based on regional atmospheric modelling (van de Berg et al., 2006, Van Wessem et al., 2014) or on data assimilation methods (Arthern et al., 2006). Lenaerts et al. (2012) compare several datasets and identify a discrepancy up to 15%, which is >300 Gt a^{-1} for the whole Antarctic ice sheet.

The IOM has another pitfall. When no thickness data are available, the flux gate is set seaward of the grounding line, with the ice thickness then derived from the ice surface elevation. This method assumes that the glacier reaches hydrostatic equilibrium a few kilometres beyond the grounding line and that ice thickness does not change significantly between the grounding line and the point where the ice shelf actually freely floats. These can be separated by several kilometres, however, so this assumption may not be correct. For instance, along the Ragnhild coast (East Antarctica), the grounding line and hydrostatic line are ≈ 2 km apart (Bindschadler et al., 2011b). Within this interval, intense and localised subglacial melting of up to several tens of meters per year can occurs at the seaward side of the grounding line (Dutrieux et al., 2013, Payne et al., 2007) and may represent an important sink of mass which will affect the mass balance estimation. This is one order of magnitude higher than the local SMB and will introduce a significant error into the mass balance calculations. Moreover, any error in ice shelf surface elevation is multiplied by a factor of ten when translated into ice thickness. An alternative to this approach is to calculate the outflow slightly upstream of the grounding line. Unfortunately, this will lead to two potential problems: (i) , if radar measurements are not available, there is no remote sensing method to estimate the thickness of the grounded ice; and (ii) ice dynamics must now be considered since the independence of flow speed with depth (plug flow) is no longer valid.

Within the eastern Dronning Maud Land (DML) sector of the EAIS, only a limited number of previous glaciology studies have been carried out. Van Autenboer and Decleir (1978) estimated the mass balance of the glaciers in the Sør Rondane Mountains (SRM), but their study was limited

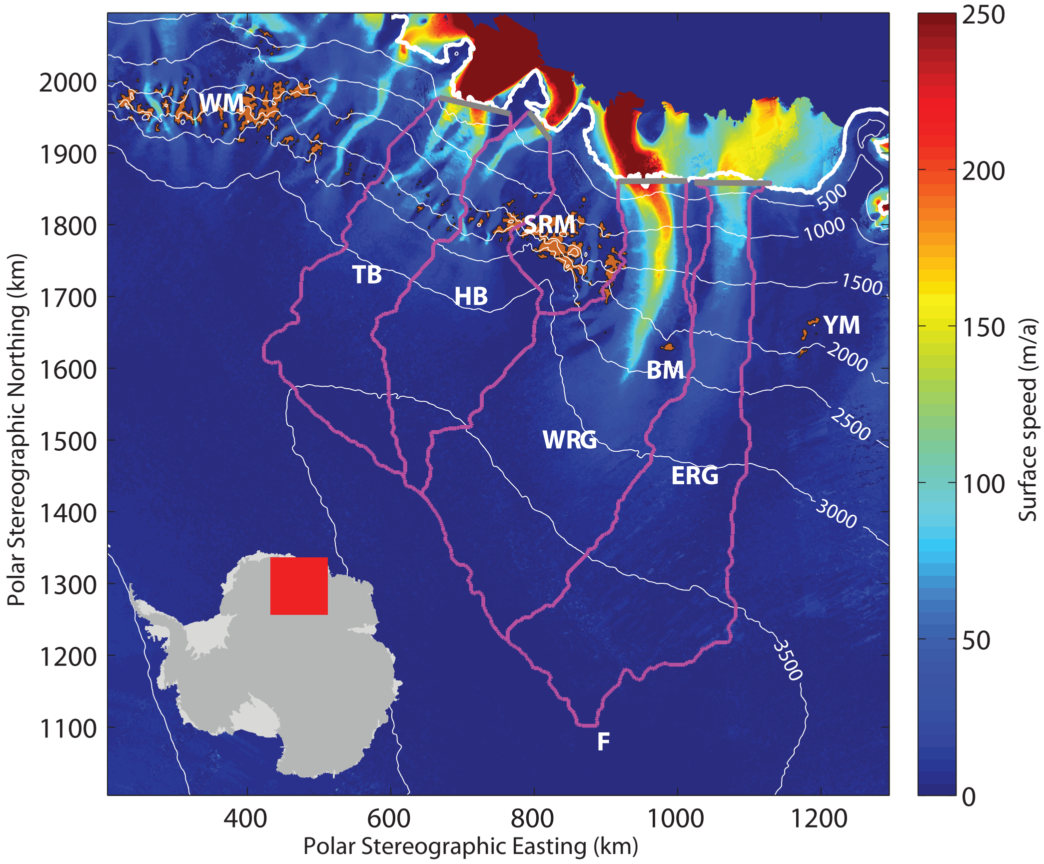

Figure 2.1: Map of the Sør Rondane Mountains glacial system. Background colour shows the surface flow speed (Rignot et al., 2011a). Contours show surface elevations (Bamber et al., 2009). The four drainage basins are in purple. Their downstream section (grey line) is the output gate used to determine the basin extension and the outflux. These are the gates surveyed by the radar and presented in Figure 2.2. Rock outcrops are shown in brown (SCAR, 2012). White line is the grounding line (Bindschadler et al., 2011b). SRM stands for Sør Rondane Mountains; WM, Wohlthat Massif; BM, Belgica Moutains; YM, Yamato Mountains and F depicts the Dome Fuji. The glaciers acronyms are: TB is Tussebreen, HB is H.E. Hansenbreen, WRG is West Ragnhild Glacier and ERG is East Ragnhild Glacier. With exception of H.E. Hansenbreen, none of these glaciers' names are official, but a number of them have been frequently used in the literature (e.g., Pattyn et al., 2005).

to the smaller glaciers within the mountain range, and does not include the primary ice flow outlets that flow through and are diverted around the major coastal mountain systems. On a continental scale, a number of studies have established the mass balance of DML drainage basins. The most recent ones are due to Rignot et al. (2008) and Shepherd et al. (2012). Along Ragnhild coast, Rignot et al. (2008) base their analysis on the flux through the ice shelf, where ice thickness is determined from hydrostatic equilibrium. Shepherd et al. (2012) assume the ice sheet in this area to be in equilibrium, since thickness data at the grounding line are lacking. In the meanwhile, GRACE (gravimetry) and Ice-Sat (altimetry) reconstruction of the mass budget do not agree in Eastern DML (Gunter et al., 2009). Furthermore, King et al. (2012) identify a trend statistically positive with 95% confidence for the mass balance of the basin between Jutulstraumen and East Ragnhild Glacier.

In this paper, we present the first estimate of the mass balance of the entire SRM glacial system using IOM. To avoid bias associated with the assumption of hydrostatic equilibrium, we base our calculations on data from an airborne radar survey which determined the ice thickness of the outlet gates slightly upstream of the grounding line. We then compare different datasets of SMB to investigate the impact of SMB uncertainties on the overall result.

2.2 Geographical setting

The Sør Rondane Mountains glacial system consists of four large outlet glaciers which flow from the Dome Fuji ice divide toward the Ragnhild coast, Dronning Maud Land (Figure 2.1). West of the SRM are Tussebreen (TB) and H.E. Hansenbreen (HB; both between the Wohlthat Massif and the SRM). To the east, there are the West Ragnhild Glacier (WRG; Callens et al., 2014, Pattyn et al., 2005) between SRM and the Belgica Mountains, and the East Ragnhild Glacier (ERG) between the Belgica and Yamato Mountains. The position of these glaciers as well as the surface flow speed (Rignot et al., 2011a) are shown in Figure 2.1.

2.3 Methods

2.3.1 Ice thickness measurements

To map the ice thickness at the grounding line, an airborne radio-echo sounding survey in the area was carried out during the austral summer 2010–2011 (Callens et al., 2014). The survey consisted of a series of cross-flow profiles, of which one close to the grounding line of each of the glaciers (Figure 2.1), as well as a longitudinal profile along the flowline. The radar system employed a 150 MHz centre frequency (Nixdorf et al., 1999, Steinhage et al., 2001). The system recorded at a rate of 20 Hz. For further signal to noise improvement, the data were ten folds stacked, resulting in a horizontal resolution of 80 $\pm$ 20 m. The data are processed like in Nixdorf et al. (1999).

Ice thickness was derived using a constant radio-wave propagation speed of 168 m μs^{-1}. The uncertainty in thickness estimation is approximately $\pm$30 m (Steinhage et al., 1999). Surface elevation was obtained by laser altimetry from the aircraft, and bed elevation was subsequently derived by subtracting the ice thickness from the surface elevation. We applied the geoid height of 20 m above the EGM96 ellipsoid (Rapp, 1997) to derive the surface and bed elevations relative to sea level[1].

The cross profile geometry as well as the ice flow speeds are displayed in Figure 2.2.

2.3.2 Surface mass balance

We determine the outlines of each drainage basin by backtracking flowlines from the out-flux gate boundaries near the grounding line in the upstream direction[2]. Starting from the grounding line, we trace flowlines on a surface digital elevation model (Bamber et al., 2009) until their convergence at the ice divide. We assumed that ice follows the steepest surface slope. A second step consists of integrating the SMB over each of the drainage basins. The SMB datasets used originate from van de Berg et al. (2006), Arthern et al. (2006) and Van Wessem et al. (2014); they are hereafter referred to as B06, A06 and W14. A06 is a dataset based on interpolation of ground-based observations (spanning span from 1950 to 2000) with a satellite derived distribution. B06 is derived from the RACMO2 model on ∼55 km spatial resolution, driven by ERA-40 reanalysis (1980-2004), and

[1] These data are available on Pangaea.
[2] The determination of the flux gates is given in the next section.

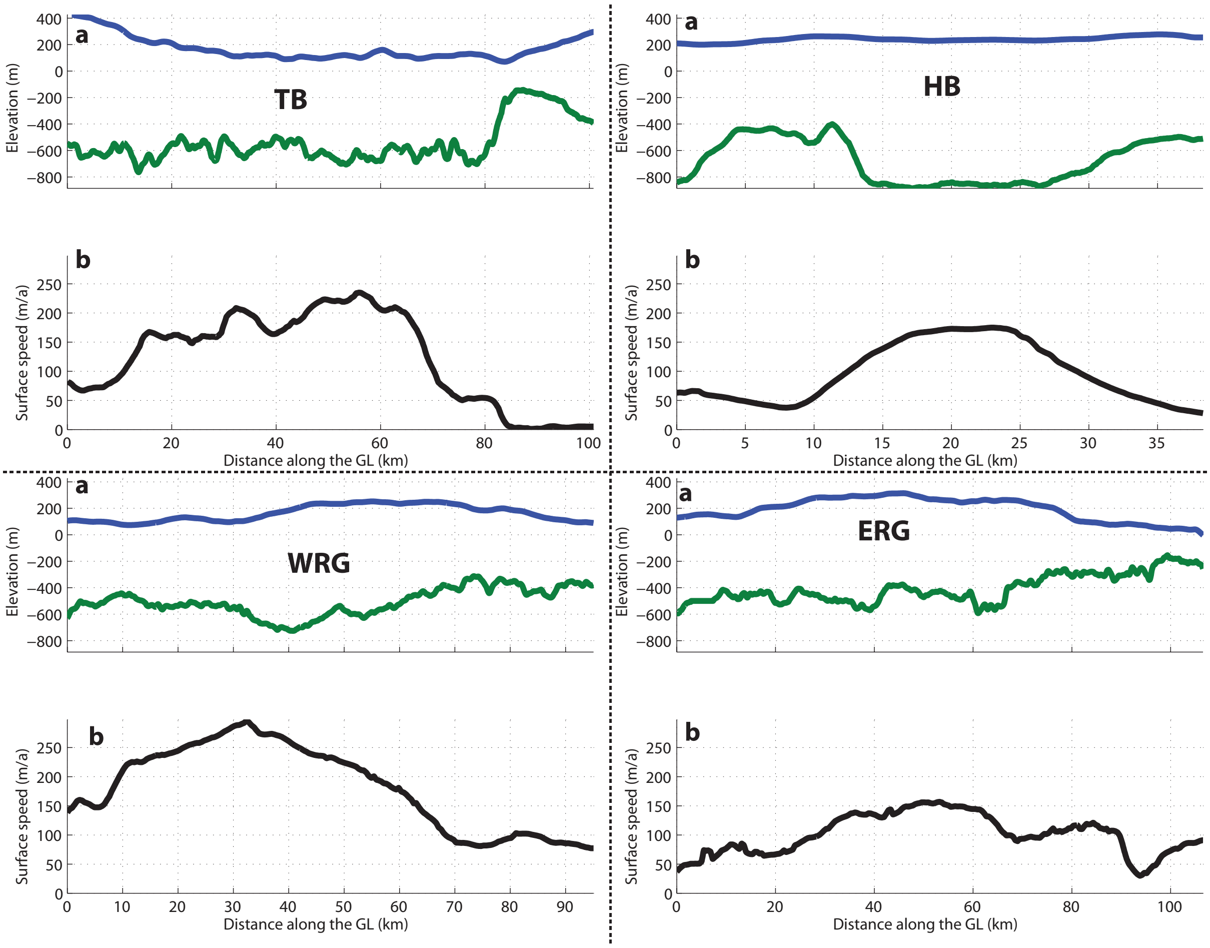

FIGURE 2.2: Geometry (a) and velocity (b) profiles along the flux gate of each glacier, oriented west to east. In panels (a), blue line is the surface elevation and green line is bed elevation. These data are described in the data section. In panel (b), black line is the surface speed from Rignot et al. (2011a). TB is Tussebreen HB is H.E. Hansenbreen, WRG is West Ragnhild Glacier and ERG is East Ragnhild Glacier.

calibrated with the use of ground-based measurements. W14 is also derived from RACMO2, on ∼27 km spatial resolution, driven by ERA-Interim reanalysis (1979–2013), without any *a posteriori* output calibration. We assume that the mean SMB values over these periods represent these SMB models and used them for the IOM calculations.

2.3.3 Outflow

The flux gates are defined along flight tracks of the airborne radar survey. They are aimed to cover a maximum of the flux within the limitation of the radar survey (Figure 2.2). However, as long as, the basin is determined by the flux gate, all the ice flowing through the flux gate is assumed to have accumulated in the associated basin. Since we prescribe the gate width, no errors are associated to this quantity.

To estimate ice flux, we use the surface velocities from Rignot et al. (2011a), taken upstream from the grounding line and coinciding with the airborne radar profiles. The velocities are projected perpendicular to these flight lines to account the fact that flowline is not exactly perpendicular to them: the norm of the velocity vector is multiply by the cosine of the angle between the normal of the gate and the velocity vector.

When the flux gate is set seaward of the grounding line, it is common to assume that ice flow speed is independent of depth (plug flow, equation 2.1) (Rignot et al., 2008):

$$\Phi = \int_{w}^{e} U_{\perp s}(y) H(y)\, dy \tag{2.1}$$

where Φ is the ice flux, $U_{\perp s}(y)$ denotes the surface speed perpendicular to the flux gate (Rignot et al., 2011a), H is the thickness, y the cross-flow direction and w and e denote the western and eastern boundaries of the gate. However, in this study, we set the flux gate on the grounded ice, where the ice flow speed can vary with depth, depending on the deformational characteristics. To assess mass balance uncertainty associated with the flow regime, we consider different possible types of flow. First, we assume a plug flow regime (2.1), where the mean ice flow speed equals the surface flow speed. Second, we introduce a combined plug/simple-shear flow regime in which the ice flow speed depends both on internal deformation and basal motion. For this purpose, we use the simplest way to describe ice flow according to simple shear, i.e., based on the so-called Shallow-Ice Approximation:

$$\overline{U}_{\perp d}(y) = \frac{2\varepsilon\overline{A}}{n+2} H(y)\, \tau_d^n(y)\ , \tag{2.2}$$

where $\overline{U}_{\perp d}$ is the depth–averaged deformational speed and $\tau_d(y) = -\rho g H(y)|\nabla z_s|$ is the driving stress. Other parameters in (2.2) are $\overline{A}$ and n, the depth-integrated temperature-dependent flow parameter and the exponent in Glen's flow law, respectively. ε is the enhancement factor, ρ is the ice density, g is the gravitational acceleration, and z_s is the surface elevation. Following Cuffey and Paterson (2010), $\varepsilon = 3$, $n = 3$ and $\overline{A} = 3.5.10^{-25}$ Pa^{-3} s^{-1}, so that $\overline{A}$ corresponds to a mean englacial temperature of -10°C. Finally the surface gradient (∇z_s) is derived from laser altimetry at the flowline and we assume that it is constant along the grounding line cross section, so that ice thickness (H) is the only spatially varying parameter in (2.2). In order to reduce flow coupling effects on short spatial scales, the surface gradients are calculated over approximately ten times the ice thickness (Kamb and Echelmeyer, 1986).

Once $\overline{U}_{\perp d}$ is determined, basal sliding ($U_{\perp b}$) is taken as the difference with the observed surface velocity. For the Shallow-Ice Approximation, this becomes (Cuffey and Paterson, 2010):

$$U_{\perp b}(y) = U_{\perp s}(y) - \frac{n+2}{n+1}\overline{U}_{\perp d}(y)\ . \tag{2.3}$$

The total mass outflux at the grounding line is thus a combination of the flux driven by basal motion and the one driven by internal deformation. This type of flow is hereafter named hybrid flow.

$$\Phi = \int_{w}^{e} \big(U_{\perp b}(y)\, H(y) + \overline{U}_{\perp d}(y)\, H(y)\big)\ \mathrm{d}y\ . \tag{2.4}$$

2.3.4 Error calculation

For the SMB datasets W14 and B06, the uncertainty in modelled SMB is derived from a comparison with 153 available SMB observations (such as stake measurements, ice core studies and automatic weather stations) over the entire northeastern Dronning Maud Land (70–77°S, 0–65°E; van de Berg et al., 2006). For each of the SMB observations, a comparison with modelled SMB is performed, and the total SMB uncertainty at each location is assumed to be the absolute difference between both values. This uncertainty can be ascribed to both an uncertainty in observation and in the model. Uncertainties on observed SMB are assumed to be linearly proportional to the SMB itself such as in Rignot et al. (2008). The remaining uncertainty, the one ascribed to the model, is calculated as the square root of the difference between the quadratic total uncertainty and the quadratic observational uncertainty. The resulting 153 model mismatches are then averaged.

Since A06 is based on an interpolation of ground-based SMB measurements, this dataset is not independent of these measurements; in this case, we cannot assume that the A06 error constitutes of an independent observational and model error. Therefore we assume a spatially homogeneous error of 10% over the entire basin according to Arthern et al. (2006).

In order to calculate error on mass outflux, we only consider the error on the measured quantities: ice thickness ($E_H = \pm$ 30 m) and surface flow speed (E_{U_s} from Rignot et al. (2011a)). The error on the flux estimation under the assumption of plug flow is given by

$$E_\Phi = \int_w^e \left(E_{U_{\perp s}}(y)H(y) + E_H U_{\perp s}(y)\right) \mathrm{d}y \; . \tag{2.5}$$

For hybrid ice flow, error propagation leads to

$$E_\Phi = \sqrt{\left(\int_w^e \left(E_{U_{\perp b}}(y)H(y) + E_H U_{\perp b}(y)\right) \mathrm{d}y\right)^2 + \left(\int_w^e \left(E_{\overline{U}_{\perp d}}(y)H(y) + E_H \overline{U}_{\perp d}(y)\right) \mathrm{d}y\right)^2} \; , \tag{2.6}$$

where

$$E_{U_{\perp b}}(y) = \sqrt{E_{U_{\perp s}}(y)^2 + E_{\overline{U}_{\perp d}}(y)^2} \; , \tag{2.7}$$

and

$$E_{\overline{U}_{\perp d}}(y) = -\frac{2(n+1)\varepsilon\overline{A}}{n+2} \left(\rho g H(y)|\nabla z_s|\right)^n H(y)^n E_H \; . \tag{2.8}$$

The error on mass balance is the quadratic mean of the error on input and output.

2.4 Results

2.4.1 Surface mass Balance

The backtracking of flowline produces four large drainage basins which extend from the grounding lines toward Dome Fuji ice divide (Figure 2.1). Table 2.1 lists the characteristic sizes of each of the drainage basins.

Table 2.1: Basin extent and flux gate width for the adjacent drainage basins

Glacier	Area (km^2)	Gate width (km)
Tussebreen	64 292	100.8
H.E. Hansenbreen	61 542	38.3
West Ragnhild Glacier	117 104	95.0
East Ragnhild Glacier	102 125	106.5

The three mass input estimates are consistent between each other: they are bounded between 30.2 and 32.1 Gt a^{-1}. Their spread is about 6% of the total SMB. Table 2.2 also presents the errors on the estimation. These were calculated following the method described in the previous section and are based on the comparison between results of the model and 153 point measurements in DML. The specific surface mass balance is used in this calculation and is expressed in terms of SMB per area (i.e. mm w.e m^{-2} a^{-1}). For W14, the error on modelled SMB is equal to 19.2 mm w.e m^{-2} a^{-1} which corresponds to 26 % of the mean of the observations (73.7 mm w.e m^{-2} a^{-1}).

We assigned this relative error to the error on the area-integrated SMB. Therefore, the relative SMB uncertainty is of the order of 26%, which we apply to the entire SRM glacial system and to the individual basins. The agreement of B06 with observations is similar. The error is 21.0 mm w.e m^{-2} a^{-1}, yielding a relative SMB uncertainty of 28%. Figure 2.3 shows both RACMO2 based SMB datasets (B06 and W14) compared to observations. B06 tend to underestimate SMB at the locations of in situ measurements. The median of the difference between models and observations is -14 mm w.e. m^{-2} a^{-1} whereas W14 does not misestimate since its median is equal to -2 mm w.e. m^{-2} a^{-1}.

TABLE 2.2: Results of the mass budget (Gt a^{-1}) using three different SMB and 2 flow regimes. TB is Tussebreen, HB is H.E. Hansenbreen, WRG is West Ragnhild Glacier and ERG is East Ragnhild Glacier. A06, B06 and W14 refer to Arthern et al. (2006), van de Berg et al. (2006) and Van Wessem et al. (2014), respectively. PF=plug flow; HF=hybrid flow.

		TB	**HB**	**WRG**	**ERG**	**Total**
SMB	A06	6.90 ± 0.69	6.50 ± 0.65	10.60 ± 1.06	8.10 ± 0.81	32.10 ± 3.21
	B06	8.20 ± 2.30	4.50 ± 1.26	10.30 ± 2.88	7.20 ± 2.02	30.20 ± 8.46
	W14	8.82 ± 2.29	5.23 ± 1.36	11.03 ± 2.87	6.39 ± 1.66	31.47 ± 8.18
Outflow	PF (eq. 2.1)	8.01 ± 0.58	3.31 ± 0.16	10.98 ± 0.50	6.02 ± 0.32	28.32 ± 0.85
	HF (eq. 2.4)	7.70 ± 0.73	3.22 ± 0.22	10.82 ± 0.61	5.82 ± 0.47	27.55 ± 1.08
Mass Budget	A06 - PF	-1.11 ± 0.90	3.19 ± 0.67	-0.38 ± 1.17	2.08 ± 0.87	3.78 ± 3.32
	B06 - PF	0.19 ± 2.37	1.19 ± 1.27	-0.68 ± 2.93	1.18 ± 2.04	1.88 ± 8.50
	W14 - PF	0.81 ± 2.37	1.92 ± 1.37	0.05 ± 2.91	0.37 ± 1.69	3.15 ± 8.23

Errors are significantly higher for B06 and W14 than A06 due to the different methodologies used to calculate the error. For B06 and W14, we compared model to point measurements and evaluate the discrepancy. The uncertainty on A06 is set to 10% as stated in A06. However, their continent-wide error estimate not necessarily reflects the local errors.

2.4.2 Outflow

Depending on the assumption with respect to ice dynamics (plug flow-simple shear), the total outflux varies from 27.55 to 28.32 Gt a^{-1}. The errors were calculated using the method described in Eqs (2.5) to (2.8). They are significantly lower than uncertainties in SMB. At basin level, the mass outflux is a function of the width, the thickness and the flow speed (equations 2.1 and 2.4). As revealed by the size of H.E. Hansenbreen, the gate width is a first order parameter in the calculation of the outflow. However, Tussebreen, West Ragnhild Glacier and East Ragnhild Glacier have the same width but the outflow from the latter is 55% of the amount drained by WRG. This large discrepancy is due to the much higher ice flow speed across the grounding line of WRG (and of TB to a lesser extent). Ice flow speeds of WRG and TB are up to 298 and 245 m a^{-1}, respectively, while the flow speed of ERG does not exceed 152 m a^{-1}.

Concerning the comparison between plug and hybrid flow, the differences remain very small and, in all cases, less than the uncertainties. Therefore, in the mass balance calculation we will neglect the hybrid flow part and continue with considering only plug flow, because plug flow is the most likely flow type near grounding lines. The low value of ∇z_s (ranging from 11.3 10^{-3} to 18.4 10^{-3}) and relatively small thickness lead to small flux due to the internal deformation. Indeed flux due to ice deformation (second term of eq. 2.4) is always one order of magnitude smaller than flux due

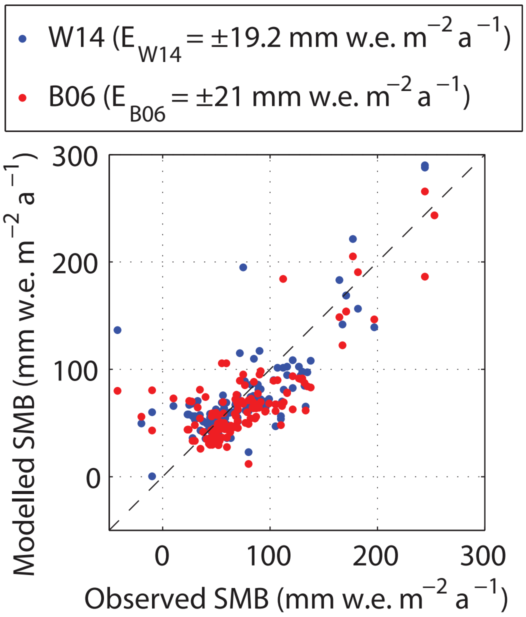

FIGURE 2.3: Comparison of the in-situ modelled SMB with the observations. E_{W14} and E_{B06} are the errors on the RACMO products calculates using the method described in the method section. The dashed line is the identity line.

to basal motion (first term of eq. 2.4). For instance, the former equals to $0.65\,\mathrm{Gt\,a^{-1}}$ while the later equals to $10.17\,\mathrm{Gt\,a^{-1}}$ in the case of WRG.

2.4.3 Mass Balance

From the difference between the mass gain through the integrated SMB and the mass loss through the gates, we find that the glacial system is slightly gaining mass, i.e., 1.88 to 3.78 Gt a^{-1}, depending on the SMB dataset used[3].

2.5 Discussion

The IOM shows consistently larger errors for the three SMB datasets that are used. All datasets give a consistent signal in terms of mass, which is also consistent over the different drainage basins we considered in this study. In general, A06 gives a higher total SMB compared to the datasets based on modelling, but overall results are comparable. B06 and W14 have same order of uncertainty while A06 has a significantly lower error. This is due to the methodology to ascribe errors on SMB estimate. As we cannot compare A06 with data since it is an interpolation of them, we have to rely on error estimate provided by Arthern et al. (2006): maximum 10%. Nevertheless, the errors on SMB represent for each scenario the majority of the uncertainty.

Smallest errors are found on the outflow, which is expected: the size of each basin is consistently dependent on the size of the outflow gate, and the latter has been well defined from the airborne radar data along the grounding line. For the mass outflow, the assumption of plug flow compared to the hybrid approach seems acceptable. The difference between plug flow and hybrid flow is

[3]In Appendix B, we present results of flux estimation downstream of the grounding line using the commonly accepted hydrostatic equilibrium assumption.

never larger than the calculated uncertainty (Table 2.2). As shown in Callens et al. (2014), the ice flow in the downstream section of West Ragnhild Glacier is primarily governed by basal sliding, so that plug flow is an adequate approximation, also upstream of the grounding line. This statement seems acceptable for the other glaciers since basal motion dominate the flux. Even if the use of the Shallow-Ice Approximation is not intrinsically valid for ice streams, it gives an end member estimation of how far the results can be from the plug flow assumption. The comparison supports the use of such assumption. The difference between plug and hybrid flow is never more than 5%, which is of the order of magnitude of the error. Indeed, the relatively low surface gradient ∇z_s implies a small driving stress even if the ice is thick, hence does not influence deformational ice flow. Therefore, the plug flow assumption can be safely applied in this situation.

Shepherd et al. (2012) show that the increasing mass balance observed in this area with GRACE between 2009 and 2011 is driven by a positive accumulation anomaly. However, this study made the assumption that the basins around SRM are in equilibrium because of the lack of data to state otherwise. Here, we estimate mass balance for mean SMB over the last 34 years (Arthern et al., 2006, van de Berg et al., 2006, Van Wessem et al., 2014) and outflow based on surface velocities between 2007 and 2009 (Rignot et al., 2011a) and a radar survey made in 2011. Based on these data, the SRM glacial system is slightly gaining mass. Given the mass budget of EAIS estimated by Shepherd et al. (2012), i.e. $+14\,\mathrm{Gt\ a^{-1}}$, and the fact that they assumed equilibrium for SRM glacial system, our new estimate of its mass budget, ranging from $+1.88$ to $3.78\,\mathrm{Gt\ a^{-1}}$ increases the continental mass budget by 13 to 27%, depending on the SMB dataset used. Unfortunately, large errors due to the SMB uncertainties do not allow to irrevocably conclude that SRM glacial system mass balance is positive.

2.6 Conclusions

Based on an airborne radar survey along and across the major outlet glaciers of the Sør Rondane mountains glacial system, grounding line ice thickness has been accurately mapped for the major outlet glaciers. We calculated the mass output of the four drainage basins constituted by these glaciers. The outflow is subsequently compared with the mass input from three different SMB datasets in order to assess their mass balance.

This study gives new insight of the mass balance in DML by contradicting the assumption of equilibrium previously made. According to the latest model and thickness measurements near the grounding line, this part of Antarctica gains 3.15 Gt of ice per year. However, given the large uncertainties and discrepancies in modelled SMB, no conclusions can be drawn relative to the mass balance of these drainage basins. Since they are almost in equilibrium, even small errors on SMB prevent to determine the sign of the contribution of the SRM glacial system to sea-level rise. At basin scale, it will be impossible to confidently assess the mass balance unless more reliable model emerged and number of SMB measurements drastically increases.

Chapter 3

Transition of flow regime along a marine-terminating outlet glacier in East Antarctica

PUBLISHED BY D. CALLENS, K. MATSUOKA, D. STEINHAGE, B. SMITH, E.WITRANT, AND F. PATTYN, IN THE CRYOSPHERE , 2014.

We present results of a multi-methodological approach to characterize the flow regime of West Ragnhild Glacier, the widest glacier in Dronning Maud Land, Antarctica. A new airborne radar survey points to substantially thicker ice (> 2000 m) than previously thought. With a discharge estimate of 11 Gt yr^{-1}, West Ragnhild Glacier thus becomes of the three major outlet glaciers in Dronning Maud Land. Its bed topography is distinct between the upstream and downstream section: in the downstream section (< 65 km upstream of the grounding line), the glacier overlies a wide and flat basin well below the sea level, while the upstream region is more mountainous. Spectral analysis of the bed topography also reveals this clear contrast and suggests that the downstream area is sediment covered. Furthermore, bed-returned power varies by 30 dB within 20 km near the bed flatness transition, suggesting that the water content at bed/ice interface increases over a short distance downstream, hence pointing to water-rich sediment. Ice flow speed observed in the downstream part of the glacier (~ 250 m yr^{-1}) can only be explained through very low basal friction, leading to a substantial amount of basal sliding in the downstream 65 km of the glacier. All the above lines of evidence (sediment bed, wetness and basal motion) and the relatively flat grounding zone give the potential for West Ragnhild Glacier to be more sensitive to external forcing compared to other major outlet glaciers in this region, which are more stable due to their bed geometry (e.g. Shirase Glacier).

3.1 Introduction

The overall mass balance of the Antarctic ice sheet is dominated by a significant mass deficit in West Antarctica (Pritchard et al., 2012, Rignot et al., 2008). This is primarily due to thinning and acceleration of glaciers (e.g. Pine Island Glacier; Joughin et al., 2003) mainly driven by the loss of buttressing from ice shelves (Schoof, 2010). Concurrently, the trend in East Antarctica is weaker. The East Antarctic ice sheet (EAIS) is only losing mass slightly, as increased surface accumulation compensates mass loss through outlet glaciers (Shepherd et al., 2012). While Miles et al. (2013) observe a link between front migration and climate forcing, a significant widespread thinning trend along the pacific coast of the EAIS remains lacking.

Although East Antarctica is mainly continental, limited observations in Dronning Maud Land (DML), show that the ice sheet seaward of the inland mountains lies on a bed well below sea level (BEDMAP2; Fretwell et al., 2013) and most of the ice from the polar plateau is discharged through numerous glaciers in between coastal mountain ranges. The ice-dynamical consequences of such settings have yet to be explored. In this paper we investigate the marine boundary of such a glacier system draining the EAIS in DML.

The coastal region of DML is characterized by numerous outlet glaciers feeding into ice shelves (Figure 3.1a). They are generally short in length but reach out to the continental shelf edge. The stability of these ice shelves is primarily ensured through the presence of ice rises and pinning points, making the ice shelf locally grounded. Potential unpinning of these ice shelves would inevitably lead to ice shelf speed up, which makes them sensitive to marine forcing.

Of all glaciers in DML, West Ragnhild Glacier is the widest ($\approx 90\,\mathrm{km}$) and longest. Its ice flow speed is already $100\,\mathrm{m\,yr^{-1}}$ 250 km upstream from the grounding line (Figure 3.1b). Based on

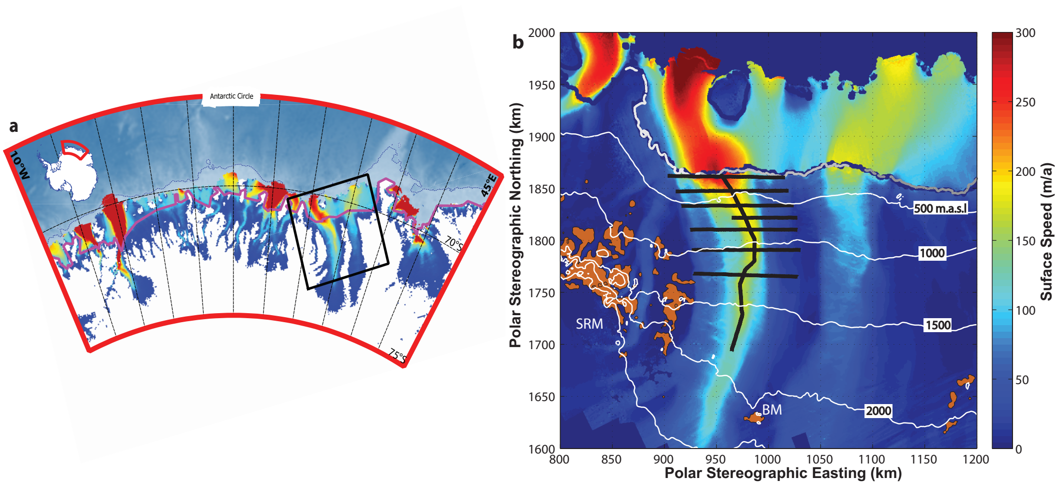

FIGURE 3.1: Overview map of West Ragnhild Glacier, Dronning Maud Land, East Antarctica. **(a)** Dronning Maud Land. Ice flow speed is shown on the same scale as for panel **(b)** (but white when $< 15\,\mathrm{m\,yr^{-1}}$; Rignot et al., 2011a). The grounding line is shown in purple (Bindschadler et al., 2011b). Rock outcrops are shown in brown (SCAR, 2012). The square shows the 400 $km \times$ 400 km area covered by the map on panel **(b)**. The inset shows the coverage of panel **(a)**. **(b)** West Ragnhild Glacier. Background colour shows the surface flow speed derived from satellite interferometry and speckle tracking. Contours show surface elevations at 500 m interval (Bamber et al., 2009). From west to east, the grounding line is defined on the basis of a pair of PALSAR images taken in 2007 (light grey) and two pairs of RADARSAT (middle grey and dark grey) taken in 2000 (Rignot et al., 2011b). Black lines are the longitudinal and transverse radar profiles. Rock outcrops as in **(a)**. SRM and BM stand for Sør Rondane Mountains and Belgica Mountains, respectively.

the ice thickness data presented in this paper, we estimate the grounding line mass flux to be 11 Gt yr^{-1}, which constitutes roughly 10 % of the total discharge from DML (Rignot et al., 2008). This is of the same order of magnitude as Shirase Glacier (13.8 ± 1.6 Gt yr^{-1}; Pattyn and Derauw, 2002) and Jutulstraumen (14.2 Gt yr^{-1}; Høydal, 1996), the other two major outlet glaciers in the DML region.

The stability of West Ragnhild Glacier is most likely governed by the dynamics of its ice shelf which is dominated by two important ice rises and several pinning points. While rapid changes at the marine boundary have not yet been observed, Rignot et al. (2013) point to an exceedance of basal melt (underneath the ice shelf and at the grounding line) over calving for several ice shelves in DML (including Roi Baudouin Ice Shelf, downstream of West Ragnhild Glacier). Melting at the grounding line 50 km west from West Ragnhild Glacier has been reported in Pattyn et al. (2012), but its magnitude is of the orders of tens of centimetres per year.

To understand what makes West Ragnhild Glacier one of the three most significant mass outputs in DML, we investigate its basal conditions using satellite remote sensing, airborne radar and ice sheet modelling. First, radar analysis reveals the geometry of the bed. Second, we characterize the roughness of the bed and its reflectivity through spectral and bed-returned power analyses, which inform us of the nature of the bed as well as of the water content. Finally, we estimate the basal friction through inverse modelling to reconstruct basal motion. We subsequently discuss the consequences of a marine-terminating East Antarctic outlet glacier, characterized by a wet sediment and dominated by basal motion/sliding.

3.2 Data acquisition

Ice flow surface velocities are generated based on RADARSAT data acquired during the austral spring of 2000. These velocities combine phase and speckle tracking offsets, using methods that minimize the error of the final combined product (Joughin, 2002). The resolution of the velocity data is $500\,m \times 500\,m$, covering the main trunk of West Ragnhild Glacier and its vicinity (Figure 3.1b).

The airborne radio echo sounding survey was carried out on West Ragnhild Glacier during the austral summer 2010–2011, resulting in one longitudinal (along-flow) profile and seven transverse profiles (Figure 3.1b). The radar system employed a 150 MHz centre frequency and transmitted bursts of 600 and 60 ns duration, toggling between the two bursts (Nixdorf et al., 1999, Steinhage et al., 2001). The system recorded at a rate of 20 Hz. For further signal-to-noise improvement, the data of same burst length were stacked ten-fold, resulting in a horizontal resolution of 80 ± 20 m. We identified the bed echo along 91 % of the entire survey (Figure 3.2). Most sections lacking a bed echo are shorter than $\sim$ 10 km (the maximum data gap is 20 km). Adjacent regions to these data gaps slope down steeply toward the data gaps. Therefore, the data gaps probably correspond to a deep bed and thick ice, causing an increased radar signal attenuation, and hence loss of signal.

Ice thickness was derived using a constant radio wave propagation speed of 168 m μs^{-1}. Surface elevation was obtained by laser altimetry from the aircraft, and bed elevation was subsequently derived by subtracting the ice thickness from the surface elevation. We applied the geoid height of 20 m above the EGM96 ellipsoid (Rapp, 1997) to derive the surface and bed elevations relative to sea level.

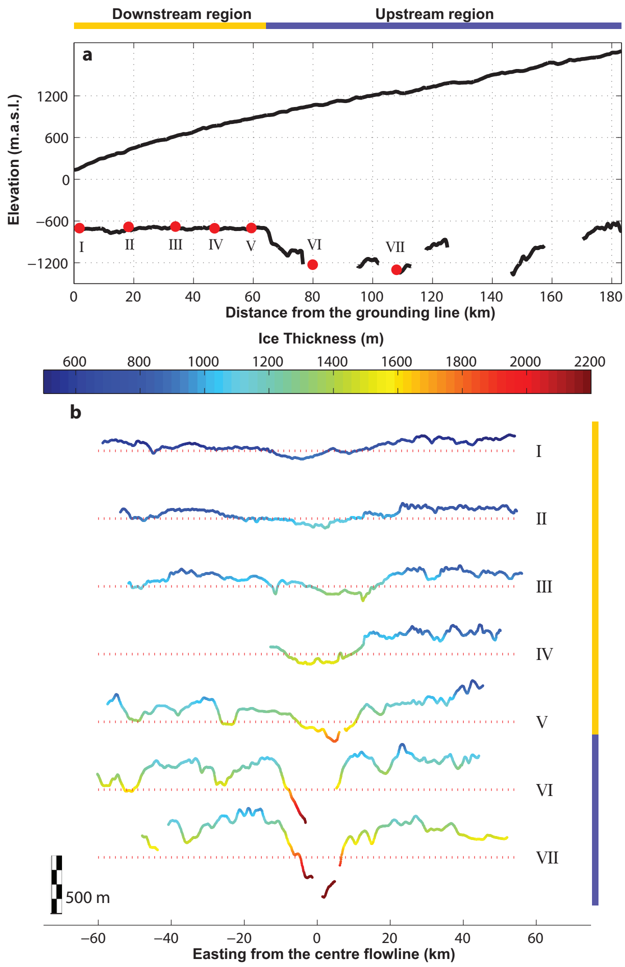

FIGURE 3.2: Radar data. **(a)** Ice and bed topography along the central flowline. The red circles are the locations of the cross profiles. **(b)** Bed topography (ordinate) and ice thickness (colour) measured across the flow. The red dotted lines show the isodepth of 600 m b.s.l., the approximate elevation of the flat basin measured along the centre flowline **(a)** and the reference for each profile.Transverse profiles are numbered from I to VII on both panels. The yellow and blue line illustrates our understanding of the downstream and upstream region.

3.3 Mapping the subglacial topography

Compared to older data sets of Antarctic bedrock topography (e.g. BEDMAP; Lythe et al., 2001), our new radar survey reveals a significantly different picture[1] (Figure 3.3). The survey highlights a marked contrast in bed topography (Figure 3.2). Between the Sør Rondane and Belgica Mountains, ice flows in a deeply incised valley, ∼ 20 km wide, lying ∼ 1000 m below sea level at the two uppermost transverse profiles (Figure 3.2b). The bed topography is rather variable here, fluctuating between 1200 and 800 m b.s.l. Further downstream, bedrock elevation increases rapidly (more than 500 m within 10 km distance) up to a flat subglacial lowland lying around 600 m b.s.l. This can be observed on both the longitudinal (Figure 3.2a) and cross profiles (Figure 3.2b). The elevation of this lowland varies less than 50 m locally, so the lowland is much flatter than the landward valley between Sør Rondane and Belgica Mountains. The amplitude of the local elevation variations increases sharply between cross profiles IV and V as we reach the

[1]The data collected for this paper are incorporated in the recently published BEDMAP2 data set (Fretwell et al., 2013). The difference between this radar-derived thicknesses and BEDMAP1 (Lythe et al., 2001) are presented in Appendix C.

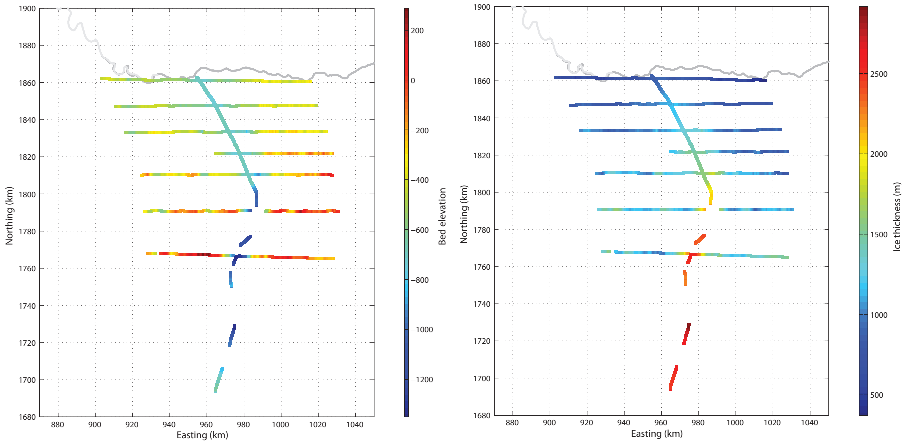

FIGURE 3.3: Bed elevation (a) and ice thickness (b) along the radar profiles, derived from the radar data. The grounding line is the same as in Figure 3.1b.

piedmont of the Sør Rondane Mountains. This is also the zone where we find the onset of the subglacial valley, described earlier.

3.4 Spectral analysis of bed topography

3.4.1 Bed roughness index

One way to quantitatively characterize the above-described bed conditions is to calculate bed roughness. The bed roughness index RI is obtained by applying a fast Fourier transform (FFT) to the bed elevation within a moving window (Taylor et al., 2004):

$$\mathrm{RI} = \int_{f_{\min}}^{f_{\max}} \frac{|X[f]|^2}{N_\mathrm{T}\Delta x}\,\mathrm{d}f\,, \tag{3.1}$$

where $f_{\min} = 1/(N_\mathrm{T}\,\Delta x)$, $f_{\max} = 1/(2\,\Delta x)$, $N_\mathrm{T} = 2^n$ is the number of data points in the window, Δx is the sampling interval (100 m in our case) and where

$$X[f] = \sum_{d=1}^{N_\mathrm{T}} x(d) e^{\frac{2\pi i}{N_\mathrm{T}}(d-1)(f-1)}\,. \tag{3.2}$$

Equation 3.2 is the definition of the FFT for a dataset $x(d)$ with index d in the range $1 \leq d \leq N_\mathrm{T}$, and $X[f]$ is the same data set in the frequency domain with index f in the range $f_{\min} \leq f \leq f_{\max}$. In other words, the bed roughness index RI is the integral of the resultant power spectrum within each of the moving windows[2].

We first resample the radar-derived bed topography (80 ± 20 m intervals) with a fixed (100 m) interval. We then detrend the measured bed elevation in each moving window, which is required

[2] See Appendix D for sensitivity evaluation of the spectral analysis.

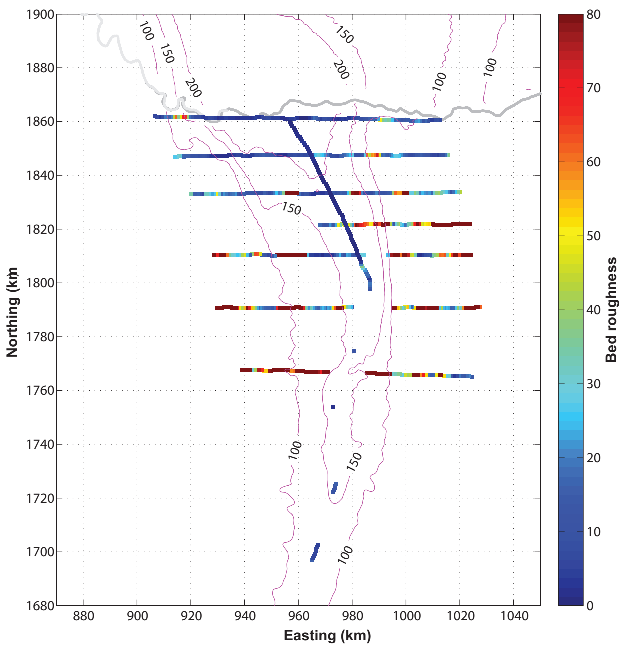

FIGURE 3.4: Bed roughness analysis. Bed roughness index of the basal topography (colour) calculated for wavelengths ranging from 200 to 6400 m. The grounding line is the same as in Figure 3.1b. Short legs of absent bed echoes result in long gaps in the estimated bed roughness indices due the window-based calculation of the bed roughness index. Larger RI corresponds to rougher bed. Contour lines represent surface speed (m a^{-1}).

to be able to perform an FFT. The method is applied within a 2^n data point window. Several authors recommend $n \geq 5$ (Bingham and Siegert, 2009, Rippin et al., 2011, Taylor et al., 2004). By using $n = 6$ we are able to analyse roughness over wavelengths ranging from 200 up to 6400 m.

3.4.2 Results

The longitudinal bed profile (Figure 3.2) reveals two distinct areas: a flat area (between the grounding line and 65 km upstream) and an intersected subglacial relief typical of subglacial mountain ranges. The transition between them occurs within 10 km. The bed roughness index RI is capable of quantifying this difference (Figures. D and 3.5a). While the two regions are still quite distinct, the transition of roughness from one to the other is more gradual than expected from visual interpretation. For the downstream cross profiles (I–III), the bed roughness is approximately constant, pointing to a wide and relatively smooth lowland. Following the analysis of Bingham and Siegert (2009), the flat and smooth area in the downstream section of the West Ragnhild Glacier may therefore very well be overlain by marine sediment. According to the further upstream profiles (IV–V), the bed is rougher away from the current glacier flowline (longitudinal radar profile). The low roughness area is therefore restricted to the zones of fast ice flow. Once outside this section, bed roughness indices increase, pointing to a rougher surface (VI–VII).

3.5 Analysis of bed-returned power

3.5.1 Analytical setup

To further examine the spatial distribution of basal conditions, we analyse the radar power returned from the bed [3], hereafter called BRP. The geometrically corrected BRP, $\mathrm{BRP^c}$, can be seen as a proxy for bed reflectivity if englacial effects do not vary along the radar profile (Matsuoka, 2011). The $\mathrm{BRP^c}$ is affected by both englacial attenuation L and bed reflectivity R. In the decibel scale, $[x]_{\mathrm{dB}} = 10\log_{10}(x)$, this relationship can be written as

$$\begin{aligned}[\mathrm{BRP^c}]_{\mathrm{dB}} &= [\mathrm{BRP}]_{\mathrm{dB}} + 10\log_{10}\left(h + \frac{H}{n}\right)^2 , \\ &\simeq [R]_{\mathrm{dB}} - [L]_{\mathrm{dB}} . \end{aligned} \tag{3.3}$$

The geometrically corrected bed-returned power $\mathrm{BRP^c}$ can be calculated based on the measured BRP returned from the bed and a geometric factor defined by $(h + H/n)^2$. Here, h is the height of the aircraft above the glacier surface, H is the ice thickness (distance between the surface and the bed of the ice mass), and n is the refraction index of the ice (~ 1.8; Matsuoka et al., 2012a). The $\mathrm{BRP^c}$ is then normalized to the mean of the observed values.

One has to note that effects of temporal changes in the instrumental characteristics and of ice crystal alignments are ignored in Equation 3.3. Englacial attenuation has contributions from pure ice and chemical constituents included in the glacier ice, both of which depend exponentially on ice temperature.

We estimate attenuation L using Equations. (3.4)–(3.6) listed below (Matsuoka et al., 2012a). The depth-averaged attenuation rate $\langle N \rangle$ is derived from the depth profile of the attenuation rate $N(z)$,

[3] we only analysed reflectivity within the along-flow profile. Because of calibration issue we cannot compare it to the cross-flow profiles.

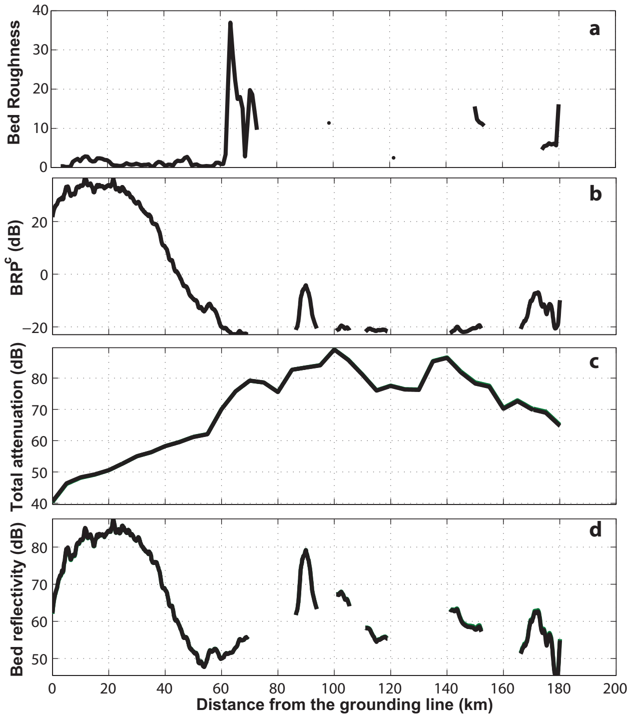

FIGURE 3.5: Subglacial conditions along the central flowline. **(a)** Bed roughness index RI; **(b)** geometrically corrected bed-returned power BRP^c; **(c)** englacial attenuation L; **(d)** bed reflectivity R.

i.e.,

$$[L]_{\mathrm{dB}} = \int_0^H N(z)\,\mathrm{d}z\,. \tag{3.4}$$

The attenuation profile $N(z)$ is proportional to local ice conductivity σ:

$$N(z) = \frac{1000(10\log_{10} e)}{c\,\varepsilon_0\sqrt{\varepsilon}}\sigma(z) \approx 0.914\,\sigma(z)\,, \tag{3.5}$$

where c is the wave velocity in vacuum, ε_0 is the permittivity of free space and ε is the relative permittivity of the ice. Since we focus only on the contribution of pure ice to the attenuation, conductivity depends only on temperature through an Arrhenius-type relationship.

$$\sigma = \sigma_0 \exp\left[-\frac{E_0}{k}\left(\frac{1}{T(z)} - \frac{1}{T_\mathrm{r}}\right)\right]\,, \tag{3.6}$$

where $\sigma_0 = 15.4\,\mu\mathrm{S\,m^{-1}}$ is the pure-ice conductivity at the reference temperature $T_\mathrm{r} = 251\,\mathrm{K}$, $T(z)$ is the vertical profile of temperature, $E_0 = 0.33\,\mathrm{eV}$ is the activation energy and $k = 8.617 \times 10^{-5}\,\mathrm{eV\,K^{-1}}$ is the Boltzmann constant (Matsuoka et al., 2012a).

Englacial temperatures $T(z)$ for the attenuation model (Equation 3.6) are calculated using a two-dimensional thermomechanical higher-order model (Pattyn, 2002, 2003). Details of this approach are given in Matsuoka et al. (2012a). We use a geothermal heat flux of $42\,\mathrm{mW\,m^{-2}}$ as lower boundary condition. However, as shown in Matsuoka et al. (2012a), the exact choice of geothermal heat flux will not affect the modelled englacial attenuation since the bed in the surveyed domain is predicted to be at the pressure melting point everywhere even with a flux as low as $42\,\mathrm{mW\,m^{-2}}$. Once the bed reaches pressure melting point, additional geothermal and shear heating have virtually no impact on ice temperature, hence on englacial attenuation (Matsuoka, 2011). Therefore, the estimated along-flow patterns of the attenuation and bed reflectivity are robust regardless of the uncertainties in geothermal heat flux. Figure 3.5c shows $[L]$ along the longitudinal profile.

Although the chemical contribution to attenuation can nearly equal the pure-ice contribution near the coast (Matsuoka et al., 2012a), the lack of observation forces us to ignore its contribution and to use only the pure-ice contribution to estimate englacial attenuation. Furthermore, MacGregor et al. (2007) and Matsuoka et al. (2012a) showed that the relative importance of impurities contribution decreases as temperature increases. The modelling reveals a mean attenuation rate from pure ice between 20.2 and 23.1 dB km^{-1}. For this range of value, Matsuoka et al. (2012a) determine that chemical contribution is less than the fifth of the pure ice contribution.

3.5.2 Results

In the upstream valley, BRP^c remains relatively low (-20 dB) and varies little (several dB) except at two sites where BRP^c shows anomalous features (90 km and 170 km upstream from the grounding line; Figure 3.5b). Further downstream, BRP^c increases by ~ 50 dB within 20 km, over which the ice thins only by ~ 200 m (Figure 3.2).

To clarify contributions of the bed reflectivity on BRP^c, we estimate the englacial attenuation using the predicted temperature (Figure 3.5c). Attenuation decreases ~ 20 dB within 10 km at 65 km upstream from the grounding line due to a decrease in ice thickness. Further downstream, attenuation gradually decreases by 20 dB over 50 km, which is probably more related to the changes in ice thickness than to changes in depth-averaged attenuation rate $\langle N \rangle$. To retrieve the actual bed reflectivity, we estimated bed reflectivity from BRP^c and englacial attenuation using Equation 3.3. The corresponding estimated bed reflectivity rapidly increases, approaching the grounding line at 40–50 km, from where it varies little within the last ~ 30 km (Figure 3.5d). The high bed reflectivity in the zone immediately upstream of the grounding line may eventually point to wet bed conditions. This high bed reflectivity is not directly related to the smoother bed interface because RI is calculated for the wavelengths longer than 200 m but the reflectivity is affected by the bed smoothness in the scale of several wavelengths of the radio wave (5 m for this study). In the next section, we will investigate whether wet basal conditions are likely or not.

3.6 Ice flow modelling

3.6.1 Model setup

Velocity data show that West Ragnhild Glacier accelerates steadily towards the grounding line (Figure 3.6). In this section,using an ice flow model, we will infer the required spatial distribution of basal friction (or, inversely, slipperiness) to match modelled ice flow velocities to the satellite-observed ones. The most common method is an inversion method in which a friction parameter is spatially optimized in order to minimize the misfit between modelled and observed velocities (Arthern and Gudmundsson, 2010, MacAyeal, 1992, 1993).

As a forward model we apply a simple ice flow model to calculate the ice flow field along the central flowline of Western Ragnhild Glacier, based on the shallow-ice approximation (SIA). In the vertically integrated case, the SIA surface velocity ($u(s)$) is then given by

$$u(s) = u(b) + \frac{2\overline{A}}{n+1} H |\tau_{\mathrm{d}}|^{n-1} \tau_{\mathrm{d}} \ , \tag{3.7}$$

where $\tau_\mathrm{d} = -\rho g H \frac{\partial s}{\partial x}$ is the driving stress, and $u(b) = \beta^{-2}\tau_\mathrm{d}$ is the basal velocity according to a viscous sliding law (Pattyn et al., 2008). Other parameters in Equation 3.7 are $\overline{A}$ and $n = 3$, the vertically integrated temperature-dependent flow parameter and the exponent in Glen's flow law, respectively; β is the basal friction, ρ is the ice density, g is the gravitational acceleration, H is the ice thickness, and s is the surface elevation. For a flowline stretching from the ice divide (Dome Fuji) to the grounding line, boundary conditions for Equation 3.7 are a zero upstream velocity and a fixed surface velocity at the edge of our profile of $u = 300\ \mathrm{m\,yr^{-1}}$, according to observations.

Since an SIA model does not take into account longitudinal stress gradients, spurious high-frequency variability in the velocity field is to be expected when the surface of the ice sheet is not supposed to relax to the imposed stress field. Especially small variations in surface slope may lead to a large variability in velocity, due to its dependence on the power of n. To prevent this, surface gradients are calculated over a distance of several ice thicknesses (Kamb and Echelmeyer, 1986, Rabus and Echelmeyer, 1997).

The main unknown in Equation 3.7 is the basal velocity field, which is initialized with a high value of basal friction ($\beta^2 = 10^7$), corresponding to conditions of ice frozen to the bed. We then invoke an optimization procedure to determine the spatial distribution of β^2 so that the modelled surface velocity (u_s^m) matches the observed one (u_s^o). This is formulated as a least-squares problem for which we seek β^2 that minimizes the following objective function:

$$J(\hat{\beta^2}) = \sum_{i=1}^{n_\mathrm{o}} \| u_\mathrm{s}^\mathrm{o}(i) - u_\mathrm{s}^\mathrm{m}(\hat{\beta^2}, i)\|^2 \ . \tag{3.8}$$

The minimization problem is solved in a vector-valued approach. The vector containing the squared errors of the basal velocity mismatch is provided to the algorithm that calculates the flow field according to Equation 3.7. The error vector is used to compute a preconditioned conjugate gradient (computed numerically using small variations in β^2 along the flowline). The subspace trust region method based on the interior-reflective Newton method (trust-region-reflective algorithm) described by Coleman and Li (1994, 1996) then determines the modified β^2-profile for the next iteration. The iterations stop when the change in $J(\hat{\beta^2})$ is below an arbitrarily small threshold.

We add two constraints to β^2. It has to be positive and, as we expect the basal friction pattern to be continuous in space (i.e. $u(b)$ is continuously differentiable), the spatial pattern is expressed in terms of summations of Legendre polynomials. Such polynomials have the interesting property that they form an orthogonal basis and lead to a better conditioning of the nonlinear optimization problem, thus necessitating fewer iterations to converge to the optimal solution. We use these polynomials to describe the spatial distribution of β^2 along the flowline. We use polynomials up to degree 35. At this stage, we reach convergence, which means that increasing the polynomial degree does not reduce the error function any further.

The surface and bed topography within the survey domain are taken from our data. Beyond this domain, bed and surface topography are taken from both BEDMAP (Lythe et al., 2001) and Bamber et al. (2009). The resulting profile is similar to the one resampled directly from BEDMAP2 (Fretwell et al., 2013), since our ice thickness data have been included. Short gaps within the retrieved bed echoes are linearly interpolated; the length of such gaps is typically less than several ice thicknesses, so that the large-scale flow fields are hardly affected by this choice. Longer gaps (> 10 km) were interpolated in the same way. Bed topography uncertainties associated with the longer data gaps introduces flow speed uncertainties in the most upstream area and are sufficiently far away from our region of interest.

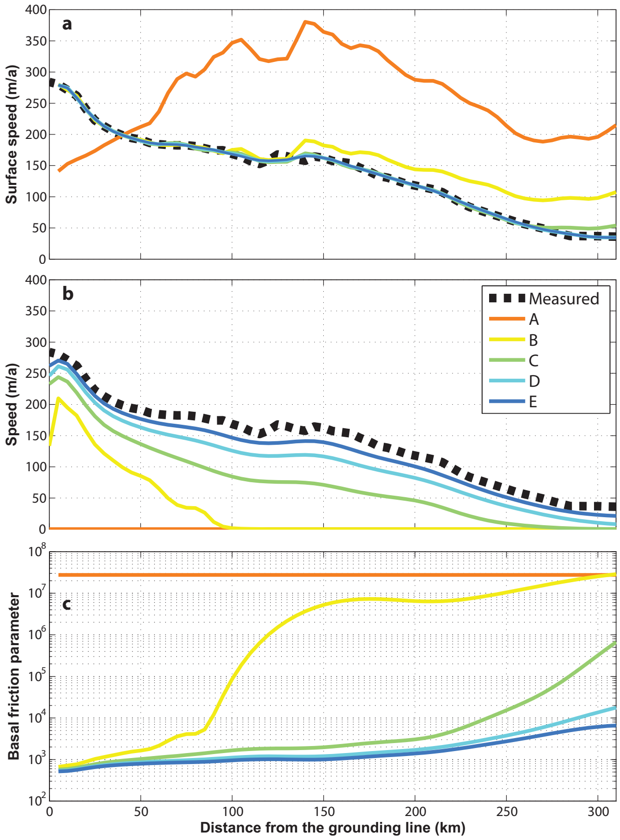

FIGURE 3.6: **(a)** Observed surface flow speed (dashed black line) and optimized surface flow speed profiles along the central flowline of West Ragnhild Glacier; **(b)** Basal ice flow speed according to the optimization and compared to the satellite-observed surface flow speed (as in panel **a**); **(c)** Basal friction β^2 along the flowline.

3.6.2 Results

To correct for the unknown deformational velocity, we performed the optimization procedure for different values of the vertically integrated flow parameter $\overline{A}$. Each of the values corresponds to mean ice temperatures of -2, -4, -5, -10 and $-15\,°$C (Cuffey and Paterson, 2010). Amongst the five different flow parameters depicted in Figure 3.6, case A corresponds to the warmest (softest) ice ($-2\,^{circ}$C), and predicts higher ice flow speeds due to ice deformation along the whole flowline compared to the observed ones. For this value, the optimization procedure fails, as the model cannot allow "negative" basal velocities. Not only is the ice too soft (hence flows too fast), the pattern of the deformational velocity does not match the observed velocity profile.

Cases B to E reveal a good match of the modelled velocities with the observed ones. For each decrement in ice temperature, the ice gets stiffer and the amount of basal sliding along the profile becomes more important. Therefore, cases D and E correspond to much colder (stiffer) ice (-10 and $-15\,°$C, respectively) and predict deformational velocities that are too small, so that basal sliding takes up the majority of the velocity along the profile.

The corresponding pattern of β^2 is, with the exception of case A, very similar for all simulations: it reveals a relatively high friction inland and a low friction in the area 100 km upstream from the grounding line. Over the upstream section of the longitudinal profile, ice motion is essentially governed by internal deformation. All experiments show that basal motion is dominant only in the downstream region.

3.7 Discussion and conclusions

Prior to our study, only two glaciers were considered as important contributors to the discharge of ice from DML, i.e. Jutulstraumen and Shirase Glacier, and both have been the subject of more interest in the past (e.g. Høydal, 1996, Pattyn and Derauw, 2002). Despite their fast flow (the grounding line velocity of Shirase Glacier is $> 2000\,\mathrm{m\,yr^{-1}}$), they each discharge approximately 10 % of the total snow accumulation of this part of the ice sheet (Rignot et al., 2008). Both glaciers are topographically constrained and characterized by a highly convergent flow regime. They also terminate in a relatively narrow trunk. From an ice-dynamical viewpoint, Shirase Glacier is a relatively stable feature, as its grounding line cannot retreat over a distance larger than 5 to 10 km, since the bedrock rapidly rises above sea level from the present position of the grounding line (Pattyn, 1996, 2000, Pattyn and Derauw, 2002). Such conditions make an outlet glacier less prone to dynamic grounding line retreat and significant mass loss due to dynamic changes in the ice shelf.

Taking into consideration West Ragnhild Glacier definitely changes the discharge picture in DML. Indeed, based on the thickness data across the grounding line in conjunction with satellite-observed ice flow velocities, its discharge (13–14 $\mathrm{Gt\,yr^{-1}}$) is comparable to the discharge of Jutulstraumen and Shirase Glacier. Nonetheless, the ice flow velocities of West Ragnhild Glacier are relatively low. Ice flow speed is $> 100\,\mathrm{m\,yr^{-1}}$ at 100 km upstream of the grounding line and up to $250\,\mathrm{m\,yr^{-1}}$ at the grounding line (Figure 3.1). The reason for such low values is ice shelf buttressing by two major ice rises within the Roi Baudouin Ice Shelf, slowing down the flow upstream.

Despite present-day stable conditions, the analysis presented in this paper clearly demonstrates that West Ragnhild Glacier (i) is an important outlet glacier, (ii) is marine terminating with a grounding line 600–700 m b.s.l., and (iii) has a downstream section that is smooth, sediment covered and water saturated in the downstream area. Beside data evidence, inverse modelling allows the conclusion that decreasing basal friction leads to an increasing basal velocity towards the grounding line. Using two different kinds of evidence, we demonstrate that the bed/ice interface plays a dominant role in the acceleration of West Ragnhild Glacier toward the grounding line.

Given the fact that the smooth bed is also flat and horizontal and devoid of distinct lateral constraints, the grounding line is potentially capable of advancing and retreating across a substantial area. According to theoretical considerations (Schoof, 2007), a grounding line retreat may be expected if sudden changes occur at the seaward side. The close proximity of the DML ice shelves to the margin of the continental shelf (Timmermann et al., 2010, and Figure 3.1a) could potentially allow relatively warm water from the abyssal plains to circulate under the shelf, leading to significant sub-shelf melting (e.g. Smedsrud et al., 2006). Unpinning of the ice shelf could therefore lead to grounding line retreat due to increased flow speed, hence increased dynamic mass loss, in line with recent observations (Rignot et al., 2013). New geophysical data presented in this paper highlight such a possibility in West Ragnhild Glacier.

Chapter 4

Surface mass balance anomaly across an ice rise derived from internal reflection horizons through inverse modelling.

in prep. by D. Callens, E.Witrant, R. Drews, M. Philippe and F. Pattyn.

Ice rises are quite common, locally grounded parts of Antarctic ice shelves which play an important role in regulating the flow of ice shelves. Since they protrude out of the ice shelf, they induce an orographic uplift of the atmospheric flow and therefore influence the pattern of the surface mass balance (SMB) across them, resulting in an asymmetric SMB distribution. In this paper we present an original and robust method to quantify this distribution. Combining shallow and deep radar layers, the SMB across Derwael Ice Rise is reconstructed. Two methods are employed as a function of the depth of the layers: i.e., the shallow layer approximation for the surface radar layers and an optimization technique based on an ice flow model for the deeper ones. Both methods produces similar results. We identify a difference in SMB magnitude of 2.5 between the flanks and the ice rise divide, as well as a shift of ≈4 km between the SMB maximum and the crest. Across the ice rise, SMB exhibits a very large variability, ranging from 0.3 to 0.9 m w.e. a^{-1}. This anomaly is robust in space and time.

4.1 Introduction

Ice rises are common features of the coastal ice-shelf belt of the Antarctica. They are locally grounded and their surface protrudes out of the surrounding ice shelf. Not much is known about their origin and formation, but they do play a crucial role in stabilizing the flow of ice shelves by exerting a back-pressure, also known as the buttressing effect. Moreover, most ice rises of the coastal Dronning Maud Land are sufficient large features, so that exhibit a local ice flow pattern, and the ice shelf flows around each of these protruding bumps. In that sense, they behave as miniature ice caps (Martin and Sanderson, 1980).

Since ice rises present a parabolic-shaped anomaly within the flat surrounding ice shelf, they also impact the atmospheric flow. Regional atmospheric and mass balance modelling (Lenaerts et al., 2014) has demonstrated that the related orographic uplift induces an increase in precipitation on the wind side and a deficit on the lee side. The down-slope on the lee side is characterized by erosion due to wind acceleration (Lenaerts et al., 2014). Both processes compete to produce an asymmetric pattern of the surface mass balance (SMB).

In order to investigate whether this pattern is robust in space and time, we employ two types of ice-penetrating radar data. Radar is often used to define the spatial variation of SMB, both for characterizing the large-scale (e.g. Nereson et al., 2000) or small-scale (King et al., 2004) variations in SMB across ice divides. Radar profiling is capable of spatially extrapolating accumulation measurements extracted from firn cores (e.g. Eisen et al., 2008). The underlying principle assumes that laterally continuous internal reflection horizons (IRH) in the radar data are isochronous, i.e., each continuous horizon has a constant age all along the profile. For layers shallower than a few percent of the ice thickness, one can assume that they have not yet been deformed significantly by ice dynamics (Waddington et al., 2007). For deeper layers, on the contrary, it is essential to consider ice dynamical effects, which influence the deformational pattern of each layer (Waddington et al., 2007).

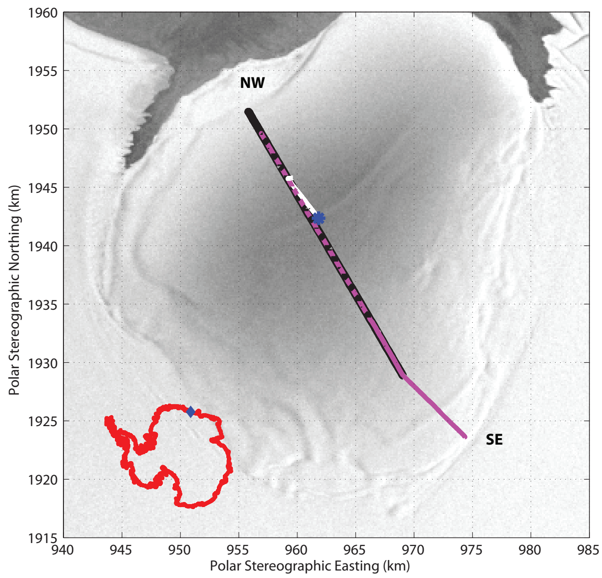

FIGURE 4.1: Map of the Derwael Ice Rise. The thick black line is the low frequency profile. The dashed and solid purple lines are the high frequency profiles of 2012 and 2013, respectively. The white line is the link to the borehole (blue star). The core site is located on the divide. RADARSAT is used as a background image. The inset in the bottom left corner informs on the location of DIR in Antarctica. NW and SE refer to north-west and south east ends of the profile. These are mentioned on each figure of this chapter.

Our study area is the Derwael Ice Rise (DIR), situated in the Roi Baudouin ice shelf, one of the fringing ice shelves of eastern Dronning Maud Land, East Antarctica. The ice rise is quasi-circular in shape and characterized by a distinct ridge in its center, oriented in SW-NE direction and culminating 350 m above the surrounding ice shelf (Figures 4.1 and 4.2). Between 2010 and 2013 we carried out several radar surveys across DIR to investigate, amongst others, the Raymond effect operating underneath the ridge (Drews et al., 2014). Here, we focus on the retrieval of surface accumulation in space and time, from both surface and deeper radar-detected layers, and investigate whether the anomalous pattern reproduced by regional SMB modelling (Lenaerts et al., 2014) is (i) clearly observable in the radar data, and (ii) whether this pattern is a robust feature in space and in time.

4.2 Methodology

We collected ice-penetrating radar profiles across DIR using two systems: a (higher-frequency, HF) 400 MHz radar (GSSI:SIR 3000) and a (lower-frequency, LF) 2 MHz radar system with resistivity loaded dipole antennas (Matsuoka et al., 2012b). The former images the shallow layering up to 50 m depth, while the latter is designed to detect deeper layers as well as the bed. Internal reflection horizons (IRHs) correspond to horizontally coherent contrasts of the dielectric properties, which are linked to changes in ice density, acidity and crystal orientation fabric (Fujita et al., 1999). It is generally accepted that many (if not all) IRHs are former surfaces, which have migrated to larger depths since their deposition. At shallow depths, the vertical spacing between these paleo surfaces is mainly a function of the SMB. At larger depths, the surfaces become increasingly deformed by ice flow. We aim to reconstruct the SMB history using the IRH geometry of both shallow and deep layers. For layers detected with the HF radar we apply the shallow layer approximation (Waddington et al., 2007), for layers detected with the LF radar we use an inverse modelling approach which accounts for ice deformation.

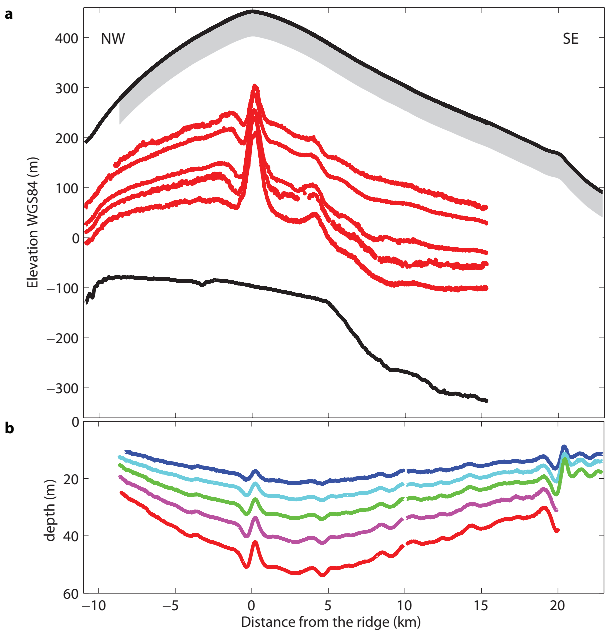

FIGURE 4.2: (a) Geometry of the DIR. Bed and surface are in black and layers detected with low frequency radar are in red. The grey zone is the detection range of the high frequency radar. (b) Depth of the shallow layers. They are located in the grey zone of panel (a). The small data gap situated around +10 km is the junction between data from 2012 and 2013.

4.2.1 SMB reconstruction using the shallow layer approximation

Figure 4.1 displays the 32 km long HF profile which is aligned perpendicular to the ridge. The acquisition of this profile was split into two field campaign in austral summer 2012 and 2013. The sampling rate is 10 Hz and the antenna is towed at $\approx 3\ \mathrm{m\,s^{-1}}$. The range of the record is 600 ns split into 2048 samples, resulting in a vertical resolution of ≈ 6 cm. From the produced radargrams, we identified five continuous IRHs (Figure 4.2b).

The profile was geolocated with kinematic GNSS surveys: A dual phase Trimble receiver was attached to the radar during the profiling and recorded the position at one second intervals, simultaneously with a non-moving base station at the dome. The kinematic data were post-processed differentially relative to the position of the base station where the coordinates were fixed using precise point positioning techniques.

The HF IRHs are linked to a nearby firn core drilled in 2012 (Hubbard et al., 2013). This 100 m long core provides the vertical profiles of temperature, density and age. The density has been measured for 48 samples distributed at different locations along the core. The agedepth scale is based on the seasonal variability of δ^{18}O stable isotopes. Since the HF profile is located $\approx$400 m from the firn core, an extra HF profile was collected to link both sites within 6–7 m of the firn core site (white line in Figure 4.1). This enables a direct dating of the corresponding shallow layers.

To link the core with the HF profile, the two way travel time has to be converted into depth via the propagation speed, which is a function of the density. Therefore, the depth of all IRHs was determined using the electromagnetic wave speed in firn given by the mixing formula of Looyenga (1965). The continuous density–depth scale needed for the velocity-depth profile stems from a semi-empirical model of firn compaction (eq. 4.1, Arthern et al., 2010) which was tuned to fit the discretely measured samples of the core, i.e.,

$$\frac{\mathrm{d}\rho}{\mathrm{d}t} = \begin{cases} c_0(\rho_i - \rho), & \rho \leq 550\,\mathrm{kg\ m^{-3}} \\ c_1(\rho_i - \rho), & \rho > 550\,\mathrm{kg\ m^{-3}} \end{cases} \tag{4.1}$$

where $\rho_i = 917$ kg m^{-3} is the density of solid ice and ρ is the local density, and c_0, and c_1 are rate parameters whose values are defined using the Nabarro-Herring relation (Arthern et al., 2010):

$$\begin{cases} c_0 = \alpha\, a\, g\, exp\left(-\frac{E_c}{RT(z)} + \frac{E_g}{RT_{av}}\right) \\ c_1 = \beta\, a\, g\, exp\left(-\frac{E_c}{RT(z)} + \frac{E_g}{RT_{av}}\right) \end{cases} \tag{4.2}$$

a is the SMB (0.55 m w.e. a^{-1}), g is the gravitational acceleration, $R = 8.314$ J mol^{-1} K^{-1} is the gas constant, $E_c = 60\,\mathrm{kJ\,mol^{-1}}$ is the activation energy for self-diffusion of water molecules through the ice lattice, $E_g = 42.2$ kJ mol^{-1} is the activation energy for grain growth and T_{av} =-14°C is the mean annual temperature based on the temperature at 10 m depth in the core. $T(z)$ is the temperature at depth z based on temperature profile of the core. Equations 4.1 and 4.2 express the evolution of density with time. As we are interested in the evolution with depth (z), we have to decompose the equation 4.1 into :

$$\frac{\mathrm{d}\rho}{\mathrm{d}t} = \frac{\partial\rho}{\partial t} + v\frac{\partial\rho}{\partial z}\,. \tag{4.3}$$

Assuming steady state conditions($\partial\rho/\partial t = 0$), the surface subsidence rate (v) equals the surface snow accumulation (taken as 1.375 m a^{-1} snow equivalent, based on the thickness of the upper layers of the firn core drilled at DIR), which is also known as Sorge's law (Bader, 1960, 1962). The density model is tuned to minimize the difference with the 48 density samples of the core through adjustment of the parameter α and β. These parameters have been estimated to be 0.02 and 0.015, respectively. This model ($\partial\rho/\partial z$) is integrated from surface density (400 kg m^{-3}) to the density of the ice (917 kg m^{-3}).

To estimate the SMB corresponding to each layer, we divided the total amount of ice between two layers by their difference in age. For the first layer, we consider the surface as a layer of age equals 0.

The absolute values derived here are inflicted with uncertainties, such as the error on the dating and on the density-depth model, which impacts the depth determination of the IRH and the determination of the cumulative mass above the IRH. The uncertainty on the layer age is estimated to be ± 1 year (based on the layer counting method). The error on the density is defined as the root mean square difference between the density-depth model and the 48 density samples of the firn core. The combined error on the derived SMB values is then calculated using standard error propagation.

4.2.2 SMB reconstruction using inverse modelling

4.2.2.1 Data

The same profile as discussed in the previous paragraphs was previously occupied with the LF system in austral summer 2010. (Figure 4.1). This radar profile shows both reflections from the bed and englacial reflectors. We picked five continuous IRHs in the LF radar data (Figure 4.2a). The positioning of this survey was obtained using a Leica L1 receiver which was processed using the kinematic precise point positioning from the Canadian Geodetic Survey.

Errors in the depth determination of the IRHs stem from (1) the uncertainty of the pure ice velocity, (2) uncertainties in the bulk firn correction, (3) from the oblique raypaths between transmitter and receiver, and (4) from an internal variability in picking the maximum amplitude of the IRH. We estimate the combined error on the depth uncertainty to be around $\pm$ 10 m.

We derived the depths of LF IRHs from the two-way travel-time using a uniform propagation speed (168 m μs^{-1}) and add a bulk firn correction of 8.8 m based on the density profile described in the previous section. The layer depth is known by $\pm$ 10 metres. This uncertainty stems from several factors : (i) the uncertainty of the pure ice velocity, (ii) uncertainties in the bulk firn correction, (iii) from the oblique raypaths between transmitter and receiver, and (iv) from an internal variability in picking the maximum amplitude of the IRH. Each of these errors are difficult to estimate but by using 10 m we consider that we obtain reasonably robust results.

As the deep layer geometry is imprinted by the internal deformation of ice, this influence has to be accounted for prior to extracting the SMB signal. We decided to reconstruct surface mass balance distribution by inverse modelling. The inverse model is separate in two components: the forward model which describes the dynamics of the ice and the optimization scheme which ensure a fast convergence toward the most likely SMB pattern according to the data.

4.2.2.2 Forward model

The IRHs of in the LF data warp upwards beneath the ice divide. This pattern originates from the non-linear ice rheology, which stiffens ice under the low deviatoric stresses encountered beneath ice divide (a.k.a the Raymond effect, Raymond, 1983). This process affects specifically the section between -2 and +3 km in the LF data (Figure 4.2a). Furthermore, we suspect that a section further to the south-east (between +3 and +5 km), where a second (smaller) bump exists, is also related to the Raymond effect and attributed to a previous position of the ice divide (Drews et al., 2014). For the upward arching to develop, the ice divide position needs to remain horizontally stable for a certain amount of time, and from the amplitude of the arches one can deduce how long the local flow pattern of the ice rise has prevailed (Drews et al., 2014).

Simulating the Raymond effect underneath the ice divide requires a thermomechanical full-Stokes model. However, as shown in Drews et al. (2014) and Martìn et al. (2009), the amplitude of the bump is very difficult to reproduce and not only requires the incorporation of anisotropic rheology, but also surface thinning. Given these complicated factors, the presence of a side bump that cannot be taken into account and the computation time associated with full Stokes models, the central part of the IRHs is ignored and the analysis is performed on the flanks of the ice rise domain.

Given the flank flow regime, the forward model is set with the Shallow-Ice approximation (SIA). Since Drews et al. (2014) established that basal ice temperature is negative ($\approx -5°$C), we assume that the ice is frozen to the bed and basal melting can be neglected. We assume plain strain so we model velocities along the flow line. Finally the ice sheet geometry is prescribed with current one and we assume steady state.

Both the ice flow field in flank-flow regime and the age field are solved using an Eulerian approach (Rybak and Huybrechts, 2003). For convenience, we redefine the depth scale as $\zeta = (b + H - z)/H$ where z is the elevation above the bedrock, b is the bed elevation and H is the ice thickness. At the surface, $\zeta = 0$, while the bottom of the ice mass becomes $\zeta = 1$. Following Pattyn (2010), the horizontal flow field is given as a shape function based on the balance flux. In the scaled coordinate system, the horizontal velocity u becomes:

$$u(x,\zeta) = \frac{n+2}{n+1}\,\overline{u}(a(x))\,(1-\zeta^{n+1})\ , \tag{4.4}$$

where x is the horizontal coordinate, $\overline{u}$ is the balance velocity, $n = 3$ is the Glen index and a is the surface mass balance. The vertical velocity w is derived from the horizontal flow field using the incompressibility hypothesis. We use an analytical solution following Hindmarsh (1999):

$$\begin{aligned} w(x,\zeta) &= -\left[\frac{\zeta^{n+2} - 1 + (n+2)(1-\zeta)}{n+1}\right] a(x) \\ &\quad +(1-\zeta)\,u(x,\zeta)\nabla H + u(x,\zeta)\nabla b\ . \end{aligned} \tag{4.5}$$

One should note that each of the velocity components are a function of the SMB ($a(x)$).

SIA-based models are fast and appropriate for flank dynamics. However, they cannot resolve the Raymond effect. Since it seriously obliterates the signal that may eventually be stemming from the local accumulation rate, the section between -2 and +3 km has to be take out in our analysis described below. Similarly, we deliberately take out as well the section the section of the former Raymond bump (between +3 and +5 km).

4.2.2.3 Optimization

In the inverse procedure, we determine the SMB distribution which minimizes the difference between the depths of the observed (Figure 4.2a) and modelled isochrones. This problem is underconstrained as neither the SMB of the last millennium nor the age of the observed layers are known. To make an assumption on the age of these layers, we applied a Nye time scale (Haefeli, 1963) with a mean SMB (0.55 m w.e a^{-1}) to the mean depth of the layer in the region of interest. The mean layers depths range from 180 to 341 m and the according ages range from 432 to 1030 years before 2012. This dating procedure may seem unusual. This method was chosen due to the presence of the Raymond bump which prevents the use of Nye time scale under the divide (Raymond, 1983) and even up-to-date full stokes models still struggle to accurately represent the magnitude of the Raymond effect on DIR. Raymond effect is particularly strong and its modelling requires full stokes equations but also anisotropy and thinning to match observation (Drews et al., 2014).

The SMB is initialised with a constant value $a(x) = 0.55$ m w.e a^{-1} for all x. We then invoke an optimization procedure to determine the spatial distribution of $a(x)$ so that the modelled IRH (z_j^m) matches the observed one (z_j^o). z_j is the depth of IRH j and m and o denote modelled and observed quantities respectively. We assume that the SMB distribution does not vary between the formation of the younger and the formation of the older LF isochrones. We aim to minimize the mismatch of all modelled layers with all observed ones to reconstruct an unique solution for $a(x)$. As we work for a global solution (i.e. time-averaged distribution of a), all layers are involved to get a unique solution. This is formulated as a least-squares problem for which we seek $a(x)$ that minimizes the following objective function :

$$J(a) = \sum_{j=1}^{n_{irh}} \frac{1}{\sigma_j^o} \sum_{i=1}^{n_j^o} \omega(i) \, \| z_j^o(i) - z_j^m(a,i) \|^2 + \kappa^2 \frac{d^2(a)}{dx^2} \;, \tag{4.6}$$

where n_{irh} is the number of IRH's involved, n_j^o is the number of data points of layer j, $\omega(i)$ is a mask set to one everywhere except under the divide (-2 km to +5 km, where Raymond effect is most pronounced) where $\omega(i) = 0$. Since the variability of the isochrones increases with depth, we normalised the mismatch by the variance of the observed IRH (σ_j^o). We aimed to ensure the same weight for each layer.

Given an SMB distribution ($a(x)$), the algorithm calculates the flow field and age field (according to equations (4.4) and (4.5)) to provide a modelled isochrone. The minimization problem is solved with a vector-valued approach. The vector contained the squared errors of the isochrones mismatch. This vector is composed of the two terms of equation 4.6. The first vector components are the term of the summation and the last components are the regularisation term.

The error vector is used to compute a preconditioned conjugate gradient (computed numerically using small variations in a along the flowline). The subspace trust-region method based on the interior-reflective Newton method (trust-region-reflective algorithm) described by Coleman and Li (1994, 1996) then determines the modified a-profile for the next iteration. The iterations stop when the improvement in $J(a)$ is below an arbitrarily small threshold.

As we expect the SMB pattern to be continuous in space (i.e. $a(x)$ is continuously differentiable), the spatial pattern of $a(x)$ is expressed in terms of summations of Legendre polynomials. Such polynomials have the interesting property that they form an orthogonal basis and lead to a better conditioning of the optimization problem, thus necessitating less iterations to converge to the optimal solution.

To avoid wiggling and overfitting, we add a roughness term which tunes the smoothness of the SMB distribution based on its second order spatial derivative (second term of eq. 4.6). The optimisation procedure thus minimises this term as well. We applied a roughness factor, κ, to ensure that this term has roughly the same variance as the first term of the cost function (equation 4.6). In the reference run, we applied a $\kappa = 3.10^4$. An higher κ will more linearise the resulting profile of surface mass balance.

To evaluate the impact of the error on depth on the inversion procedure, we applied the inverse modelling to the extreme possible depths of the IRHs (± 10 m), resulting in two new distribution of SMB that provide the confidence interval.

4.3 Results

4.3.1 Shallow internal reflection horizons

In the HF data (Figure 4.2b), one may notice that the deepest part of each of the internal layers is not situated underneath the ice divide, but near km 4. One may also notice that toward the south-east, layers are generally lying deeper than at the north-western side of the profile.

SMB across DIR is extremely variable. From wind side (South-East) to lee side (NW), SMB rises up to a maximum 4 km before the divide and then decreases continuously on the other side to reach the same SMB than on the other flank (Figure 4.3). The maximum is approximately 2.5 times the SMB on the flanks. This scheme is consistent for all the layers. The magnitude of all the layers is similar except for the second layer which is everywhere higher than the others. This can be due to the temporal variability of SMB or a misestimation of the age at the core. The four other horizons vary from low values (≈ 0.35 m w.e. a^{-1}) on both flanks to a maximum of ≈ 0.75 m w.e. a^{-1} around 4 km south-east of the divide. According to the dating of the core, the ages of these layers are: 17a, 21a, 27a, 35a and 46a.

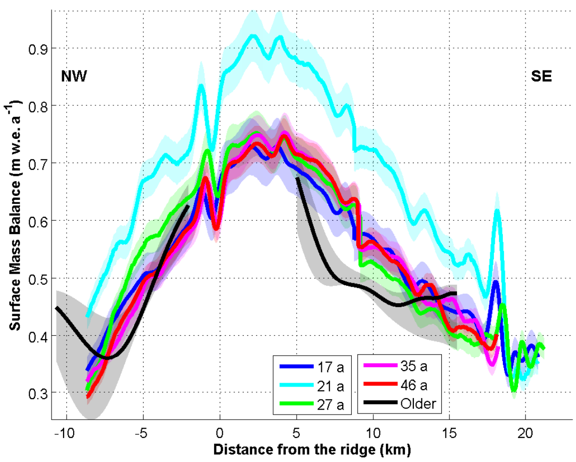

FIGURE 4.3: Spatial distribution of the SMB across the DIR inferred from shallow and deep layers. The color code for the shallow layers is the same as in Figure 4.2. The shaded areas denote the confidence intervals (with respect to the error on the accumulation). The solid black line is the result of the optimisation on deep layers. The grey shaded area represents the range of SMB derived while taking into account the depth uncertainty.

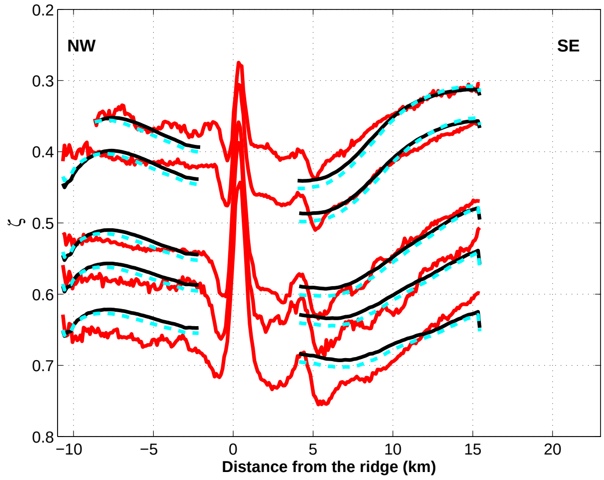

FIGURE 4.4: Comparison between modelled and observed (red) IRHs with a varying dataset. Black IRHs are the results of the reference run while light blue ones are obtained by the reconstruction of SMB based on the four other layers.

Superimposed on this broad-scale gradient are small scale features. Two regions are interesting : (i) around the divide and (ii) around the km 20 on the south-east side (Figure 4.3). Within 1 km around the divide, there are a local minimum and a local maximum. This is an artefact of the method which does not take in account the deformation of the firn and the underlying ice and is taken as a footprint of the Raymond Bump observed lower. The second anomaly corresponds to a slope break in the surface topography (Figure 4.2). This small change of slope affects the wind speed and consequently the wind redistribution of snow (King et al., 2004).

Error on SMB depends on the error on the depth-age scale which is $\pm$ 1 year and the root mean square error of the density-depth model: ± 18.2 kg m^{-3}, which results in an additional uncertainty on the depth estimation that varies with depth. The combined effect of these errors on the SMB ranges between ± 0.013 and $\pm$ 0.05 m w.e a^{-1} and are displayed on Figure 4.3. The error on the shallowest layer is larger due to the error on the age, which dominates the error calculation and is relatively more important for young layers. Except IRH21a, all the layers are within the error bars of the others.

4.3.2 Deep internal reflection horizons

The results of the inverse method are shown on Figure 4.3. The amplitude of the SMB distribution is consistent with the results inferred from shallow layers with approximately the same spatial distribution. However, we draw attention to the fact that only the relative variation can be considered since absolute values depend on the parametrisation of the depth-age scale. Nevertheless, comparison with results from shallow layers show a good agreement between the methods. The gradients on the lee-side (NW) are very similar while the agreement is less good on the wind side. The gradient is more constant on this side for the results from HF radar.

Figure 4.4 shows the fitting between the observed and modelled layers. The model performs quite well to describe the upper layer and its accuracy slightly decreases with depth. Nonetheless the global fitting adequately captures the major trends, even in the deeper layers. Even if an offset due to the uncertainties on the age is possible, the SMB distribution derived with this method is reliable.

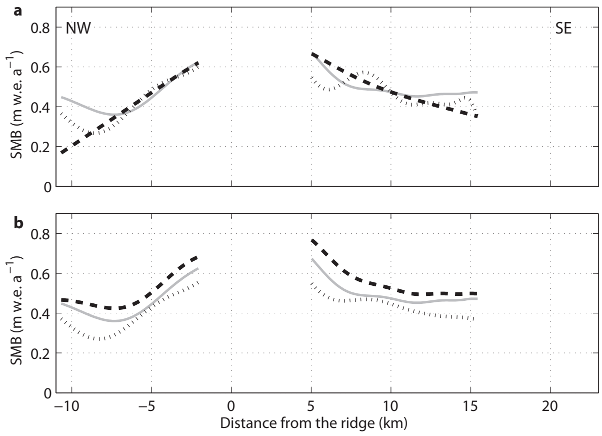

FIGURE 4.5: Sensitivity analysis of parameter (a) κ and (b) age-depth relationship. In both panels, the thin grey line is the reference run. In panel (a), the dotted line is the model with a κ divided by 10 and the dashed line has a κ multiplied by 10. In panel (b), the dotted line refers to an "older" scenario while the dashed line corresponds to a younger one.

4.4 Discussion

4.4.1 Sensitivity analysis of the model

To test the robustness of the model, we run 3 experiments and compare the results with the nominal SMB profile presented above. The first experiment is to vary the roughness coefficient (eq. 4.6), κ, within one order of magnitude in both directions. This allows us to show the impact of this parameter on the results (Figure 4.5a). Unsurprisingly, a lower κ results in an higher frequency content. However using an higher κ seems to improve the boundary discrepancy observed on the NW side. Table 4.1 shows the normalized cost function for the different sensitivity tests. A lower κ improves the matching because a larger part of the uncertainty due to the forward model is transferred to the SMB distribution (resulting in an overfitting of the data). Nevertheless, the roughness term does not change the bulk gradient of the SMB. In this respect, the method can be considered as robust.

TABLE 4.1: Value of the cost function divided by the number of layers involved in the inversion and normalized by the value of the $J(a)$ of the reference run.

Model run	**Normalized $J(a)$**
Reference run	1
$\kappa/10$	0.55
$\kappa \times 10$	1.55
age–depth scale +10%	0.69
age–depth scale −10%	1.29
without deep IRH 1 (top)	0.72
without deep IRH 2	0.89
without deep IRH 3	1.07
without deep IRH 4	0.98
without deep IRH 5 (bottom)	0.80

The second experiment evaluates the influence of the depth-age relationship. The IRHs were dated by applying a Nye time scale relationship to the mean layer depth calibrated with an SMB equals to 0.55 m w.e a^{-1}. Since this method may induce significant errors, we investigate the impact of an arbitrary variation of 10% on the depth-age scale. As expected, this produces an overall shift in the SMB amplitude (Figure 4.5b). The analysis of the cost functions favour an older relationship between depth and age. Again the SMB profiles are very similar and the result of the reference run stays within the bounds of the two extreme scenarios.

With the last experiment, we test the dependency of the model on the dataset. The optimisation is run five times, each time discarding a different layer used in the inversion procedure. Each run gives an SMB distribution, which we use to reconstruct the removed layer. On Figure 4.4, each modelled layer is obtained by a forward run with the SMB distribution inferred from the optimisation on the other layers. The results are very similar to the reference run and demonstrate the quality of the inversion. Furthermore, the cost function values for the best match show that each run gives approximately the same results illustrating the global coherence of the method to handle multiple IRHs

While the inversion works satisfactory, the forward model may be hampered by different simplifying assumptions. First of all, the steady state assumption is questionable. Drews et al. (2014) propose that the main Raymond arch beneath today's divide is a result of a sustained thinning, however, during that process the ice divide remained laterally stable. Since Lenaerts et al. (2014) show that the asymetric SMB distribution is mainly a function of the divide position, we argue that the steady-state assumption which was imposed here does not significantly alter the inferred SMB distribution (but may affect its magnitude).

The second caution concerns the plain strain assumption. Indeed, the ridge is slightly curved to the south-east. Consequently, divergence occurs on this side and convergence on the other side. Divergence pushes the layers down and affects positively the SMB reconstruction. However Reeh (1989) shows that the influence of the divergence is limited for the first 90% of the ice sheet depth and we hence decided to neglect it. Furthermore, the SMB described with the shallow layers shows the same distribution as the deep layers. This reinforces our confidence in the method used.

In this paper, we essentially focus on the gradient of SMB because there are significant uncertainties on its absolute value, at least for the deep layers. In the range of the error bar, we are confident on the values retrieved from shallow layers, except for IRH 21a which is suspiciously inconsistent with the others. Considering deep layers, the absolute value is uncertain. As shown by the second experiment, a variation of the age-depth relationship affects the mean value of the SMB without affecting its pattern. It is why we are confident on the gradient. Furthermore, it matches the results of atmospheric modelling. Lenaerts et al. (2014) showed with RACMO that SMB across an ice divide rise and drop along the trajectory of the wind with a maximum a bit upstream of the ice divide.

4.5 Conclusion

Combining geophysics data and modelling, we were able to reconstruct SMB distribution. The shallowest layers are considered not affected by ice dynamics and their geometry directly reflect the pattern of accumulation. Therefore, we were able to draw a fine distribution of recent SMB. For deep isochrones, we presented an original and robust method which allows exploring the SMB of the past : we used an inverse model to define the most likely distribution of SMB according to the geometry of these isochrones. This method has the advantage to be flexible. It can be applied to other places, such as other ice rises. It is also possible to change the forward model. Indeed, the optimisation procedure permits to flexibly adapt the forward model to take into account more complex representation of ice flow including, for instance, Raymond effect, basal melting or evolving geometry.

With an inversion procedure, we derived the SMB pattern across the Derwael Ice Rise and showed that this pattern is long lasting. The asymmetric distribution is related to orographic uplift of air masses. It induces an increase of precipitation on the wind side and a deficit on the lee side. As we roughly estimate the age of the oldest IRH to be more than 1 ka and as no significant differences between results from shallow and deep layers could be observed, we conclude that the SMB pattern across the Derwael Ice Rise do not significantly change over the last millennium and that atmospheric circulation did not change neither. This conclusion is consistent with the large Raymond bump observed on DIR. Indeed, this feature had to develop within stable conditions.

Chapter 5

Comprehensive description of the coastal Dronning Maud Land

This chapter brings me the opportunity to merge all my contributions, major and minor, in a global overview of Sør Rondane Mountains(SRM) sector from different point of views. Generally, information presented in this chapter are published or under review in peer-review journals. However some ideas presented may be speculative and are meant to give new insights in the dynamical characteristics of the region.

5.1 Mass balance of the Sør Rondane Mountains Glacial System

Based on a new airborne radar survey of the SRM glacial system, grounding line ice thickness could be accurately mapped across the major outlet glaciers. We calculated the mass output of the four drainage basins which constitute this system (Chapter 2). In the framework of an input–output study, this output is compared with the area–integrated SMB over these basins (the input) from three different datasets. The mass balance assessment obtained are subsequently evaluated.

The output at the grounding line is driven by a flow regime dominated by the basal motion (Table 2.2 and Chapter 3). The plug flow is therefore valid and uncertainty on ice dynamics is low. However the temporal evolution of the velocity could be interesting to be worked out. Due to the long term stability of the ice shelves in front of the studied glaciers (see map of the Belgian expeditions in the 60's (Derwael, 1985)), an inter-annual variability is probably insignificant but it does not mean that a trend is nonexistent. The assumption that the system is in steady state is not supported by any evidence. Unfortunately time series of the surface ice flow speed are still not available. The only existing database is a composite snapshot from different sources and time (Rignot et al., 2011a). Identifying whether there is a trend or not in the SRM glacier system, would be a major breakthrough in the understanding of the region.

The mass balance is generally accepted to be controlled by the SMB in Dronning Maud Land (Hanna et al., 2013). Therefore the choice of SMB dataset is a key aspect of the IOM and the temporal variation of SMB is also important. For instance, Shepherd et al. (2012) show that the increasing mass balance observed in DML with GRACE between 2009 and 2011 is driven by a positive accumulation anomaly. Considering a longer time period, they also identify a periodicity of 2 to 4 years in the mass balance. Therefore the results of the IOM should be carefully considered due to this temporal variability of SMB. In addition to this natural variability, the IOM is very sensitive to the choice of SMB datasets (Table 2.2). It is the main pitfall of the IOM : we used 3 SMB datasets and each of them suffer from large uncertainties. The number of control points are too sparse to qualify one instead of another. This is particularly valid for IOM applied to individual basins. In our case study, only 3 data points were located inside the drainage basins. We had to extend our validation area to have enough data points to validate the results of atmospheric modelling or satellite measurements. Therefore we cannot evaluate the different inputs and each of the datasets has to be consider on the same level. Nevertheless, the consistency of each area-integrated SMB gives more confidence in the mass balance assessment: the Sør Rondane glacial system slightly gains mass (between +1.88 and +3.78 $\mathrm{Gt\,a^{-1}}$) during the last 40 years. We also determined that the uncertainties on SMB largely dominate the uncertainty on mass balance. Therefore, refining SMB estimates will highly benefit to IOM studies especially at basin scale.

5.2 Ice dynamics of the West Ragnhild Glacier

As shown in Chapter 3, the glacier dynamics close to the Ragnhild Coast is essentially governed by basal motion. In this section, we focus on the dynamics of the West Ragnhild Glacier (WRG). It is one of the three major glaciers in Dronning Maud Land, together with Jutulstraumen and Shirase glacier. It drains 10.98 Gt per year toward the ocean (Chapter 2). It flows between the SRM and the Belgica Mountains where it concentrates the ice from the Dome Fuji Plateau and exports it toward the Ragnhild coast into the Roi Baudouin ice shelf (RBIS, Figure 3.1). In Chapter 3, we showed a scope of evidences which concludes that the WRG switches from a flow regime driven by the internal deformation (inland) toward a regime driven by the basal motion when it gets closer to the coast. Indeed the observed surface velocity could not be only explained by the internal deformation (Figure 3.6). Basal motion is enhanced by the nature of the bed: geometry suggests that the bed is covered by sediments and reflectivity analysis confirms the presence of water at the ice/bed interface. These factors lower the basal friction. The transition between the two regimes is located inland approximately 65 km away of the grounding line. By modelling, Pattyn et al. (2005) conclude that an enhance basal sliding of WRG induces flux piracy from ERG toward WRG. However, we showed that their is no transfer between the two glaciers and the drainage basins are well apart.

A major concern is to evaluate whether the WRG is stable or not according to the setting described above. Weertman (1974) showed that ice sheet resting on reverse sloped bed below sea level is

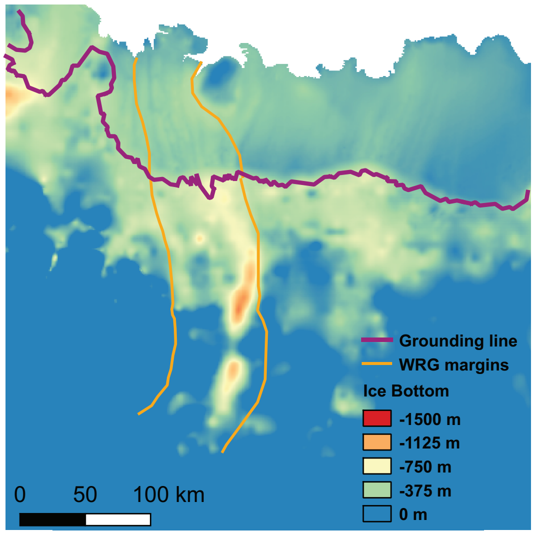

Figure 5.1: Basal topography of the West Ragnhild Glacier. Background color is the ice bottom, i.e. the ice/ocean interface for the ice shelf and the ice/bed interface for the ice sheet (Fretwell et al., 2013). The grounding line is shown in purple (Bindschadler et al., 2011b) and the shear margins of the WRG are in orange (see Figure 5.2). The extent of this figure is the same than for Figure 3.1.

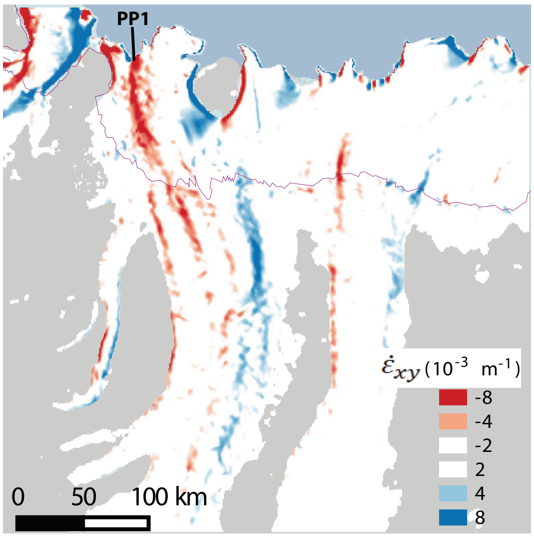

FIGURE 5.2: Map of the lateral shear strain rate. The grey areas are zones where ice moves slower than 15 m a^{-1}. The grounding line is shown in purple (Bindschadler et al., 2011b). The extent of this figure is the same than for Figure 3.1 and Figure 5.1. PP1 = pinning point 1. The methodology and the figure are adapted from Thonnard (2013)

inherently unstable. While Schoof (2007) showed that if the retreat of the grounding line induces an increase of the ice thickness, the ice sheet can not be in steady state. The upstream part of the WRG lies on a flat bed situated 600 ± 100 m below sea level with a minima along the flow line of −700 m (Figure 3.2). Further inland the bed elevation drops at the flowline while it rises under the margins of the glacier (Figure 5.1). Our assessment of the stability regarding the topography is difficult. The 65 first kilometres upstream of the grounding line are very flat but the thickness increases upstream. According to Schoof (2007), a retreat occurring in this area will sustain itself, the grounding line position is hence sensitive to the boundary conditions (SMB and buttressing from ice shelves). Further upstream, the flowline profile (Figure 3.2a) suggests a retrograding slope after the 65th km. However, this valley is very narrow and does not extend under all the trunk of the glacier, high subglacial mountains are observed around this valley (Figure 3.2b and Figure 5.1). With this configuration, grounding line may be stable because the sides are higher and ice is still grounded there. These higher margins exert lateral friction which stabilizes the flow (Gudmundsson et al., 2012). This setting is missing near the grounding line and could not stabilize the flow. In case of a decreasing of the buttressing exerted by the ice shelf, the grounding line has the potential to retreat until it reaches the subglacial mountains approximately 60 km upstream of the current grounding line and then find a stable position.

WRG is hence sensitive to what happens downstream, on the Roi Baudouin Ice Shelf. Three main features play a role in stabilising its flow : Derwael Ice Rise (DIR), FranKenny Ice Rise (FKIR) and the pinning point 1 (PP1, Figure 1.7 and 1.9). Their impact is particularly visible on the lateral shear strain rate ($\dot{\varepsilon}_{xy}$) map (Figure 5.2). This strain rate is calculated via the following equation :

$$\dot{\varepsilon}_{xy} = \frac{1}{2}\left(\frac{\partial u}{\partial y} + \frac{\partial v}{\partial x}\right), \tag{5.1}$$

where u is the surface speed in the direction of the flow (x) and v is the surface speed perpendicular to the flow (y). High absolute values of $\dot{\varepsilon}_{xy}$ mean that the lateral shearing is important. These denote the interface between the fast moving ice stream and the motionless surrounding ice and are usually used to define the margins of the ice streams. On this map (Figure 5.2), the role of the ice rises is obvious. They induce very strong speed gradient and their influence can be traced back far upstream. On the east side of WRG, the margin is well-defined while on the west side, the shear margin is separated into 3 shear zones on the grounded part (Figure 5.2). These zones merge into the ice shelf. These shear margins are the expression of important lateral friction which stabilizes the flow.

Obviously, a decreasing of the buttressing due to the RBIS will promote an acceleration of the glacier as this buttressing highly depends on the interaction between the ice shelf and the ice rises. The size of DIR and FKIR prevents them to detach of the ice shelf. Their influence can be considered as stable in a long term perspective. On the other hand, PP1 is smaller and its flow regime is not fully decoupled from the surrounding ice shelf (R. Drews, personal communication). The buttressing from this pinning point may faster decline under changing sea level or thinning of the ice shelf. The consequences could be important since it is a major provider of friction (Figure 5.2). Mercenier (2014) modelled the consequences of the unpinning of PP1 and concluded that it will increase the mean speed of RBIS by 15% and divert the flow in the direction of the FKIR.

The ice shelf downstream of East Ragnhild Glacier is probably more unstable : the alternating from red to blue on Figure 5.2 denotes the presence of several small pinning points in front of ERG. Therefore this part of the ice shelf is probably more sensitive to sea level change. In case of unpinning of these small ice rumples, the resistance to the flow may be smaller on this side of DIR and WRG will deviate in this direction. Indeed, the bedrock does not offer obstacles against a lateral migration of WRG (Figure 5.1). Variation of this flow field around DIR might have happen in the past. By modelling the Raymond Bump observed in this ice rise, Drews et al. (2014) demonstrated that the today's geometry could not be explained without a significant thinning of the DIR which occurred recently. This is most likely due to the change of the margins' thickness of the ice rise. The ice shelf thinned triggering the thinning of the ice rise. Similarly, a change of the flow pattern around DIR could unbalance it and lead to displacement of the ridge.

5.3 Subglacial processes

5.3.1 Processes under the ice sheet

In Chapter 3, we have seen that West Ragnhild Glacier overlies a water-rich substrates and temperature modelling has shown that pressure melting point is reached everywhere under the downstream area of WRG. It means that subglacial melting very likely occurs. Furthermore, we suspect unconsolidated sediment under the ice. In this substrate, water can flow in the porous medium. If water pressure overcomes the overburden pressure from ice mass, the sediment is unstable and can actively deform (Boulton and Hindmarsh, 1987). Several metres of deformable sediments have already been observed in Antarctica, e.g. beneath the ice stream B (Blankenship et al., 1986). Subsequently, Alley et al. (1986) suggested that the flow regime of this glacier is dominated by the till deformation. Another mechanism of basal motion is basal sliding. Basal sliding is likely when bed is at the temperature of the pressure melting point and when water is present (Van der Veen, 2013). Both mechanisms are likely playing a role in the motion of WRG but discretize their impacts is impossible without additional information.

Therefore, subglacial water behaviour is a key factor of ice dynamics. Water under ice masses behaves in two ways. It can occupy the whole interface between ice and bed or it can concentrate in few subglacial channels which drain the rest of the interface (Cuffey and Paterson, 2010). The evidences exposed above tend to opt for the first hypotheses. However, Le Brocq et al. (2013) discovered a coincidence between zones with an high hydraulic potential close to the grounding line and trenches in the subsequent ice shelf and used RBIS as an example of their hypotheses. Hence,

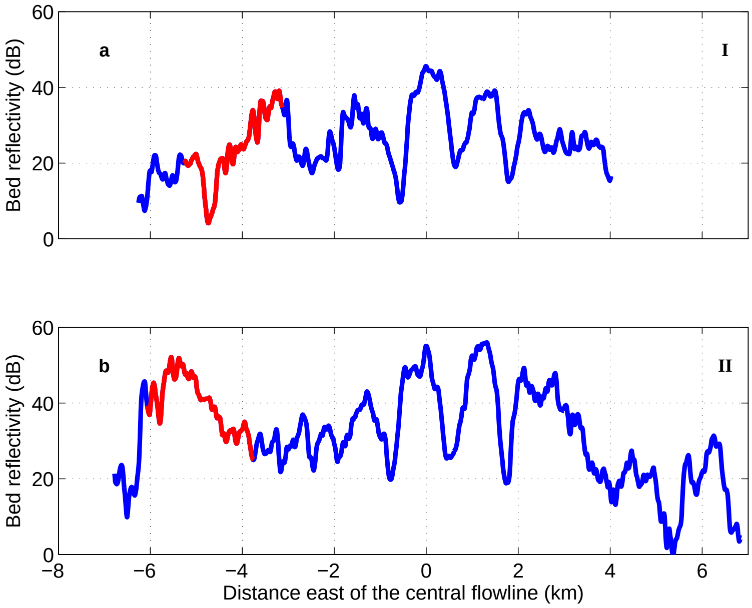

Figure 5.3: Reflectivity of the two downstream profile (I and II) of Figure 3.2. Reflectivity is obtained by method described in Chapter 3. Red curves denote the high hydro–potential zone according to Le Brocq et al. (2013).

they implicitly favoured existence of a structured subglacial water system. However our analysis described in Chapter 3 emphasizes the importance of basal motion usually promoted by widespread and continuous water layer. Furthermore, the reflectivity estimation across the flow (Figure 5.3[1]) does not show any characteristic changes in the high hydraulic potential zone described by Le Brocq et al. (2013) while presence of large amount of water should have a signature in reflectivity signal. The evidences presented in this document counteract the hypotheses of a structured water system. Secondly high hydro-potential and large sub ice sheet channel may not lead to a sub ice shelf channel (e.g. Whillans Ice Stream, Horgan et al., 2013). Therefore assessing that the longitudinal flow stripes observed on RBIS (Figure 5.7) originate from subglacial melt water influx from the grounding zone is questioned by the data we have.

The study of the water conditions at the bed will certainly benefit to the understanding of the WRG dynamics. This study has also open new perspectives for glaciological research in the region. A network of seismometers will be installed near the grounding line and will focus on the short time scale ice dynamics. In the meanwhile, another place is subject to growing concern : the RBIS. The changes affecting it will likely have a greater and faster impact on the dynamics and equilibrium of the WRG.

5.3.2 Processes under the Ice shelf

Neither Pritchard et al. (2012), nor Depoorter et al. (2013) observe significant imbalance in the mass budget of east DML ice shelves. This does not mean that subglacial processes are absent. In east DML sector, basal melting is half of the total mass loss (Depoorter et al., 2013). This is compensated by mass influx from ice sheet. Only one glacier is imbalanced, the H.E. Hansenbreen, for which icesat data reveal a thickness decreasing of ≈ 1 m a^{-1} between 2003 and 2008 (Pritchard et al., 2012).

[1]Please do not compare absolute value from Figure 5.3 to the one in Figure 3.5. These profiles were collected another day and calibration does not succeed. Nevertheless relative changes are meaningful.

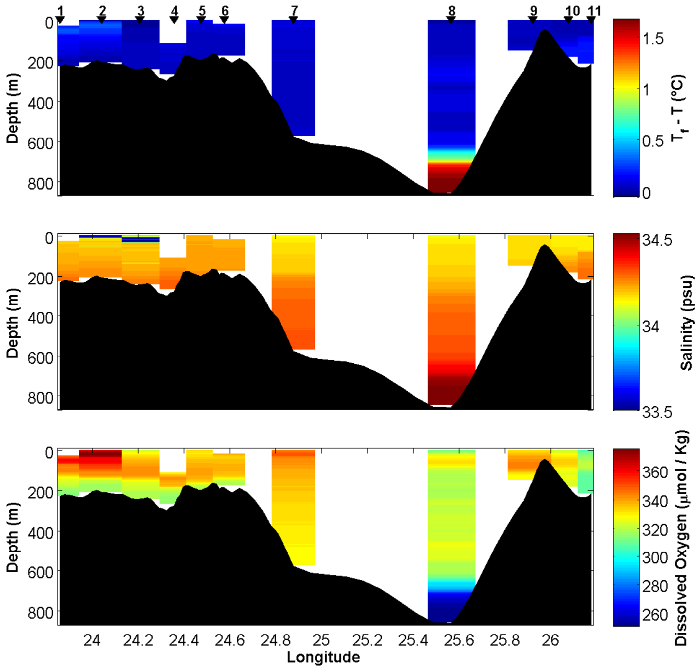

FIGURE 5.4: North-Facing Oceanographic Sections. Results of CTD measurements are plotted here for each individual casts. These casts were made along a roughly ice front parallel line following latitude 70°10 S (see Figure 5.7 – yellow dots with the same numbering). Bedrock topography is from bathymetric measurements (Derwael, 1985) and CTD casts. Water temperature relative to the local freezing point (top) was calculated following (Holland and Jenkins, 1999); salinity (middle) and dissolved oxygen (bottom). The three panels demonstrate the presence of warmer, saltier, low-oxygen water in the deepest part of the trough, characteristic of mCDW.

What is triggering this melting beneath the ice shelf? On Amundsen continental shelf, massive input of warm Circumpolar Deep Water (CDW) had induced significant melting beneath the ice shelf and subsequently destabilized the flow of Pine Island and Thwaites glaciers (Jacobs et al., 2011). The situation is very different beneath RBIS. Firstly, the estimate basal melting is one order of magnitude lower in DML than in Amundsen sea sector (Depoorter et al., 2013). Secondly, interaction between CDW and Roi Baudouin Ice shelf cavity is very unlikely. In DML, the Antarctic Circumpolar Current (ACC), bearing the CDW, is pushed north by the Weddell gyre. This gyre extends from the Antarctic peninsula to approximately 20°E and turns clockwise between the ACC and the coast (Orsi et al., 1995). It carries cold water. Nonetheless, the conductivity-temperature-depth (CTD) casts made in 2011 (Leonard et al., Prep) revealed presence of water that looked alike CDW at least in one location (Figure 5.4). In a deep through below the ice shelf, warmer water is observed at depth greater than 700 m. Its properties deviates significantly of the shelf water properties: (i) its potential temperature[2] is higher than -0.5 against <-1.5°C, (ii) its salinity is 0.5 practical salinity unit (psu) higher than in shallower water and (ii) its concentration in oxygen denotes water which didn't exchange gases with the atmosphere for a while.

This water is different than shelf water but it is still significantly different than CDW. Indeed, the potential temperature of the CDW in the region is 1.9°C, the psu=34.7 and the dissolved oxygen is <200 μ mol kg^{-1} (Meijers et al., 2010). Therefore the water observed is as far from the shelf water composition than from the CDW composition. It is called modified circumpolar deep water (mCDW) due to its formation process.

[2]The potential temperature is the temperature that the water would acquire if adiabatically brought to the atmospheric pressure. This temperature is different than the one plotted in Figure 5.4.

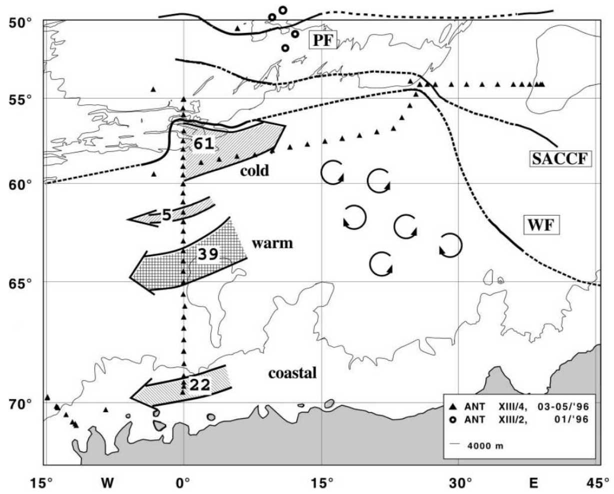

FIGURE 5.5: Observed situation of the water mass movement offshore of DML in 1996. Triangles and circles refer to the location of CTD casts and velocity measurements. Black lines depict fronts between water masses. PF = Polar Front; SACCF = Southern Antarctic Circumpolar Current Front, WF = Weddell Front. Big arrows are the main water fluxes with the amount in Sv in them. Circular arrows denote the presence of eddies. Figure adapted from Schröder and Fahrbach (1999)

Offshore of DML coast, mCDW results from the mixing of the cold water of the Weddel gyre and CDW of the ACC. The Weddell gyre flows eastward from the Antarctic Peninsula and turns back coast ward around 20°E. Since ACC is not pushed north any more by the Weddell gyre, its flow is inflicted toward the coast(Figure 5.5). In the interval between the two currents, mixing occurs trough an intense mesoscale eddy field located between 15 and 30°E just in front of the RBIS (Schröder and Fahrbach, 1999).

In the mean while, a westward wind located 63°S induces a Ekman transport of water toward the south. This current is deviated westward by coriolis forces (Whitworth et al., 2013). When this current will arrive close to the continental margin, it will encounter the Antarctic Slope Front (ASF). This front is a temperature gradient between mCDW and a thicken layer of Antarctic surface water on the continental shelf. Water coming from the north is blocked there and accumulated to produce the Antarctic slope current : a strong westward current flowing along the continental slope (Jacobs, 1991).

In the east of RBIS, Meijers et al. (2010) made a profile along the 30°E meridian (upstream of RBIS in regard of the Antarctic slope current) and identified water with the same properties observed in the CTD casts presented in Figure 5.4. This water was observed at depth as shallow as 400m. Therefore the trough observed under the ice shelf is the easy way for mCDW intrusion in the ice shelf cavity.

In the ice shelf cavity of RBIS, water of 1.5°C above the in-situ freezing point is observed beneath the 700 m isobath (Figure 5.4). This is approximately the range of depth WRG reaches at the grounding line (Figure 3.2). Therefore, if there is no obstacle between the front and the grounding line, the warmer mCDW has the potential to reach the ice and melt it. It is yet worthy to note that we have no evidence of any ice-ocean interactions at the grounding line of WRG.

However, in recent years, direct evidences of this basal activity in other locations under RBIS have been observed. Pattyn et al. (2012) have shown that the geometry of internal reflection horizons cannot be resolved if basal melting close to the grounding line is neglected. Since basal melting and surface accumulation anomaly do not act on isochrones geometry on the same way. Minimization of the difference between observed and modelled layers regarding these two parameters permits to

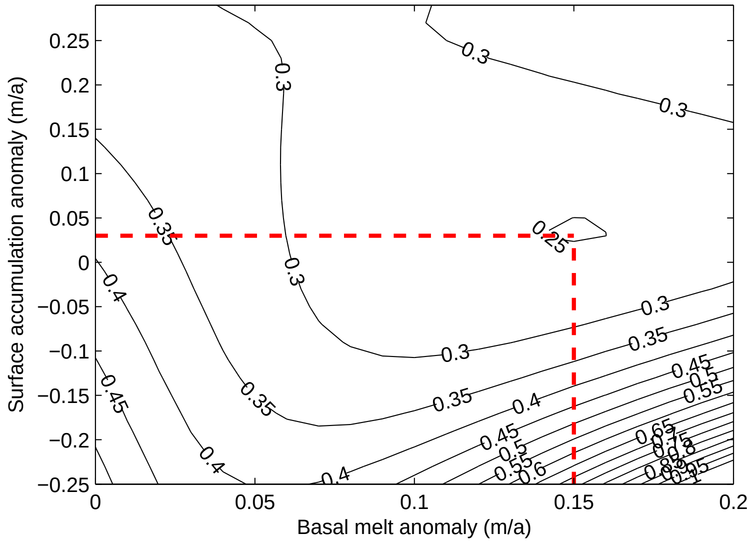

FIGURE 5.6: Minimization of the RMS error (m) between observed and modeled isochrones for different combinations of accumulation/ablation and basal melting near the grounding line. The best fit is obtained with basal melting of 0.15 m a^{-1} and no accumulation anomaly. This figure is a reproduction of Figure 3 in Pattyn et al. (2012).

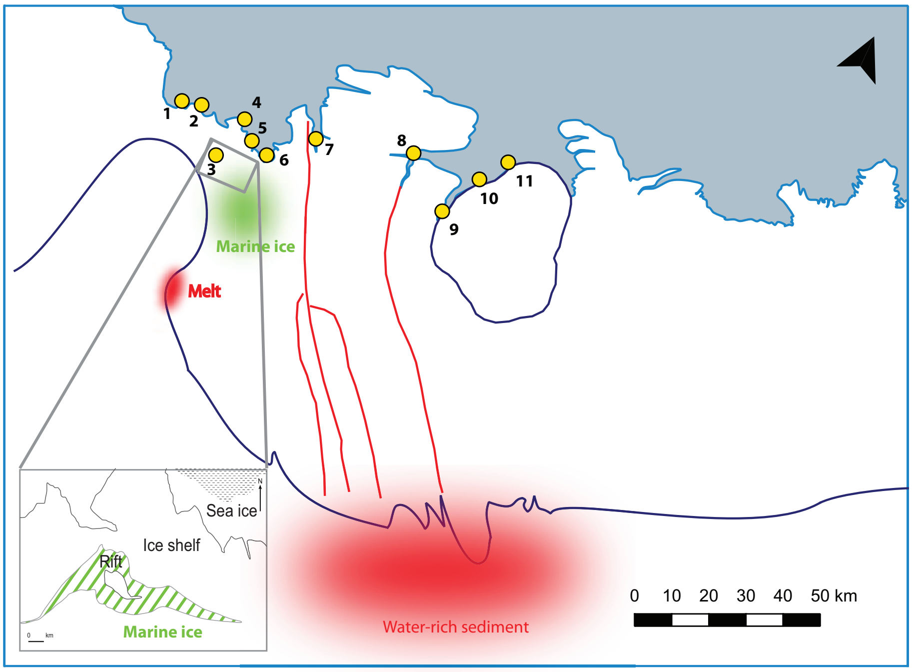

FIGURE 5.7: Summary of the subglacial processes occurring under the ice. Dark blue lines are the grounding lines, light blue line is the ice shelf front, red lines are longitudinal flow stripes. Small red spot is the location where melting is found and big red spot in the south is the water saturated sediment region discovered in Chapter 3. The green spot is the place where Gossart (2014) has found evidences of marine ice. The yellow dots are the location of the CTD casts with the same numbering as Figure 5.4 Inset : Map of the rift where 10 cores were drilled. In each of them marine ice was found.

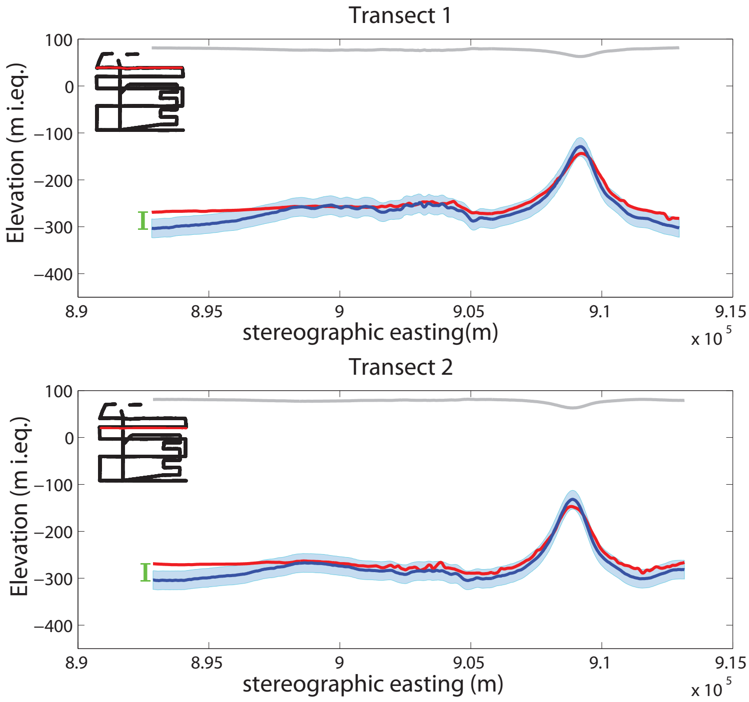

FIGURE 5.8: Geometry profiles of the two most northern transect of the bewise project. Light grey line is the surface measured with GPS, red line is the ice shelf bottom inferred with radar and blue line is the ice shelf bottom inferred with GPS assuming the hydrostatic equilibrium. The blue shade is the error range of GPS inferred bottom. The elevations are in meter of ice equivalent. The green bar is the discrepancy between the two methods at the west end of the profiles. The top left inset shows the position (red) of the profiles in the bewise dataset (black). This figure is adapted from Gossart (2014).

discretize their relative influence. There is no accumulation anomaly while we estimate the basal melting around 0.15 m a^{-1} (Figure 5.6). Position of this observation is shown on the Figure 5.7.

Pattyn et al. (2012) alse present evidence of marine ice accretion in the rift system of the RBIS. Four ice core were drilled in and around a rift close to the ice shelf front (Figure 5.7). Marine ice is melted water which refreezes at shallower depth when the incoming heat flux is not enough to sustain the melting. Hubbard et al. (2012) also found evidences of marine ice in 10 boreholes drilled in 2008 and 2010 in the same rift, north of FKIR. Nevertheless, this marine ice is not necessarily an evidence for a global thermohaline circulation into the ice shelf cavity. In rifts, the bottom of the sidewall can melt and refreeze at shallower depth creating a significant layer of marine ice (Khazendar and Jenkins, 2003). Nevertheless, marine ice worthes to be investigate since it can have a major impact on the stabilisation of ice shelves by filling the suture zone with mechanical soft ice (Kulessa et al., 2014).

Gossart (2014) combined depth inferred from GPS and radar to study the distribution of marine ice beneath the bewise's velocity markers grid (Figure 1.9). Assuming hydrostatic equilibrium, the elevation measured by GPS can provide the ice thickness. In parallel, radar allows to identify the depth of the ice bottom. As marine ice is opaque to radio electromagnetic waves (Thyssen, 1988), the radar signal comes from the bottom of the meteoric ice while the GPS derived thicknesses take into account the whole ice column (meteoric and marine ice). With this method, Gossart (2014) identifies a zone where the discrepancy is quite high ($\approx$ 35 m) at the west end of the 2 northern most lines of bewise's velocity markers (Figure 5.8). We interpret this difference as an evidence of marine ice presence at the bottom of the ice. There, the discrepancy exceeds the error. Therefore, we can safely assume that there is marine ice. Unfortunately, this comparison is very sensitive to density of the ice column. Therefore, Gossart (2014) used an other method which brings confidence to these results. She calculated the basal mass balance of different boxes. With interferometry, it is possible to evaluate the flux which crosses the sides of the boxes. Then a constant surface mass balance is assumed : 0.25 m i.eq (Hubbard et al., 2012). In the place where marine ice is suspected, the box calculation returns accretion (≈1.01 m i.eq. a^{-1}) which is in line with the first method. In the rest of the bewise grid, it gives a slight melting (≈0.57 m i.eq. a^{-1}). This is the same order of magnitude as the surface mass balance. This is why the results of this method have to be carefully considered. Firstly, in Lenaerts et al. (2014), the modelled SMB on the RBIS is larger and, secondly, the method used by Hubbard et al. (2012) underestimates the SMB on DIR (M. Philippe, personal communication). Since SMB is probably higher than assumed, it weakens the results of box calculation where melting is found but strengthens it where accretion is found.

A scope of indirect evidences suggests that thermohaline activity occurs in the ice shelf cavity. The magnitude of mass transfer between cryosphere and ocean is difficult to assess regarding to the data we have but continental wide studies say that RBIS is in equilibrium (Pritchard et al., 2012). The stability of this equilibrium is directly linked to the ability of warm mCDW to reach the grounding line or not. Indeed mCDW could initiate sustained melting all along the ice shelf cavity roof (Holland et al., 2008). To evaluate this possibility, bathymetric mapping under the ice shelf is required.

5.4 Surface mass balance variability over ice rises and Roi Baudouin Ice Shelf.

Mass balance and dynamics of a glacier depend on its lower interface as well as the processes acting at the surface. In Chapter 4, we described how the shape of ice rises can affect the surface mass balance. A strong gradient of accumulation is observed across the Derwael Ice Rise. It appears in shallow layering and in the shape of deeper layers. This gradient was already observed in other places (King et al., 2004, Lenaerts et al., 2014, Nereson et al., 2000). Lenaerts et al. (2014) analysed the results of atmospheric modelling over numerous ice rises in DML and concluded that SMB has a parabolic shape with an apex located a few kilometres of the divide, on the wind side. To test these findings, we presented a new method to reconstruct the SMB associated with deep internal reflection horizons (IRH). By inverse modelling, the geometry of the IRHs can be related to the most likely distribution of accumulation. The SMB of DIR varies from 0.3 to 0.9 m w.e. a^{-1} and the distribution is consistent for shallow and deep layers.

To test the ability of the model to perform the same analysis on other places, we consider the FranKenny Ice Rise. As explained in introduction, a geophysical survey was performed on this ice rise which results in 6 IRHs (Callens, 2010). We decided to consider the northern profile which crosses the FKIR (Figure 1.9 and Figure 5.9a). They were dated at the divide via Nye time scale with an initial accumulation rate at the divide equals to 0.4 m w.e. a^{-1}. Then we applied the method described in Chapter 4. However, we did not remove the central part of the profile as we did for DIR since we consider that the Raymond effect is weaker and does not affect excessively the geometry of the IRHs.

The optimisation performs extremely well as revealed by Figure 5.9c. The optimized SMB (Figure 5.9b) is slightly different from the one from DIR (Figure 4.3) and does not fully agree with conclusion of Lenaerts et al. (2014). Even if the SMB doubled on the wind side compared to the lee side, it does not have a parabolic shape. This proofs that the model can be applied to other ice rises and produces promising results.

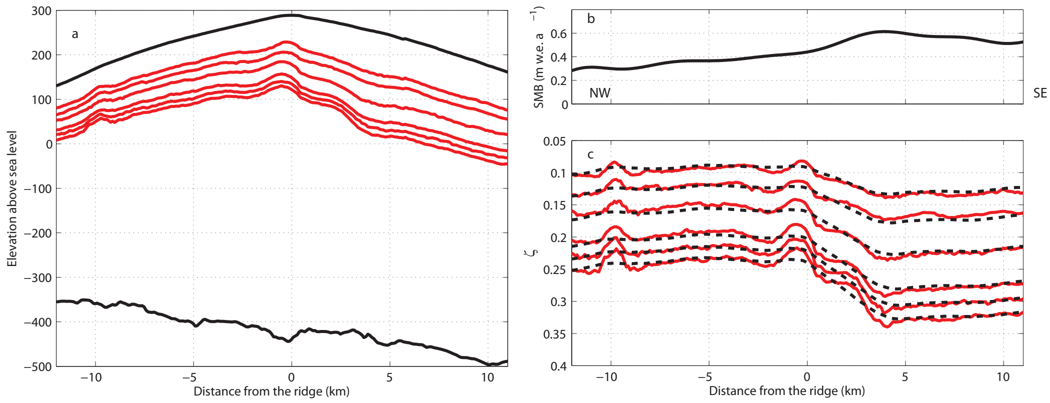

FIGURE 5.9: Data and results of the inverse modelling on FranKenny Ice Rise. (a) Geometry of the surface and the bed (black) and the IRHs (red) across FKIR. (b) SMB distribution which produces the best match between modelled and observed IRHs. (c) Comparison of the observed IRHs with the modelled ones using the most likely SMB distribution.

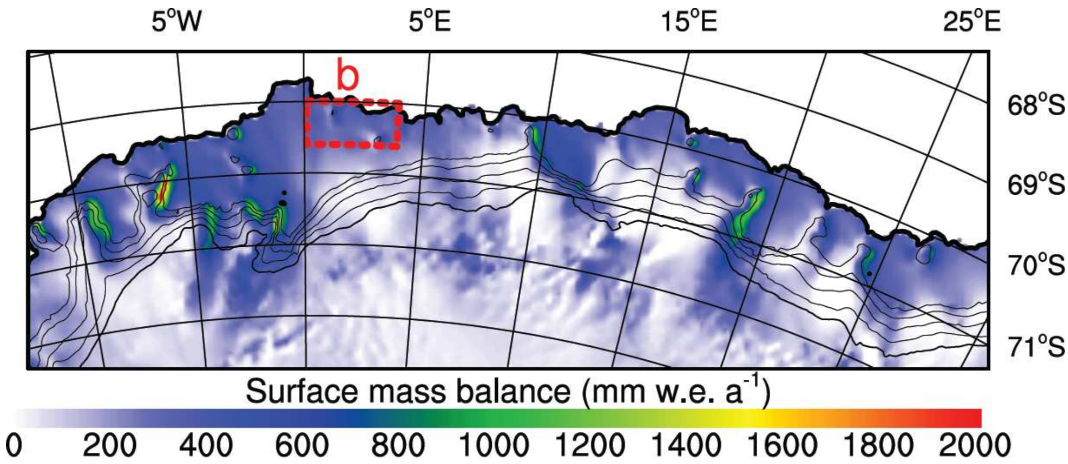

FIGURE 5.10: RACMO2 mean (2001–2012) annual SMB in entire coastal Dronning Maud Land. Contours show the surface topography (Bamber et al., 2009) with a contour interval of 200 m. This map is a reproduction from Lenaerts et al. (2014).

All along the coastline of DML, this asymmetry is observed across numerous ice rises (Figure 5.10). Regional atmospheric modelling has demonstrated that the orographic uplift associated to the ice rise induces an increase in precipitations on the wind side and a deficit on the lee side. The down-slope on the lee side is characterized by erosion due to wind acceleration (Lenaerts et al., 2014). Both processes compete to produce an asymmetric pattern of the surface mass balance (SMB). Apart from the sharp gradient across ice rises, the SMB of the ice shelves varies very little (Figure 5.10) except downstream (regarding to the air flow) of the ice rises were SMB shadow can be observed almost next to each ice rise.

Knowing the SMB pattern is interesting for many reasons. Firstly, reconstruction of the SMB with IRH geometry allows to calculate since how long the current SMB pattern is active or to date changes in the atmospheric circulation. For instance, Morse et al. (1998) showed that prevailing storm trajectories over Taylor Dome were reversed during the last glacial maximum by analysing the IRH geometry. Secondly, the gradient of accumulation is a major interest in choosing the location of an ice core site. Area of low accumulation gives a larger time span while higher accumulation produces a finer time resolution. Finally as the surface geometry is also a function of the SMB pattern, this asymmetry may have an influence on the divide position.

Chapter 6

Conclusions

Thanks to a multidisciplinary approach, we were able to draw a comprehensive descritpion of the Sør Rondane Mountains (SRM) glacial system. We combined different types of new measurements as well as different types of model into novel analyses techniques to achieve this description. We analysed multiple factors which determine the mass balance of ice sheet and the system is now profoundly better understood.

The SRM glacial system slightly gains mass but stays close to the equilibrium with an imbalance of $+3.15\,\mathrm{Gt\,a^{-1}}$ according to the latest SMB dataset. Ice accumulates on the continent via the solid precipitations. It compacts and flows downward in the direction of the coast. In Dronning Maud Land, ice has to flow around obstacles such as mountains and therefore concentrates into valleys to produce outlet glaciers. For instance, West Ragnhild Glacier (WRG) emerges from the Dome Fuji through the valley between the SRM and the Belgica Mountains. These valleys are the favoured output gates for ice from the plateau. After the mountain range, several of these outlets may merge (e.g. Tussebreen) and form large ice streams which drain several gigatons of ice per year.

The amount of ice transported depends on the dynamics of these glaciers. Downstream of this mountain range, a large lowland covered by sediment was discovered beneath the WRG. This sediment layer probably deposit when the Antarctic ice sheet was smaller and bounded by the mountains. This till is extremely flat and saturated with water. Firstly, basal motion is enhanced by this setting as well as the total speed (Chapter 3). Secondly, flatness of the bed suggests that the position of the grounding line directly depends on the conditions downstream of the glacier, i.e. on the ice shelf. As shown for Roi Baudouin Ice Shelf (RBIS), the ice rises (such as Derwael Ice Rise) play a dominant role on stabilising the flow by inducing strong lateral shearing while ice rumples (such as PP1) induce basal friction. Therefore, it slows down the flow of the ice sheet.

This configuration seems stable but has one weakness: its proximity to the open ocean. The trough observed in front of RBIS allows warm ocean water to enter in the ice shelf cavity and, maybe, reaches the grounding line. This can initiate sustained melting and subsequently thin the ice shelf, decreasing the area of contact between ice and ground. This can destabilize the ice shelf and induce an acceleration of the mass transfer from the cryosphere to the ocean.

Studying drainage basins of the SRM glacial system is interesting because the other drainage basins in Dronning Maud Land look like it (Figure 6.1). Ice has to cross a mountain range to reach the coast and, hence, concentrates into narrow glaciers. These glaciers flow into small ice shelves surrounded by ice rises. These ice rises buttress the flow and prevent the grounding line to retreat. Finally, all these ice shelves have the same weakness. Their front reaches the continental slope. This setting promotes interaction between ocean and the ice shelf cavity.

The Weddell gyre and its cold water prevent warm circumpolar deep water to reach the coast of Dronning Maud Land. However, we saw that the Antarctic slope current can carry a significant

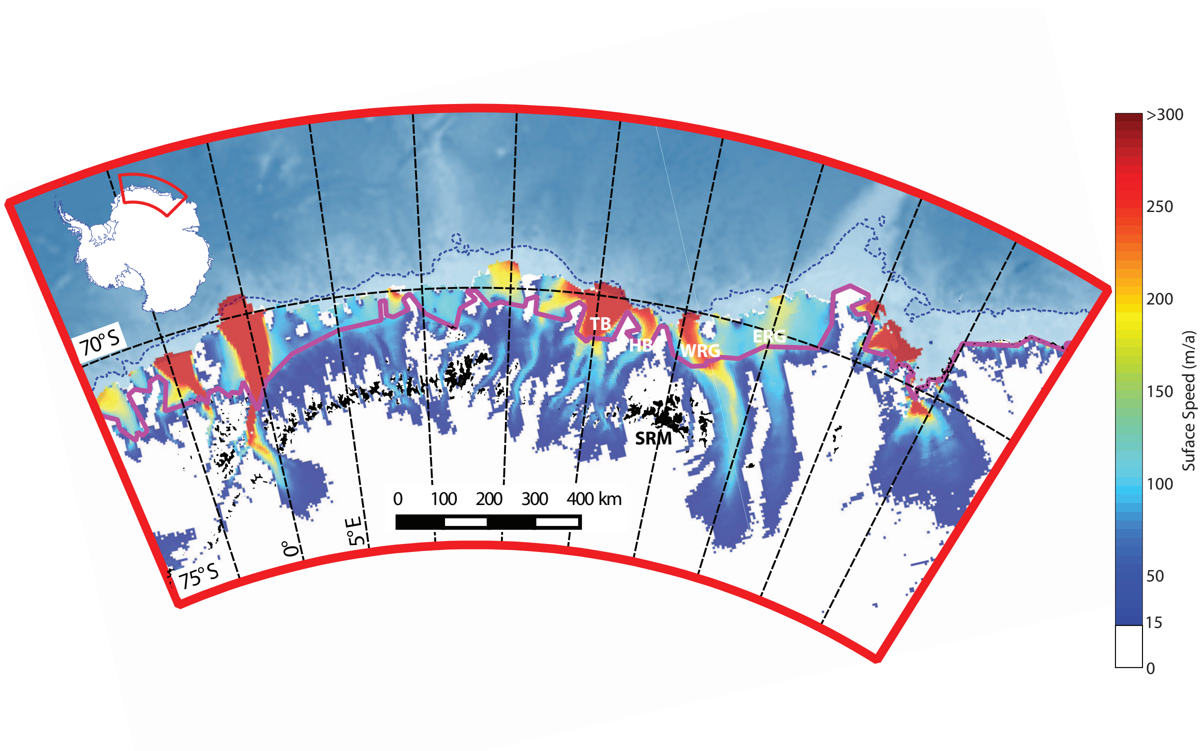

FIGURE 6.1: Overview map of the eastern Dronning Maud Land. Background on the continent is the ice flow speed (white when $< 15\,\mathrm{m\,yr^{-1}}$; Rignot et al., 2011a). The grounding line is shown in purple (Bindschadler et al., 2011b). The dotted blue line is the isobath of 1000 m of depth denoting the continental slope. Rock outcrops are shown in black (SCAR, 2012). SRM stands for Sør Rondane Mountains and the glaciers acronyms are: TB is Tussebreen, HB is H.E. Hansenbreen, WRG is West Ragnhild Glacier and ERG is East Ragnhild Glacier. The inset shows the coverage of the map.

amount of water from east to west. This water is warmer than the freezing point but it flows deep (>700 m of depth). Therefore two conditions have to be fulfil to allow interaction between ice and ocean: (i) the ocean bed should provide a deep enough path to allow warm water to reach the grounding line and (ii) the ice has to be thick enough to allow interaction with warm water. The latter is relatively easy to investigate (via radar measurements). On the other hand, mapping the ocean floor into the ice shelf cavity is extremely complex and requires heavy logistics. In our opinion, the long term stability of the eastern Dronning Maud Land will still remain unclear for a while, as long as we don't know the potential of interaction between the ice sheet and the ocean.

Little is known about mass balance and ice dynamics in eastern DML. Few studies focussed on this part of Antarctica because of the conviction that no change happens. It is often consider as non-responsive to climate changes. However, we identified weaknesses which may mean an important potential responsiveness at the ocean margin of DML.

Appendix A

Radar in glaciology

Radio-echo sounding in glaciology is a geophysical technique designed to investigate the interior of the ice masses as well as the underlying bed properties. Its principle is based on the dielectric heterogeneity of the medium in which radar waves propagate. At the interface between two media with different dielectric properties, a radar wave behaves in three ways : a part of the energy is spread, a part is refracted further and a part is reflected back to the source of the wave. The latter is the target of the radio-echo sounding.

A radar system is composed of a transmitter and a receiver (Figure A.1). The transmitter sends an electromagnetic wave which propagates through air and ice. The receiver records the time of arrival of the air wave and the reflected wave. The difference between them is the time the wave took to reach the reflector and come back. If the velocity of the wave is known, the depth of the reflector can be calculated.

The wave speed in pure ice is $168 \pm 2\,\mathrm{m}\,\mu\mathrm{s}^{-1}$ (Bogorodsky et al., 1985). Unfortunately, ice sheets are covered with a layer of firn. The firn is compacted snow which will become ice. It is characterized by a lower density. Since density is a first order parameter in the definition of the wave speed, knowing the density-depth profile is a requirement to calculate the depth of a reflector. When the reflector is deeper than the firn/ice interface, the depth correction is a constant value ($\approx 10\,\mathrm{m}$) applied all along the profile. When the reflector is shallower, the correction depends on the depth and an accurate profile of density.

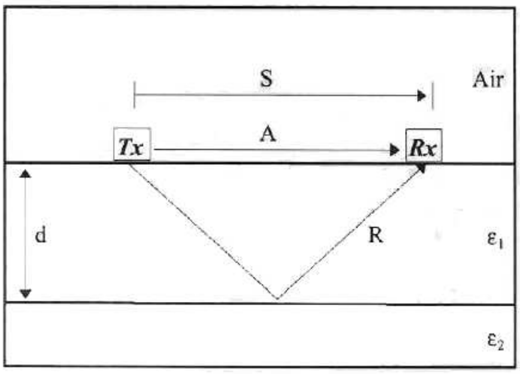

Figure A.1: Schematic illustration of a radar wave propagation through ice. Tx and Rx are the transmitter and the receiver. S is the distance between them. A and R represent the path of propagation of the radar wave in air and in ice, respectively. ε_1 and ε_2 denote the electric properties of 2 different media. They can be two layers of ice or ice and bed. Finally d is the distance between the surface and the reflector. d is the quantity we are interest in. Figure adapted from Delcourt (2012)

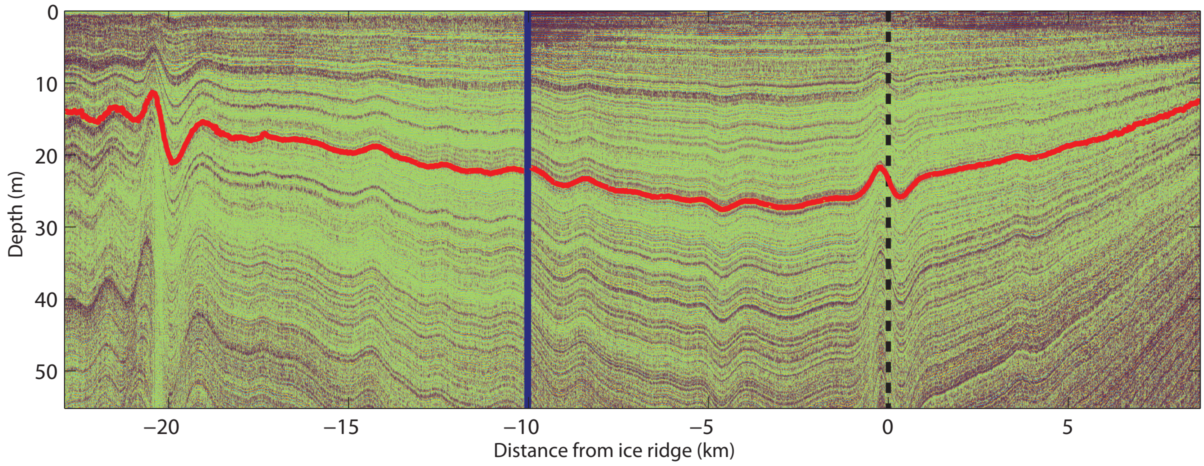

FIGURE A.2: Ground-penetrating radar profile across the Derwael Ice Rise. Its location is mapped on Figure 4.1. Red curve denotes the reflector picked. Dashed black line is the position of the ridge and the firn core (Hubbard et al., 2013). The blue line denotes a gap in the data.

In this thesis, we consider two types of reflectors: the ice/bed interface and the internal reflection horizons (IRH). Detecting the bed echo allows to calculate the ice thickness. We were able to map the bed geometry in Chapter 2 and 3. While we picked the IRHs in Chapter 4 to reconstruct the surface mass balance. IRHs are discontinuities due to a change of (i) density, (ii) acidity and (iii) ice fabric (Fujita et al., 1999). Indeed IRH is a former surface which was buried by accumulation of snow above it. Therefore, their geometry is influenced by the history of SMB. Deeper is the layer, more it is affected by the ice dynamics. Understanding the geometry of IRH includes both aspects. Figure A.2 displays an example of layer picking on the radargram of the 400 MHz profile across Derwael Ice Rise Figure 4.1.

Appendix B

Outflux of the SRM glacial system according to the hydrostatic assumption.

A common assumption made in estimation of the outflux of a drainage basin is the hydrostatic equilibrium. Indeed thickness of the outflux gate is often unavailable since no radar survey has been yet carried out along the grounding line. This leads scientists to consider another way to calculate ice thicknesses. Where ice freely floats, its thickness directly depends on surface elevation through Archimedes principle: ice thickness is approximately 9 times the height above sea level of the surface. This method is widely used since surface elevation is easier to estimate especially with satellite-based estimates.

Unfortunately calculating ice thickness in this way introduces several significant errors. Firstly, the place where ice detaches from the bed and the place where it freely floats can be separated by several kilometres and intense basal melting can occur in the interval. Secondly, determination of thickness is less accurate than the one derived from radar. Following (Fretwell et al., 2013), the error is ±150 m while error on radar derived thickness is ±30 m (Callens et al., 2014).

To illustrate this issue, we compared the flux estimated upstream of the grounding line with radar data (Table 2.2) and flux derived upstream of the grounding line (Table B.1). We defined output gates on the ice shelf sufficiently downstream of the hydrostatic line[1] (Figure B.1) to be freely floating. They were chosen to cover a maximum of the flux flowing through the gates upstream. We used Equation 2.1 to calculate the flux : the speeds are from Rignot et al. (2011a) and the thicknesses are coming from Fretwell et al. (2013).

Table B.1 displays the mass budget using the new outflux estimates. The results are significantly different than for the grounded gates. While analysis presented in Chapter 2 suggests the SRM

[1]Hydrostatic line is the line where ice reaches the hydrostatic equilibrium.

TABLE B.1: Results of the mass budget (Gt a^{-1}) using the SMB from Van Wessem et al. (2014) and the outflux estimated downstream of the grounding line. TB is Tussebreen, HB is H.E. Hansenbreen, WRG is West Ragnhild Glacier and ERG is East Ragnhild Glacier. W14 stands for Van Wessem et al. (2014).

	TB	**HB**	**WRG**	**ERG**	**Total**
SMB (W14)	8.82 ± 2.29	5.23 ± 1.36	11.03 ± 2.87	6.39 ± 1.66	31.47 ± 8.18
Outflow	7.81 ± 2.45	3.56 ± 0.95	6.39 ± 2.80	3.57 ± 2.06	21.33 ± 4.36
Mass Budget	1.01 ± 3.36	1.67 ± 1.66	4.64 ± 4.01	2.82 ± 2.65	10.14 ± 6.09

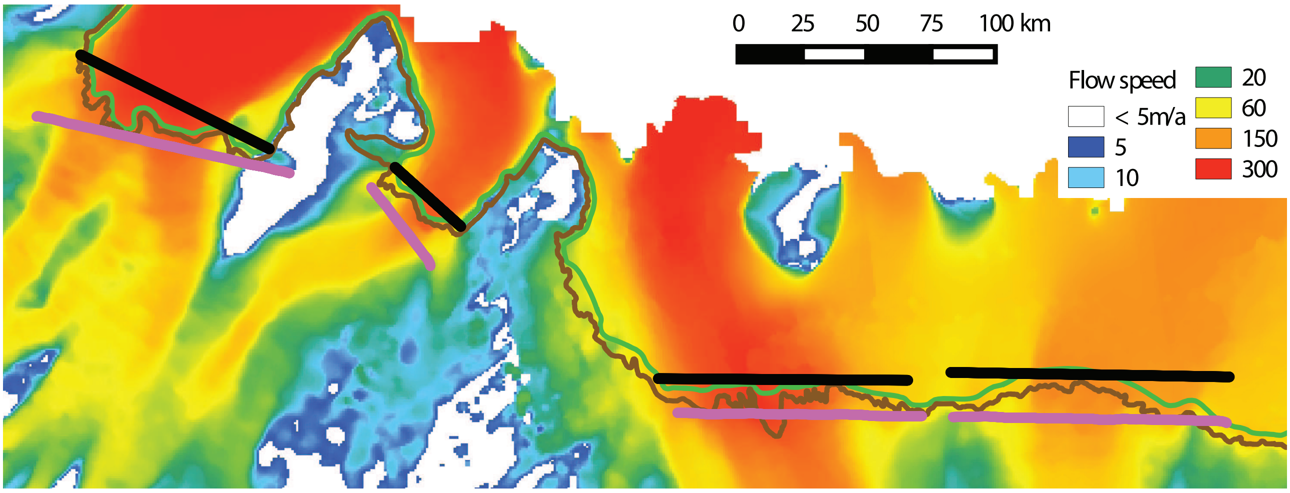

FIGURE B.1: Map of the output gate of the SRM glacial system. Brown line and green line are grounding line and hydrostatic line, respectively. Pink lines are the gate of Chapter 2 and black lines are the gate used in this appendix.

glacial system to slightly gain mass, the new estimates conclude to a huge gain of mass (>10 Gt a^{-1}).

Even if the discrepancies between the estimates presented in Chapter 2 and here are large, several weaknesses have to be set out. Firstly, intense basal melting can occur between the two gates and it affects the mass budget because it is a sink of mass which are not take in account in the IOM. Secondly, the gate defined downstream of the grounding line may not cover exactly all the flux from upstream gates. Divergence may occur and the different gates may not be consistent. Finally as expressed by the large uncertainties presented in Table B.1, caculating ice thickness assuming hydrostatic equilibrium is inaccurate. This comparison emphasizes the risk of using an output gate downstream of the grounding line.

Nevertheless, the discrepancy is so large that basal melting should definitely occur at the grounding to explain it. In the case of WRG, it is probably linked to the warm water observed at the front (Chapter 5).

Appendix C

Discrepancy between BEDMAP1 and collected radar data

The airborne radar survey permits to measure the ice thickness of the glaciers around the SRM within an uncertainty of ±30 m. It shows significant discrepancies between these measurements and the thickness dataset available in 2011 (i.e. BEDMAP1 (Lythe et al., 2001). Three areas are particularly ill-defined (Figure C.1): the bed of Tussebreen, the grounding line H.E. Hansenbreen and the upstream part of West Ragnhild Glacier. These important mismatches convince us to submit our data to the new version of BEDMAP (Fretwell et al., 2013).

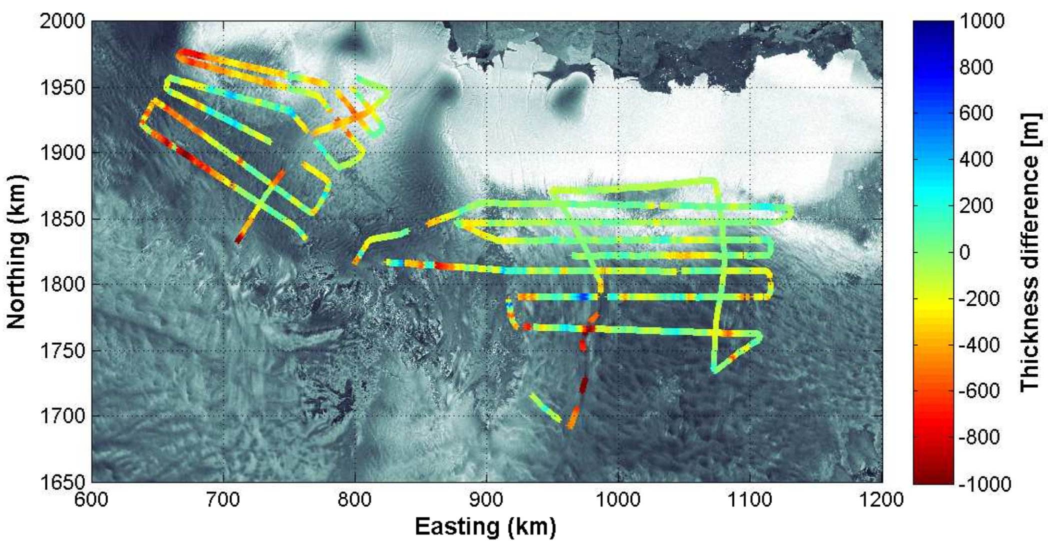

Figure C.1: Mismatch between the radar data collected in 2011 and BEDMAP1 (Lythe et al., 2001).Background is the radarsat mosaic from Jezek and RAMP Product Team (2002). Coloured lines are the difference between BEDMAP1 and our radar data. The first minus the latter.

Appendix D

Sensitivity of the roughness analysis

The roughness analysis may be difficult to grasp. Therefore we evaluate the impact of two parameters on the roughness index (RI). Here we test the sensitivity of the roughness analysis presented in Chapter 3. We performed the roughness analysis on artificial bed (Figure D.1a and Figure D.2a). The phase as well as the amplitude is tested. To understand how the phase affects the RI, the artificial bed used is described by the following sum of sinus:

$$y_n(x) = \sin(x) + \sin(x \times n)\,, \tag{D.1}$$

where y is the artificial bed geometry, x varies between 0 and 2π and n varies between 2 and 30. Figure D.1b shows the results of the test on the phase. As the phase increases, the RI rises.

To test the amplitude, we use the following description of the bed:

$$y_n(x) = t\sin(x)\,, \tag{D.2}$$

for parameter t varying between 1 and 10. The amplitude has also an impact on the RI. RI is proportional to the amplitude of the bedrock (Figure D.2).

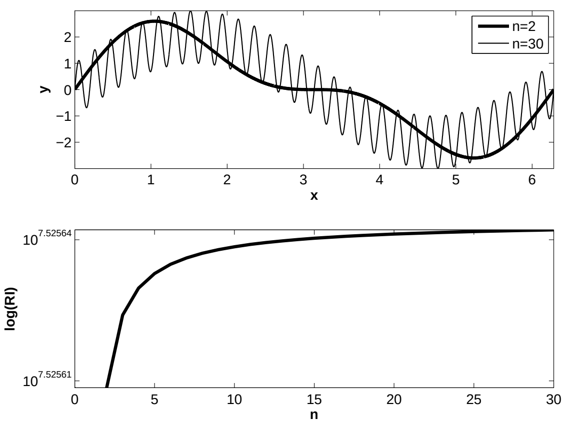

FIGURE D.1: Test of the impact of the phase on the roughness analysis. (a) Artificial bed described by Equation D.1 for the two extreme values of n (2 and 30). (b) Roughness index calculated following Equation 3.1 for n between 2 and 30.

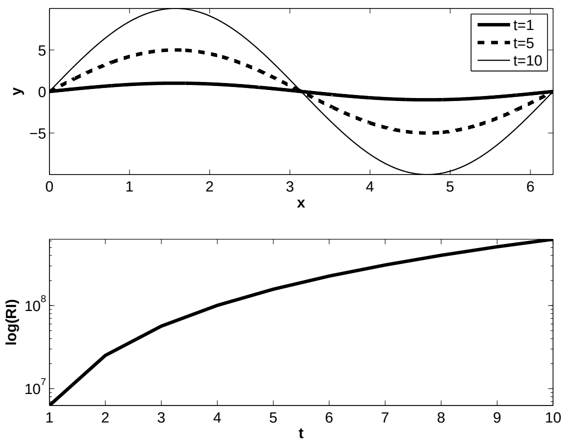

Figure D.2: Test of the impact of the amplitude on the roughness analysis. (a) Artificial bed described by Equation D.2 for three arbitrary values of t (1, 5 and 10). (b) Roughness index calculated following Equation 3.1 for t between 1 and 10.

References

Alley, R., Blankenship, D., Bentley, C., and Rooney, S. (1986). Deformation of till beneath ice stream b, west antarctica. *Nature*, 322:57–59.

Anderson, J. B., Shipp, S. S., Lowe, A. L., Wellner, J. S., and Mosola, A. B. (2002). The antarctic ice sheet during the last glacial maximum and its subsequent retreat history: a review. *Quaternary Science Reviews*, 21(1–3):49 – 70. {EPILOG}.

Anschütz, H., Müller, K., Isaksson, E., McConnell, J., Fischer, H., Miller, H., Albert, M., and Winther, J.-G. (2009). Revisiting sites of the south pole queen maud land traverses in east antarctica: accumulation data from shallow firn cores. *Journal of Geophysical Research: Atmospheres (1984–2012)*, 114(D24).

Arthern, R. J. and Gudmundsson, H. G. (2010). Initialization of ice-sheet forecasts viewed as an inverse robin problem. *Journal of Glaciology*, 56(197):527–533.

Arthern, R. J., Vaughan, D. G., Rankin, A. M., Mulvaney, R., and Thomas, E. R. (2010). In situ measurements of antarctic snow compaction compared with predictions of models. *Journal of Geophysical Research: Earth Surface (2003–2012)*, 115(F3).

Arthern, R. J., Winebrenner, D. P., and Vaughan, D. G. (2006). Antarctic snow accumulation mapped using polarization of 4.3-cm wavelength microwave emission. *Journal of Geophysical Research: Atmospheres*, 111(D6):n/a–n/a.

Bader, H. (1960). Theory of densification of dry snow on high polar glaciers, i. Technical report, Cold Regions Research and Engineering Lab Hanover.

Bader, H. (1962). Theory of densification of dry snow on high polar glaciers, ii. Technical report, Cold Regions Research and Engineering Lab Hanover.

Bamber, J. L., Gomez-Dans, J. L., and Griggs, J. A. (2009). A new 1 km digital elevation model of the antarctic derived from combined satellite radar and laser data – part 1: Data and methods. *The Cryosphere*, 3(1):101–111.

Berthier, E., Scambos, T. A., and Shuman, C. A. (2012). Mass loss of larsen b tributary glaciers (antarctic peninsula) unabated since 2002. *Geophysical Research Letters*, 39(13).

Bindschadler, R., Choi, H., Wichlacz, A., Bingham, R., Bohlander, J., Brunt, K., Corr, H., Drews, R., Fricker, H., Hall, M., Hindmarsh, R., Kohler, J., Padman, L., Rack, W., Rotschky, G., Urbini, S., Vornberger, P., and Young, N. (2011a). Getting around antarctica: new high-resolution mappings of the grounded and freely-floating boundaries of the antarctic ice sheet created for the international polar year. *The Cryosphere*, 5(3):569–588.

Bindschadler, R. A., Choi, H., and ASAID Collaborators (2011b). *High-Resolution Image-derived Grounding and Hydrostatic Lines for the Antarctic Ice Sheet*. Boulder, Colorado, USA: National Snow and Ice Data Center. Digital media.

Bingham, R. G. and Siegert, M. J. (2009). Quantifying subglacial bed roughness in antarctica: implications for ice-sheet dynamics and history. *Quaternary Science Reviews*, 28:223–236.

Blankenship, D. D., Bentley, C. R., Rooney, S., and Alley, R. B. (1986). Seismic measurements reveal a saturated porous layer beneath an active antarctic ice stream. *Nature*, 322:54–57.

Bogorodsky, V., Bentley, C., and Gudmandsen, P. (1985). *Radioglaciology.* Glaciology and Quaternary Geology. D. Reidel Publishing Company.

Boulton, G. S. and Hindmarsh, R. C. A. (1987). Sediment deformation beneath glaciers: Rheology and geological consequences. *Journal of Geophysical Research: Solid Earth*, 92(B9):9059–9082.

Callens, D. (2010). *Variabilité spatiale du bilan de masse du FranKenny Ice Rise, Dronning Maud Land, Antarctique.* Master Thesis, ULB.

Callens, D., Matsuoka, K., Steinhage, D., Smith, B., Witrant, E., and Pattyn, F. (2014). Transition of flow regime along a marine-terminating outlet glacier in east antarctica. *The Cryosphere*, 8:867–875.

Chen, J. L., Wilson, C. R., Blankenship, D., and Tapley, B. D. (2009). Accelerated Antarctic ice loss from satellite gravity measurements. *Nature Geosci.*, 2:859–862.

Church, J. A. and White, N. J. (2011). Sea-level rise from the late 19th to the early 21st century. *Surveys in Geophysics*, 32(4-5):585–602.

Coleman, T. F. and Li, Y. (1994). On the convergence of interior-reflective newton methods for nonlinear minimization subject to bounds. *Mathematical programming*, 67(1-3):189–224.

Coleman, T. F. and Li, Y. (1996). An interior trust region approach for nonlinear minimization subject to bounds. *SIAM Journal on optimization*, 6(2):418–445.

Cuffey, K. and Paterson, W. S. B. (2010). *The Physics of Glaciers. 4th ed.* Elsevier, New York.

Delcourt, C. (2012). *Dynamics, subglacial hydrology and polythermal regime of McCall Glacier (Alaska, USA).* PhD Thesis, ULB.

Depoorter, M. A., Bamber, J. L., Griggs, J. A., Lenaerts, J. T. M., Ligtenberg, S. R. M., van den Broeke, M. R., and Moholdt, G. (2013). Calving fluxes and basal melt rates of antarctic ice shelves. *Nature*, 502(7469):89–92.

Derwael, J. (1985). Levés altimétriques - BRB - côte princesse ragnild, expéditions antarctiques belgo-néerlandaises (5 maps), exantar. (1965).

Drews, R., Matusoka, K., Martìn, C., Callens, D., Bergeot, N., and Pattyn, F. (2014). Sustained thinning over millennia of an ice rise in dronning maud land, antarctica. *Submitted to J. Geophys. Res.*

Dutrieux, P., Vaughan, D. G., Corr, H. F. J., Jenkins, A., Holland, P. R., Joughin, I., and Fleming, A. H. (2013). Pine island glacier ice shelf melt distributed at kilometre scales. *The Cryosphere*, 7(5):1543–1555.

Eisen, O., Frezzotti, M., Genthon, C., Isaksson, E., Magand, O., van den Broeke, M. R., Dixon, D. A., Ekaykin, A., Holmlund, P., Kameda, T., Karlf, L., Kaspari, S., Lipenkov, V. Y., Oerter, H., Takahashi, S., and Vaughan, D. G. (2008). Ground-based measurements of spatial and temporal variability of snow accumulation in east antarctica. *Reviews of Geophysics*, 46(2):n/a–n/a.

Favier, L., Gagliardini, O., Durand, G., and Zwinger, T. (2012). A three-dimensional full stokes model of the grounding line dynamics: effect of a pinning point beneath the ice shelf. *The Cryosphere*, 6(1):101–112.

Fjøsne, K. (2014). *Etude paléoclimatique et glacio-dynamique d'un sondage de 120 mètres (Dronning Maud Land, Antarctique).* Master Thesis, ULB.

Fretwell, P., Pritchard, H. D., Vaughan, D. G., Bamber, J. L., Barrand, N. E., Bell, R., Bianchi, C., Bingham, R. G., Blankenship, D. D., Casassa, G., Catania, G., Callens, D., Conway, H., Cook, A. J., Corr, H. F. J., Damaske, D., Damm, V., Ferraccioli, F., Forsberg, R., Fujita, S., Gim, Y., Gogineni, P., Griggs, J. A., Hindmarsh, R. C. A., Holmlund, P., Holt, J. W., Jacobel, R. W., Jenkins, A., Jokat, W., Jordan, T., King, E. C., Kohler, J., Krabill, W., Riger-Kusk, M., Langley, K. A., Leitchenkov, G., Leuschen, C., Luyendyk, B. P., Matsuoka, K., Mouginot, J., Nitsche, F. O., Nogi, Y., Nost, O. A., Popov, S. V., Rignot, E., Rippin, D. M., Rivera, A., Roberts, J., Ross, N., Siegert, M. J., Smith, A. M., Steinhage, D., Studinger, M., Sun, B., Tinto, B. K., Welch, B. C., Wilson, D., Young, D. A., Xiangbin, C., and Zirizzotti, A. (2013). Bedmap2: improved ice bed, surface and thickness datasets for antarctica. *The Cryosphere*, 7:375–393.

Frezzotti, M., Scarchilli, C., Becagli, S., Proposito, M., and Urbini, S. (2013). A synthesis of the antarctic surface mass balance during the last 800 yr. *The Cryosphere*, 7(1):303–319.

Fujita, S., Holmlund, P., Andersson, I., Brown, I., Enomoto, H., Fujii, Y., Fujita, K., Fukui, K., Furukawa, T., Hansson, M., Hara, K., Hoshina, Y., Igarashi, M., Iizuka, Y., Imura, S., Ingvander, S., Karlin, T., Motoyama, H., Nakazawa, F., Oerter, H., Sjöberg, L. E., Sugiyama, S., Surdyk, S., Ström, J., Uemura, R., and Wilhelms, F. (2011). Spatial and temporal variability of snow accumulation rate on the east antarctic ice divide between dome fuji and epica dml. *The Cryosphere*, 5(4):1057–1081.

Fujita, S., Maeno, H., Uratsuka, S., Furukawa, T., Mae, S., Fujii, Y., and Watanabe, O. (1999). Nature of radio echo layering in the Antarctic ice sheet detected by a two-frequency experiment. *J. Geophys. Res.*, 104(B6):13,013–13,024.

Gardner, A. S., Moholdt, G., Cogley, J. G., Wouters, B., Arendt, A. A., Wahr, J., Berthier, E., Hock, R., Pfeffer, W. T., Kaser, G., Ligtenberg, S. R. M., Bolch, T., Sharp, M. J., Hagen, J. O., van den Broeke, M. R., and Paul, F. (2013). A reconciled estimate of glacier contributions to sea level rise: 2003 to 2009. *Science*, 340(6134):852–857.

Gossart, A. (2014). *Basal mass Balance of the Roi Baudouin Ice Shelf, using GPS and radar.* Master Thesis, ULB.

Gudmundsson, G. H., Krug, J., Durand, G., Favier, L., and Gagliardini, O. (2012). The stability of grounding lines on retrograde slopes. *The Cryosphere*, 6(6):1497–1505.

Gunter, B., Urban, T., Riva, R., Helsen, M., Harpold, R., Poole, S., Nagel, P., Schutz, B., and Tapley, B. (2009). A comparison of coincident grace and icesat data over antarctica. *Journal of Geodesy*, 83(11):1051–1060.

Haefeli, R. (1963). A numerical and experimental method for determining ice motion in the central parts of ice sheets. *IAHS Publ.*, 61:253–260.

Hanna, E., Navarro, F. J., Pattyn, F., Domingues, C. M., Fettweis, X., Ivins, E. R., Nicholls, R. J., Ritz, C., Smith, B., Tulaczyk, S., Whitehouse, P. L., and Zwally, H. J. (2013). Ice-sheet mass balance and climate change. *Nature*, 498(7452):51–59.

Hattermann, T., Nøst, O. A., Lilly, J. M., and Smedsrud, L. H. (2012). Two years of oceanic observations below the fimbul ice shelf, antarctica. *Geophysical Research Letters*, 39(12):n/a–n/a.

Hindmarsh, R. C. A. (1999). On the numerical computation of temperature in an ice sheet. *J. Glaciol.*, 45(151):568–574.

Holland, D. M. and Jenkins, A. (1999). Modeling thermodynamic ice-ocean interactions at the base of an ice shelf. *J. Phys. Oceanogr.*, 29(8):1787–1800.

Holland, P. R., Jenkins, A., and Holland, D. M. (2008). The response of ice shelf basal melting to variations in ocean temperature. *Journal of Climate*, 21(11).

Horgan, H. J., Alley, R. B., Christianson, K., Jacobel, R. W., Anandakrishnan, S., Muto, A., Beem, L. H., and Siegfried, M. R. (2013). Estuaries beneath ice sheets. *Geology*, 41(11):1159–1162.

Høydal, Ø. A. (1996). A force-balance study of ice flow and basal conditions of Jutulstraumen, Antarctica. *J. Glaciol.*, 42(142):413–425.

Hubbard, B., Tison, J. L., Pattyn, F., Dierckx, M., Boereboom, T., and Samyn, D. (2012). Optical televiewer-based identification and characterization of material facies associated with an Antarctic ice-shelf rift. *Ann. Glaciol.*, 53(60):137–146.

Hubbard, B., Tison, J.-L., Philippe, M., Heene, B., Pattyn, F., Malone, T., and Freitag, J. (2013). Ice shelf density reconstructed from optical televiewer borehole logging. *Geophysical Research Letters*, 40(22):5882–5887.

Isaksson, E., van den Broeke, M. R., Winther, J.-G., Karlöf, L., Pinglot, J. F., and Gundestrup, N. (1999). Accumulation and proxy-temperature variability in dronning maud land, antarctica, determined from shallow firn cores. *Annals of Glaciology*, 29(1):17–22.

Jacobs, S. S. (1991). On the nature and significance of the antarctic slope front. *Marine Chemistry*, 35(1–4):9 – 24.

Jacobs, S. S., Jenkins, A., Giulivi, C. F., and Dutrieux, P. (2011). Stronger ocean circulation and increased melting under pine island glacier ice shelf. *Nature Geoscience*, 4(8):519–523.

Jenkins, A., Dutrieux, P., Jacobs, S., McPhail, S., Perrett, J., Webb, A., and White, D. (2010). Observations beneath Pine Island Glacier in West Antarctica and implications for its retreat. *Nature Geosci.*, 3(7):468–472.

Jezek, K. and RAMP Product Team (2002). *RAMP AMM-1 SAR Image Mosaic of Antarctica*. http://nsidc.org/data/nsidc-0103.html, Alaska SAR Facil., Natl. Snow and Ice Data Cent., Boulder, Colorado.

Joughin, I. (2002). Ice-sheet velocity mapping: A combined interferometric and speckle-tracking approach. *Ann. Glaciol.*, 34:195–201.

Joughin, I., Rignot, E., Rosanova, C. E., Lucchitta, B. K., and Bohlander, J. (2003). Timing of recent accelerations of Pine Island Glacier, Antarctica. *Geophys. Res. Lett.*, 30(13):10.1029/2003GL017609.

Kamb, B. and Echelmeyer, K. A. (1986). Stress-gradient coupling in glacier flow: 1. longitudinal averaging of the influence of ice thickness and surface slope. *J. Glaciol.*, 32(111):267–298.

Khazendar, A. and Jenkins, A. (2003). A model of marine ice formation within Antarctic ice shelf rifts. *J. Geophys. Res.*, 108(C7, 3235).

Khazendar, A., Schodlok, M., Fenty, I., Ligtenberg, S., Rignot, E., and van den Broeke, M. (2013). Observed thinning of totten glacier is linked to coastal polynya variability. *Nature communications*, 4:2857.

King, J., Anderson, P., Vaughan, D., Mann, G., Mobbs, S., and Vosper, S. (2004). Wind-borne redistribution of snow across an antarctic ice rise. *Journal of Geophysical Research: Atmospheres (1984–2012)*, 109(D11).

King, M. A., Bingham, R. J., Moore, P., Whitehouse, P. L., Bentley, M. J., and Milne, G. A. (2012). Lower satellite-gravimetry estimates of antarctic sea-level contribution. *Nature*, 491(7425):586–589.

Kulessa, B., Jansen, D., Luckman, A. J., King, E. C., and Sammonds, P. R. (2014). Marine ice regulates the future stability of a large antarctic ice shelf. *Nature communications*, 5.

Le Brocq, A. M., Ross, N., Griggs, J. A., Bingham, R. G., Corr, H. F. J., Ferraccioli, F., Jenkins, A., Jordan, T. A., Payne, A. J., Rippin, D. M., and Siegert, M. J. (2013). Evidence from ice shelves for channelized meltwater flow beneath the antarctic ice sheet. *Nature Geosci*, 6(11):945–948.

Lenaerts, J. T. M., Brown, J., van den Broeke, M. R., Matsuoka, K., Drews, R., Callens, D., Philippe, M., Gorodetskaya, I. V., van Meijgaard, E., Reijmer, C. H., Pattyn, F., and Van Lipzig, N. P. M. (2014). High variability of climate and surface mass balance induced by antarctic ice rises. *J. Glaciol.*, 60(224):1101–1110.

Lenaerts, J. T. M., van den Broeke, M. R., van de Berg, W. J., van Meijgaard, E., and Kuipers Munneke, P. (2012). A new, high-resolution surface mass balance map of antarctica (1979–2010) based on regional atmospheric climate modeling. *Geophysical Research Letters*, 39(4):n/a–n/a.

Leonard, K., Pattyn, F., Callens, D., Matusoka, K., Derwael, J., and Tison, J. (in Prep.). Warm deep water under an east antarctic ice shelf: implications for grounding line melt.

Little, C. M., Gnanadesikan, A., and Oppenheimer, M. (2009). How ice shelf morphology controls basal melting. *Journal of Geophysical Research: Oceans*, 114(C12):n/a–n/a.

Looyenga, H. (1965). Dielectric constants of heterogeneous mixtures. *Physica*, 31(3):401–406.

Lythe, M. B., Vaughan, D. G., and BEDMAP consortium (2001). BEDMAP: A new ice thickness and subglacial topographic model of Antarctica. *J. Geophys. Res.*, 106(B6):11335–11351.

MacAyeal, D. R. (1992). Irregular oscillations of the West Antarctic ice sheet. *Nature*, 359:29–32.

MacAyeal, D. R. (1993). A tutorial on the use of control methods in ice-sheet modeling. *J. Glaciol.*, 39(131):91–98.

MacGregor, J. A., Winebrenner, D. P., Conway, H., Matsuoka, K., Mayewski, P. A., and Clow, G. D. (2007). Modeling englacial radar attenuation at Siple Dome, West Antarctica, using ice chemistry and temperature data. *J. Geophys. Res.*, 112(F03008).

Mackintosh, A. N., Verleyen, E., O'Brien, P. E., White, D. A., Jones, R. S., McKay, R., Dunbar, R., Gore, D. B., Fink, D., Post, A. L., Miura, H., Leventer, A., Goodwin, I., Hodgson, D. A., Lilly, K., Crosta, X., Golledge, N. R., Wagner, B., Berg, S., van Ommen, T., Zwartz, D., Roberts, S. J., Vyverman, W., and Masse, G. (2014). Retreat history of the east antarctic ice sheet since the last glacial maximum. *Quaternary Science Reviews*, 100(0):10 – 30. Reconstruction of Antarctic Ice Sheet Deglaciation (RAISED).

Martìn, C., Gudmundsson, G. H., Pritchard, H. D., and Gagliardini, O. (2009). On the effects of anisotropic rheology on ice flow, internal structure, and the age-depth relationship at ice divides. *Journal of Geophysical Research: Earth Surface*, 114(F4):n/a–n/a.

Martin, P. and Sanderson, T. (1980). Morphology and dynamics of ice rises. *Journal of Glaciology*, 25:33–45.

Matsuoka, K. (2011). Pitfalls in radar diagnosis of ice-sheet bed conditions: Lessons from englacial attenuation models. *Geophysical Research Letters*, 38(5).

Matsuoka, K., MacGregor, J. A., and Pattyn, F. (2012a). Predicting radar attenuation within the antarctic ice sheet. *Earth and Planetary Science Letters*, 359 - 360:173 – 183.

Matsuoka, K., Pattyn, F., Callens, D., and Conway, H. (2012b). Radar characteristics of the basal interface across the grounding zone of an ice-rise promontory, East Antarctica. *Ann. Glaciol.*, 53(60):29–34.

Meijers, A., Klocker, A., Bindoff, N., Williams, G., and Marsland, S. (2010). The circulation and water masses of the antarctic shelf and continental slope between 30 and 80°e. *Deep Sea Research Part II: Topical Studies in Oceanography*, 57(9):723–737.

Mengel, M. and Levermann, A. (2014). Ice plug prevents irreversible discharge from east antarctica. *Nature Climate Change*, 4:451–455.

Mercenier, R. (2014). *Using inverse control methods to evaluate the effect of unpinning on the Roi Baudouin Ice Shelf, Dronning Maud Land, Antarctica.* Master Thesis, ULB.

Miles, B. W. J., Stokes, C. R., Vieli, A., and Cox, N. J. (2013). Rapid, climate-driven changes in outlet glaciers on the pacific coast of east antarctica. *Nature*, 500(7464):563–566.

Morse, D., Waddington, E., and Steig, E. (1998). Ice age storm trajectories inferred from radar stratigraphy at taylor dome, antarctica. *Geophysical Research Letters*, 25(17):3383–3386.

Nerem, R., Chambers, D., Choe, C., and Mitchum, G. (2010). Estimating mean sea level change from the topex and jason altimeter missions. *Marine Geodesy*, 33(S1):435–446.

Nereson, N., Raymond, C., Jacobel, R., and Waddington, E. (2000). The accumulation pattern across siple dome, west antarctica, inferred from radar-detected internal layers. *Journal of Glaciology*, 46(152):75–87.

Nixdorf, U., Steinhage, D., Meyer, U., Hempel, L., Jenett, M., Wachs, P., and Miller, H. (1999). The newly developed airborne radio-echo sounding system of the AWI as a glaciological tool. *Ann. Glaciol.*, 29:231–238.

Oppenheimer, M. (1998). Global warming and the stability of the west antarctic ice sheet. *Nature*, 393(6683):325–332.

Orsi, A. H., Whitworth, T., and Jr., W. D. N. (1995). On the meridional extent and fronts of the antarctic circumpolar current. *Deep Sea Research Part I: Oceanographic Research Papers*, 42(5):641 – 673.

Pattyn, F. (1996). Numerical modelling of a fast-flowing outlet glacier: Experiments with different basal conditions. *Ann. Glaciol.*, 23:237–246.

Pattyn, F. (2000). Ice-sheet modelling at different spatial resolutions: Focus on the grounding line. *Ann. Glaciol.*, 31:211–216.

Pattyn, F. (2002). Transient glacier response with a higher-order numerical ice-flow model. *J. Glaciol.*, 48(162):467–477.

Pattyn, F. (2003). A new 3D higher-order thermomechanical ice-sheet model: Basic sensitivity, ice-stream development and ice flow across subglacial lakes. *J. Geophys. Res.*, 108(B8, 2382).

Pattyn, F. (2010). Antarctic subglacial conditions inferred from a hybrid ice sheet/ice stream model. *Earth Planet. Sci. Lett.*, 295:451–461.

Pattyn, F., De Brabander, S., and Huyghe, A. (2005). Basal and thermal control mechanisms of the Ragnhild glaciers, East Antarctica. *Ann. Glaciol.*, 40:225–231.

Pattyn, F. and Derauw, D. (2002). Ice-dynamic conditions of Shirase Glacier, Antarctica, inferred from ERS–SAR interferometry. *J. Glaciol.*, 48(163):559–565.

Pattyn, F., Matsuoka, K., Conway, H., Callens, D., Depoorter, M., Docquier, D., Hubbard, B., Samyn, D., and Tison, J. L. (2012). Radar and ice-core evidence for active ice-ocean interaction under the Roi Baudouin ice shelf, East Antarctica. *J. Geophys. Res.*, 117(F04008).

Pattyn, F., Perichon, L., Aschwanden, A., Breuer, B., De Smedt, B., Gagliardini, O., Gudmundsson, G. H., Hindmarsh, R. C. A., Hubbard, A., Johnson, J. V., Kleiner, T., Konovalov, Y., Martin, C., Payne, A. J., Pollard, D., Price, S., Rückamp, M., Saito, F., Soucek, O., Sugiyama, S., and Zwinger, T. (2008). Benchmark experiments for higher-order and full-Stokes ice sheet models (ISMIP–HOM). *The Cryosphere*, 2:95–108.

Payne, A. J., Holland, P. R., Shepherd, A. P., Rutt, I. C., Jenkins, A., and Joughin, I. (2007). Numerical modeling of ocean-ice interactions under Pine Island Bay's ice shelf. *J. Geophys. Res.*, 112(C10):C10019.

Pritchard, H. D., Ligtenberg, S. R. M., Fricker, H. A., Vaughan, D. G., van den Broeke, M. R., and Padman, L. (2012). Antarctic ice-sheet loss driven by basal melting of ice shelves. *Nature*, 484:502 – 505.

Rabus, B. T. and Echelmeyer, K. A. (1997). The flow of a polythermal glacier: McCall Glacier, Alaska, U.S.A. *J. Glaciol.*, 43(145):522–536.

Rapp, R. H. (1997). Use of potential coefficient models for geoid undulation determinations using a spherical harmonic representation of the height anomaly/geoid undulation difference. *Journal of Geodesy*, 71:282–289.

Raymond, C. F. (1983). Deformation in the vicinity of ice divides. *J. Glaciol.*, 29:357–373.

Reeh, N. (1989). The age-depth profile in the upper part of a steady-state ice sheet. *Journal of Glaciology*, 35(121):406–417.

Rhein, M., Rintoul, S., Aoki, S., Campos, E., Chambers, D., Feely, R., Gulev, S., Johnson, G., Josey, S., Kostianoy, A., Mauritzen, C., Roemmich, D., Talley, L., and Wang, F. (2013). Observations: Ocean. In Stocker, T., Qin, D., Plattner, G.-K., Tignor, M., Allen, S., Boschung, J., Nauels, A., Xia, Y., Bex, V., and Midgley, P., editors, *Climate Change 2013: The Physical Science Basis. Contribution of Working Group I to the Fifth Assessment Report of the Intergovernmental Panel on Climate Change*, Cambridge, United Kingdom and New York, NY, USA. Cambridge University Press.

Rignot, E., Jacobs, S., , Mouginot, J., and Scheuchl, B. (2013). Ice shelf melting around antarctica. *Science*, 314(6143):266–270.

Rignot, E., Mouginot, J., and Scheuchl, B. (2011a). Ice flow of the antarctic ice sheet. *Science*, 333(6048):1427–1430.

Rignot, E., Mouginot, J., and Scheuchl, B. (2011b). Measures antarctic grounding line from differential satellite radar interferometry. boulder, colorado usa: Nasa eosdis distributed active archive center at nsidc. Boulder, Colorado, USA. Digital media.

Rignot, E., Velicogna, I., van den Broeke, M. R., Monaghan, A., and Lenaerts, J. (2011c). Acceleration of the contribution of the Greenland and Antarctic ice sheets to sea level rise. *Geophys. Res. Lett.*, 38(L05503):doi:10.1029/2011GL046583.

Rignot, E. J., Bamber, J. L., van den Broeke, M. R., Davis, C., Li, Y., van de Berg, W. J., and van Meijgaard, E. (2008). Recent Antarctic ice mass loss from radar interferometry and regional climate modelling. *Nature Geosci.*, 1:106–110.

Rippin, D. M., Vaughan, D. G., and Corr, H. F. J. (2011). The basal roughness of pine island glacier, west antarctica. *J. Glaciol.*, 57(201):67–76.

Rybak, O. and Huybrechts, P. (2003). A comparison of eulerian and lagrangian methods for dating in numerical ice-sheet models. *Annals of Glaciology*, 37(1):150–158.

Scambos, T. A., Bohlander, J. A., Shuman, C. A., and Skvarca, P. (2004). Glacier acceleration and thinning after ice shelf collapse in the Larsen B embayment. *Geophys. Res. Lett.*, 31(18):L18402.

SCAR (2012). Scientific committee on antarctic research antarctic digital datablase. Digital media.

Schoof, C. (2007). Ice sheet grounding line dynamics: Steady states, stability and hysteresis. *J. Geophys. Res.*, 112(F03S28).

Schoof, C. (2010). Glaciology: Beneath a floating ice shelf. *Nature Geosci*, 3(7):450–451.

Schröder, M. and Fahrbach, E. (1999). On the structure and the transport of the eastern weddell gyre. *Deep Sea Research Part II: Topical Studies in Oceanography*, 46(1–2):501 – 527.

Shepherd, A., Ivins, E. R., A, G., Barletta, V. R., Bentley, M. J., Bettadpur, S., Briggs, K. H., Bromwich, D. H., Forsberg, R., Galin, N., Horwath, M., Jacobs, S., Joughin, I., King, M. A., Lenaerts, J. T. M., Li, J., Ligtenberg, S. R. M., Luckman, A., Luthcke, S. B., McMillan, M., Meister, R., Milne, G., Mouginot, J., Muir, A., Nicolas, J. P., Paden, J., Payne, A. J., Pritchard, H., Rignot, E., Rott, H., Sandberg Srensen, L., Scambos, T. A., Scheuchl, B., Schrama, E. J. O., Smith, B., Sundal, A. V., van Angelen, J. H., van de Berg, W. J., van den Broeke, M. R., Vaughan, D. G., Velicogna, I., Wahr, J., Whitehouse, P. L., Wingham, D. J., Yi, D., Young, D., and Zwally, H. J. (2012). A reconciled estimate of ice-sheet mass balance. *Science*, 338:1183–1189.

Smedsrud, L., Jenkins, A., Holland, D. M., and Nøst, O. A. (2006). Modeling ocean processes below the Fimbul Ice Shelf. *J. Geophys. Res.*, 111(C01007).

Stanton, T. P., Shaw, W. J., Truffer, M., Corr, H. F. J., Peters, L. E., Riverman, K. L., Bindschadler, R., Holland, D. M., and Anandakrishnan, S. (2013). Channelized ice melting in the ocean boundary layer beneath pine island glacier, antarctica. *Science*, 341(6151):1236–1239.

Steinhage, D., Nixdorf, U., Meyer, U., and Miller, H. (1999). New maps of the ice thickness and subglacial topography in Dronning Maud Land, Antarctica, determined by means of airborne radio-echo sounding. *Ann. Glaciol.*, 29:267–272.

Steinhage, D., Nixdorf, U., Meyer, U., and Miller, H. (2001). Subglacial topography and internal structure of central and western dronning maud land, antarctica, determined from airborne radio echo sounding. *Journal of Applied Geophysics*, 47(3-4):183 – 189.

Taylor, J., Siegert, M., Payne, A., and Hubbard, B. (2004). Regional-scale bed roughness beneath ice masses: Measurement and analysis. *Computers and Geosciences*, 30:899–908.

Thonnard, N. (2013). *Outlet dynamics in Dronning Maud Land, Antarctica.* Master Thesis, ULB.

Thyssen, F. (1988). Special aspects of the central part of filchner-ronne ice shelf, antarctica. *Ann. Glaciol*, 11:173–179.

Timmermann, R., Le Brocq, A., Deen, T., Domack, E., Dutrieux, P., Galton-Fenzi, B., Hellmer, H., Humbert, A., Jansen, D., Jenkins, A., Lambrecht, A., Makinson, K., Niederjasper, F., Nitsche, F., Nøst, O. A., Smedsrud, L. H., and Smith, W. H. F. (2010). A consistent data set of antarctic ice sheet topography, cavity geometry, and global bathymetry. *Earth System Science Data*, 2(2):261–273.

Tison, J. L. and Khazendar, A. (2001). The isotope/salinity relationship in marine ice: New perspectives. *J. Geophys. Res.*, 106(C12):31387–31401.

Van Autenboer, T. and Decleir, H. (1978). Glacier discharge in the sør-rondane, a contribution to the mass balance of dronning maud land, antarctica. *Zeitschrift fr Gletscherkunde und Glazialgeologie*, 14(1):1–16.

van de Berg, W. J., van den Broeke, M. R., Reijmer, C. H., and van Meijgaard, E. (2006). Reassessment of the Antarctic surface mass balance using calibrated output of a regional atmospheric climate model. *J. Geophys. Res*, 111(D11104).

van den Broeke, M., Bamber, J., Ettema, J., Rignot, E., Schrama, E., van de Berg, W. J., van Meijgaard, E., Velicogna, I., and Wouters, B. (2009). Partitioning recent greenland mass loss. *Science*, 326(5955):984–986.

Van der Veen, C. J. (2013). *Fundamentals of glacier dynamics*. CRC Press.

Van Wessem, J., Reijmer, C. H., Morlighem, M., Mouginot, J., Rignot, E., Medley, B., Joughin, I., Wouters, B., Depoorter, M., Bamber, J., Lenaerts, J., de Berg, W. V., den Broeke, M. V., and Meijgaard, E. V. (2014). Improved representation of east antarctic surface mass balance in a regional atmospheric climate model. *Journal of Glaciology*, 60(222):761.

Vaughan, D., Comiso, J., Allison, I., Carrasco, J., Kaser, G., Kwok, R., Mote, P., Murray, T., Paul, F., Ren, J., Rignot, E., Solomina, O., Steffen, K., and Zhang, T. (2013). Observations: Cryosphere. In Stocker, T., Qin, D., Plattner, G.-K., Tignor, M., Allen, S., Boschung, J., Nauels, A., Xia, Y., Bex, V., and Midgley, P., editors, *Climate Change 2013: The Physical Science Basis. Contribution of Working Group I to the Fifth Assessment Report of the Intergovernmental Panel on Climate Change*, Cambridge, United Kingdom and New York, NY, USA. Cambridge University Press.

Waddington, E. D., Neumann, T. A., Koutnik, M. R., Marshall, H. P., and Morse, D. L. (2007). Inference of accumulation-rate patterns from deep layers in glaciers and ice sheets. *J. Glaciol.*, 53(183):694–712.

Weertman, J. (1974). Stability of the junction of an ice sheet and an ice shelf. *J. Glaciol.*, 13:3–11.

Whitworth, T., Orsi, A. H., Kim, S.-J., Nowlin, W. D., and Locarnini, R. A. (2013). Water masses and mixing near the antarctic slope front. In Jacobs, S. and Weiss, R., editors, *Ocean, Ice, and Atmosphere: Interactions at the Antarctic Continental Margin*, pages 1–27. American Geophysical Union.

Wong, P., Losada, I., Gattuso, J. P., Hinkel, J., Khattabi, A., McInnes, K., Saito, Y., and Sallenger, A. (2014). Coastal systems and low-lying areas. In Field, C., Barros, V., Dokken, D., Mach, K., Mastrandrea, M., Bilir, T., Chatterjee, M., Ebi, K., Estrada, Y., Genova, R., Girma, B., Kissel, E., Levy, A., MacCracken, S., Mastrandrea, P., and White, L., editors, *Climate Change 2014:Impacts, Adaptation, and Vulnerability. Contribution of Working Group II to the Fifth Assessment Report of the Intergovernmental Panel on Climate Change*, Cambridge, United Kingdom and New York, NY, USA. Cambridge University Press.

Zwally, H. and Giovinetto, M. (2011). Overview and assessment of antarctic ice-sheet mass balance estimates: 1992 – 2009. *Surveys in Geophysics*, 32(4-5):351–376.